Topical Review

Material strategies to enhance the performance of piezoelectric energy harvesters based on lead-free materials

Ausrine Bartasyte[1,2], Giacomo Clementi[1,3], Quentin Micard[1,4], Ishamol Labbaveettil[1], Arthur Sousa Lopes Moreira[1,5], Sondes Boujnah[1], Merieme Ouhabaz[1], Anjenya Verma[6], Arun Ichangi[6,7], Graziella Malandrino[4], Sanjay Mathur[6], Bernard Dulmet[1] and Samuel Margueron[1]

[1] FEMTO-ST Institute, University of Bourgogne Franche-Comté, CNRS UMR6174 Besançon, France

[2] Institut Universitaire de France (IUF), Paris, France

[3] University of Perugia, Perugia, Italy

[4] Dipartimento di Scienze Chimiche, Università di Catania and INSTM UdR Catania, Viale A. Doria 6, Catania 95125, Italy

[5] WIKA Group, Klingenberg am Main, Germany

[6] Institute of Inorganic Chemistry, University of Cologne, Cologne, Germany

[7] Laboratory for High Performance Ceramics, Empa—Swiss Federal Laboratories for Materials Science and Technology, Überlandstrasse 129, 8600 Dübendorf, Switzerland

E-mail: ausrine.bartasyte@femto-st.fr

Abstract

Over the past four decades, energy microsources based on piezoelectric energy harvesting have been intensively studied for applications in autonomous sensor systems. The research is triggered by the request for replacing standard lead-based piezoelectric ceramics with environmentally friendly lead-free materials and potential deployment of energy-harvesting microsystems in internet of things, internet of health, 'place and leave' sensors in infrastructures and agriculture monitoring. Moreover, futher system miniaturization and co-integration of functions are required in line with a desired possibility to increase the harvested power density per material volume. Thus, further research efforts are necessary to develop more sustainable materials/systems with high-performance. This paper gives a comprehensive overview on the processing and functional testing the lead-free bulk materials and thin films and discusses their potential in the applications in the stress- and strain-driven piezoelectric energy harvesting. This includes the methodology of estimation of the substrate clamping and orientation/texture effects in the thin films, and identification of orientations offering high figure of merit. The ability to control film orientation of different lead-free materials is reviewed and the expected piezoelectric performances are compared with the ones reported in literature.

Keywords: lead-free materials, piezoelectricity, thin films, symmetry, orientation, figure of merit

1. Introduction

Structural health monitoring, wearable and portable healthcare devices, widely distributed wireless sensors in smart agriculture, home and industry, smart automation, and transport industry are all examples of application fields that would largely benefit from self-sufficient energy technologies from micro-energy harvesting solutions and/or from the drastic reduction of energy consumption [1–5]. In the past decades, information processing power and connectivity have been the main limiting factors of information technology. Advances in metal-oxide-semiconductor field-effect transistor (MOSFET) and communication technologies have determined new applications and services. Recently, Internet-of-Things (IoT), Internet of Health (IoH) and monitoring by distributed sensor networks have emerged. The key limiting factor in IoT devices and their applications is energy autonomy. Energy harvesting (EH) through, the collection of local environmental energy has been developing rapidly since 2000 and many different energy autonomous sensor systems have been already demonstrated [2–6]. With the advent of ultralow power microelectronics that led to a drastic reduction in the consumption of electrical components (going from 100's of mW 40 years ago to a few μW nowadays in idle mode), it is now possible to perform an electronic function with a very low amount of energy. This enabled the functioning of structural health control [7–10] temperature measurements [11] or wireless switches [12–14] with very little amount of energy. More than 30 trillion sensors are expected to be deployed worldwide in the near future [15].

Low-power MEMS sensors, based on Si technology, became the devices of choice offering cost effective solutions and high yield in automotive and aerospace industry. This includes accelerometers, pressure sensors, microbolometers, gyroscopes, communication filters, etc. Piezoelectric vibration energy harvesters (PiViEHs) for self-powered wireless MEMS networks are particularly attractive due to the possibility of direct integration with electronic circuits & sensor nodes [6, 16, 17]. Therefore, EH from vibrations, also called inertial harvesting, has become a focus of interest during the past years. Harvesting vibrations with piezoelectric devices were thoroughly studied with bulk $PbZr_{1-x}Ti_xO_3$ (PZT) materials, and piezoelectric bulk composites. More recently, since about ten years, the miniaturization of harvesters using MEMS technology with thin piezoelectric films or nanocomposites came into the focus of interest in order to power small systems such as wireless nodes. Initial studies were indeed carried out at high-frequency vibrations in order to maximize the harvested energy [18]. However, they required forced excitation that is not readily available in the environment. Recent research permitted reducing the operating frequencies from several kHz to a range between 10 Hz and 300 Hz, where vibrations are widely available in the environment (motions of humans/animals, sea waves, automotive engines, etc), while maintaining an interesting output power. The volume/size of the cell is highly limited in the case of integrated sensors (typical volume of a sensor <1 cm^3) [19] including a sensing system, an energy harvester with a MEMS transducer, energy storage and electronics. If the sensor is wireless, it will include the communication module, as well. The harvested power is reduced by more than 10 times when the volume is reduced by 10 times [20]. Miniaturization normally also leads to an increase in frequency.

The state-of-the-art piezoelectric EH is enough to power various wireless sensor networks. However, the functioning of vibrational EH in most cases is limited to very specific environmental conditions. In addition, the harvesters typically include materials with toxic or rare elements in the transducers and battery (Pb, Te, Bi, etc). Obtaining high power output from piezoelectric harvesters in many applications requires a high figure of merit (FoM). Hence this resulted in the preference and common use of bulk PZT in piezoelectric harvesters. However, in future, PZT has to be replaced by lead-free materials, even for thin films, to reduce any negative ecological impact of lead-based transducers.

In order to enable the wide deployment of micro-energy sources based on EH in IoTs, Distributed Sensor Management, and the 'place and leave' sensors, further research effort has to be done in development of more sustainable fabrication processes and eco-friendly materials and systems with long life/durability, improved recyclability of materials, ameliorated capacity of miniaturization devices through heterogeneous cointegration of different functions, as well as further decrease in power demand through the increased transduction efficiency and generated power density (PD).

At present, many different lead-free ferroelectric (e.g. $BaTiO_3$ (BTO), $K_{1-x}Na_xNbO_3$ (KNN), etc) and non-ferroelectric (AlN, ZnO) piezoelectric materials in the form of films, nanostructures and ceramic/crystals bonded on wafers are explored for the fabrication of PiViEHs [5]. The integration of lead-free piezoelectric films as transducers in the EH applications is essential for the MEMS scale devices and due to the required flexibility & robustness of the vibrational energy scavengers. Unfortunately, the communities working on the material synthesis and optimization, and on the integrated systems and electronics have made limited concerted efforts so that functional validation of new materials in device structures remains elusive. Despite the environmental restrictions, EH systems are still frequently developed by using on-shelf lead-based materials.

This paper gives a comprehensive overview of the symmetry and properties of lead-free materials and their potential in the applications in vibrational energy harvesting. This includes the comparison of the equivalent bulk materials, the estimation of the substrate clamping effect in the thin film, and identification of their highly coupled orientations. The ability to control film orientation of different lead-free materials will be summarized and their expected piezoelectric performance will be compared with the ones reported in the literature.

2. Theoretical considerations

2.1. Piezoelectricity

The vibrational EH is based on the direct piezoelectric effect relating a mechanical stress, T_J, to a dielectric displacement vector, D_i,:

$$D_i = d_{iJ}T_J\,(i = 1{-}3 \text{ and } J = 1{-}6)\,. \tag{1}$$

In this paper, the capital letters, (*I, J, L*) are used for the contracted coefficients in matrix notation, which can vary from 1 to 6. In a general case, d_{iJ} is a strain piezoelectric tensor (3^{rd} rank tensor with 18 independent coefficients:

$$\begin{pmatrix} d_{11} & d_{12} & d_{13} & d_{14} & d_{15} & d_{16} \\ d_{21} & d_{22} & d_{23} & d_{24} & d_{25} & d_{26} \\ d_{31} & d_{32} & d_{33} & d_{34} & d_{35} & d_{36} \end{pmatrix}. \tag{2}$$

The constitutive equations can be defined in strain, *S*,—charge, *D*, form as

$$\begin{aligned} S_I &= s^E_{IJ}T_J + d_{kI}E_k \\ D_i &= d_{iJ}T_J + \varepsilon^T_{ij}E_j \end{aligned} \tag{3}$$

where s^E is the elastic compliance tensor (4^{th} rank, 21 independent coefficients) at constant electric field, E, and ε^T—permittivity tensor (2^{nd} rank, 6 independent coefficients) at constant stress, T. These equations be also written in the form of stress-charge

$$\begin{aligned} T_I &= c^E_{IJ}S_J + e_{kI}E_k \\ D_i &= e_{iJ}S_J + \varepsilon^s_{ij}E_j \end{aligned} \tag{4}$$

where c^E is an elastic stiffness at constant field (4^{th} rank tensor like the compliance one) and e is a stress piezoelectric tensor. The stress and strain piezoelectric coefficients e and d are related by

$$e_{iJ} = d_{iL}c^E_{LJ}. \tag{5}$$

There are three operational modes in piezoelectric transduction:

- Longitudinal excitation (thickness mode)—the material is deformed parallel to the electric field (or stress is parallel to the dielectric displacement axis). This excitation is represented by d_{iI} ($i = I = 1,2,3$) coefficient. In the case of ferroelectric materials, if it is along the spontaneous polarization direction, d_{33} will be used.
- Transverse excitation (transverse mode)—the material is excited with respect to the dielectric displacement, represented by d_{iJ} coefficient with $i \neq J$ ($i,J = 1,2,3$).
- Shear excitation (shear mode)—the material is excited under shear boundary conditions, so the relative piezoelectric coefficient is d_{iJ} with $i = 1,2,3$ and $J = 4,5,6$.

2.2. Symmetry

According to Neumann's principle, the symmetry of the material structure reduces the number of independent components of tensors describing the physical properties, which cannot be less symmetric than the crystal structure. In crystallography, the standard unit cells and their axes are placed with respect to the principal symmetry elements and are specific to each crystal system (see table 1 for more details). The relationship between *XYZ* coordinates used for the tensors, and the standard crystallographic unit cell axis is summarized in table 1.

Ferroelectricity (switch of spontaneous polarization) can be present only in the materials which have nonzero physical properties presented by the first rank tensors (vector) like pyroelectricity. It is important to stress that the symmetry reasoning is obligatory but not sufficient condition for the presence of the ferroelectric properties. The materials containing center of the symmetry, improper rotation axis, cubic symmetry, or more than one rotation axis do not present 1st rank tensor properties. Only ten point groups present such properties: 1, m, 2, mm2, 4, 4mm, 6, 6mm, 3, 3m. In the triclinic point group, 1, which does not contain any symmetry all three vector (1^{st} ransk tensor) components (p_1, p_2, p_3) are not zero. The symmetry elements in the monoclinic symmetry are placed with respect to the *b*-axis of the unit cell. Therefore, the m point group presents vector properties $(p_1, 0, p_3)$ and 2 point group—$(0, p_2, 0)$. Only p_3 component is not zero for all other point groups with non-zero 1st rank properties which corresponds to the *c*-axis of the unit cell, placed along unique rotational symmetry axis.

The centrosymmetric point groups and 432 point group are not piezoelectric and not pyroelectric/ferroelectric. Although 20 point groups from 32 point groups present piezoelectric properties, the most studied piezoelectric materials are represented only in few point groups: 3m ($LiNbO_3$ (LN), $LiTaO_3$ (LT), $BiFeO_3$ (BFO)), 32 (Quartz, Langasite(LGS)), 6mm (AlN, ZnO), 4mm ($BaTiO_3$ (BTO), $KTa_xNb_{1-x}O_3$ (KTN_x) with $0.5 < x < 0.6$), mm2 (PZT-4 single crystal, $KNbO_3$ (KN)). The tensors describing piezoelectric, elastic and dielectric properties of single-crystal materials represented by these point groups are summarized in table 1. The point group 32 contains only two independent piezoelectric coefficients, 4mm and 6mm–3, 3m–4, and mm2–5 independent coefficients. Similar tendency on number of independent coefficients is observed for the other rank tensors. The stress and strain piezoelectric coefficients, compliance, stiffness, stress dielectric constants of the key piezoelectric materials are given in the Supplementary Material. The geometrical representation of the permittivity, the piezoelectricity and the elastic stiffness of LN, quartz, ZnO, $KTN_{0.53}$, KN are given in the figure 1. The permittivity of hexagonal, trigonal, and tetragonal materials can be defined by only two independent coefficients and this

Table 1. Piezoelectric, elastic stiffness/compliance and permittivity tensors of single crystals with 3m, 32, 6mm, 4mm, and mm2 point groups. The relationship between key symmetry elements, unit cell axis and *XYZ* reference coordinate system, used for tensor description, is indicated. Note that in the case of hexagonal and trigonal symmetries there is a difference between stiffness and compliance tensors as indicated below [23].

3m

Standard hexagonal cell: $a_h = b_h$, $\alpha_h = \beta_h = 90^\circ$, $\gamma_h = 120^\circ$
and 3 $\| c$, m $\perp$ (a, b)
XYZ coordinate system: $x \| a$ & $z \| c$, & $y \perp (x, z)$

Piezoelectric tensor

$$\begin{pmatrix} 0 & 0 & 0 & 0 & d_{15} & -2d_{22} \\ -d_{22} & d_{22} & 0 & d_{15} & 0 & 0 \\ d_{31} & d_{31} & d_{33} & 0 & 0 & 0 \end{pmatrix}$$

$e_{16} = -e_{22}$

Permittivity tensor

$$\begin{pmatrix} \varepsilon_{11} & 0 & 0 \\ 0 & \varepsilon_{11} & 0 \\ 0 & 0 & \varepsilon_{33} \end{pmatrix}$$

Stiffness and compliance tensors

$$\begin{pmatrix} c_{11} & c_{12} & c_{13} & c_{14} & 0 & 0 \\ c_{12} & c_{11} & c_{13} & -c_{14} & 0 & 0 \\ c_{13} & c_{13} & c_{33} & 0 & 0 & 0 \\ c_{14} & -c_{14} & 0 & c_{44} & 0 & 0 \\ 0 & 0 & 0 & 0 & c_{44} & c_{14} \\ 0 & 0 & 0 & 0 & c_{14} & 0.5 * (c_{11} - c_{12}) \end{pmatrix}$$

$s_{66} = 2(s_{11} - s_{12})$ & $s_{56} = s_{65} = 2s_{14}$

32

Standard hexagonal cell: $a_h = b_h$, $\alpha_h = \beta_h = 90^\circ$, $\gamma_h = 120^\circ$
and 3 $\| c$, 2$\|$ (a, b) & 2$\|$ [110]
XYZ coordinate system: $x \| a$ & $z \| c$, & $y \perp (x, z)$

Piezoelectric tensor

$$\begin{pmatrix} d_{11} & -d_{11} & 0 & d_{14} & 0 & 0 \\ 0 & 0 & 0 & 0 & -d_{14} & -2d_{11} \\ 0 & 0 & 0 & 0 & 0 & 0 \end{pmatrix}$$

$e_{26} = -e_{11}$

Permittivity tensor

$$\begin{pmatrix} \varepsilon_{11} & 0 & 0 \\ 0 & \varepsilon_{11} & 0 \\ 0 & 0 & \varepsilon_{33} \end{pmatrix}$$

Stiffness and compliance tensors

$$\begin{pmatrix} c_{11} & c_{12} & c_{13} & c_{14} & 0 & 0 \\ c_{12} & c_{11} & c_{13} & -c_{14} & 0 & 0 \\ c_{13} & c_{13} & c_{33} & 0 & 0 & 0 \\ c_{14} & -c_{14} & 0 & c_{44} & 0 & 0 \\ 0 & 0 & 0 & 0 & c_{44} & c_{14} \\ 0 & 0 & 0 & 0 & c_{14} & 0.5(c_{11} - c_{12}) \end{pmatrix}$$

$s_{66} = 2(s_{11} - s_{12})$ & $s_{56} = s_{65} = 2s_{14}$

6mm

Standard hexagonal cell: $a_h = b_h$, $\alpha_h = \beta_h = 90^\circ$, $\gamma_h = 120^\circ$
and 6 $\| c$, m $\perp$ (a, b), m $\|$ (a, b)
XYZ coordinate system: $x \| a$ & $z \| c$, & $y \perp (x, z)$

Piezoelectric tensor

$$\begin{pmatrix} 0 & 0 & 0 & 0 & d_{15} & 0 \\ 0 & 0 & 0 & d_{15} & 0 & 0 \\ d_{31} & d_{31} & d_{33} & 0 & 0 & 0 \end{pmatrix}$$

Permittivity tensor

$$\begin{pmatrix} \varepsilon_{11} & 0 & 0 \\ 0 & \varepsilon_{11} & 0 \\ 0 & 0 & \varepsilon_{33} \end{pmatrix}$$

(Continued.)

Table 1. (Continued.)

Stiffness and compliance tensors

$$\begin{pmatrix} c_{11} & c_{12} & c_{13} & 0 & 0 & 0 \\ c_{12} & c_{11} & c_{13} & 0 & 0 & 0 \\ c_{13} & c_{13} & c_{33} & 0 & 0 & 0 \\ 0 & 0 & 0 & c_{44} & 0 & 0 \\ 0 & 0 & 0 & 0 & c_{44} & 0 \\ 0 & 0 & 0 & 0 & 0 & 0.5(c_{11}-c_{12}) \end{pmatrix}$$

$$s_{66} = 2(s_{11} - s_{12})$$

4mm

Standard tetragonal cell: $a = b$, $\alpha = \beta = \gamma = 90^\circ$
And 4 $\parallel c$, m $\perp$ (a, b), m$\perp$[110] & m$\perp$[1$\bar{1}$0]
XYZ coordinate system: $x \parallel a$, $y \parallel b$, & $z \parallel c$

Piezoelectric tensor

$$\begin{pmatrix} 0 & 0 & 0 & 0 & d_{15} & 0 \\ 0 & 0 & 0 & d_{15} & 0 & 0 \\ d_{31} & d_{31} & d_{33} & 0 & 0 & 0 \end{pmatrix}$$

Permittivity tensor

$$\begin{pmatrix} \varepsilon_{11} & 0 & 0 \\ 0 & \varepsilon_{11} & 0 \\ 0 & 0 & \varepsilon_{33} \end{pmatrix}$$

Stiffness and compliance tensors

$$\begin{pmatrix} c_{11} & c_{12} & c_{13} & 0 & 0 & 0 \\ c_{12} & c_{11} & c_{13} & 0 & 0 & 0 \\ c_{13} & c_{13} & c_{33} & 0 & 0 & 0 \\ 0 & 0 & 0 & c_{44} & 0 & 0 \\ 0 & 0 & 0 & 0 & c_{44} & 0 \\ 0 & 0 & 0 & 0 & 0 & c_{66} \end{pmatrix}$$

mm2

Standard orthorhombic cell: $\alpha = \beta = \gamma = 90^\circ$
and m$\perp a$, m$\perp b$, m$\perp c$, in general $c < a < b$, but in ferroelectrics
always $c \parallel$ polarization axis independently of lattice parameters
XYZ coordinate system: $x \parallel a$, $y \parallel b$, & $z \parallel c$

Piezoelectric tensor

$$\begin{pmatrix} 0 & 0 & 0 & 0 & d_{15} & 0 \\ 0 & 0 & 0 & d_{24} & 0 & 0 \\ d_{31} & d_{32} & d_{33} & 0 & 0 & 0 \end{pmatrix}$$

Permittivity tensor

$$\begin{pmatrix} \varepsilon_{11} & 0 & 0 \\ 0 & \varepsilon_{22} & 0 \\ 0 & 0 & \varepsilon_{33} \end{pmatrix}$$

Stiffness and compliance tensors

$$\begin{pmatrix} c_{11} & c_{12} & c_{13} & 0 & 0 & 0 \\ c_{12} & c_{22} & c_{23} & 0 & 0 & 0 \\ c_{13} & c_{23} & c_{33} & 0 & 0 & 0 \\ 0 & 0 & 0 & c_{44} & 0 & 0 \\ 0 & 0 & 0 & 0 & c_{55} & 0 \\ 0 & 0 & 0 & 0 & 0 & c_{66} \end{pmatrix}$$

results in highly symmetric geometrical representation (ellipsoid). The orthorhombic symmetry is represented by three permittivity coefficients and the double ellipsoid space distribution. The key symmetry elements can be easily identified in the piezoelectric tensor geometrical representation. One can note the difference between the elastic stiffness and compliance representations in the space (figures 1 and 2, respectively), related by

$$c_{IJ}s_{KL} = 1. \tag{6}$$

One can also note some similarities in geometrical representations of the elastic compliance and piezoelectricity.

It is important to note that in the case of orthorhombic $KNbO_3$, two conventions are used to define the XYZ tensor axis with respect to the unit cell axis: the crystallographic one (defined in the table 1) and the optics one, in which X-axis is aligned along b-axis and Y-axis—along a-axis (figure 3) [21]. In this work, we use the crystallogarphic settings ($x \parallel a$, $y \parallel b$, & $z \parallel c$) in which unit cell parameters are

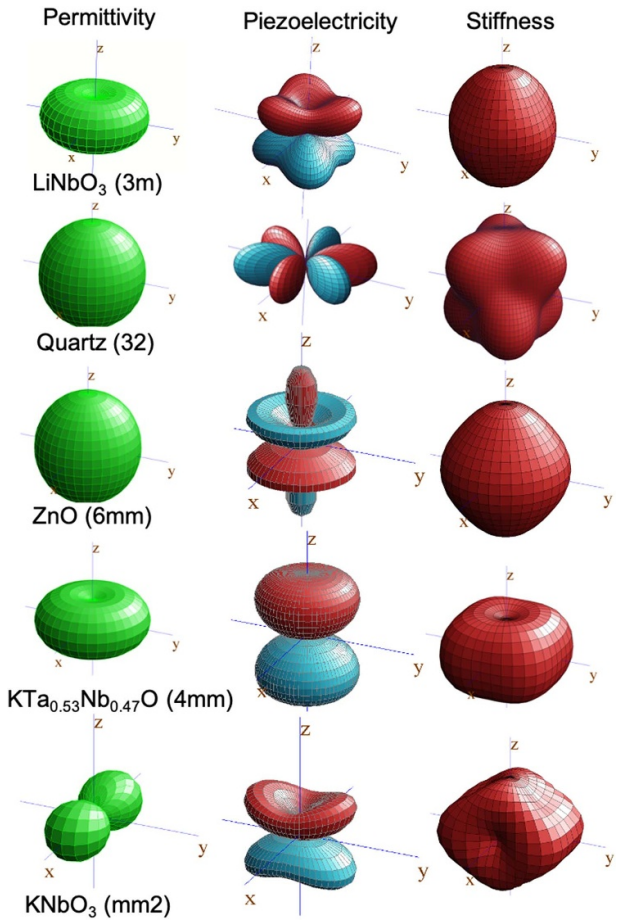

Figure 1. Geometrical representations of permittivity, ε_{ij}, piezoelectric, d_{iJ}, and elastic stiffness, c_{JK} of LN, quartz, ZnO, $KTN_{0.53}$ and KN representing different point groups.

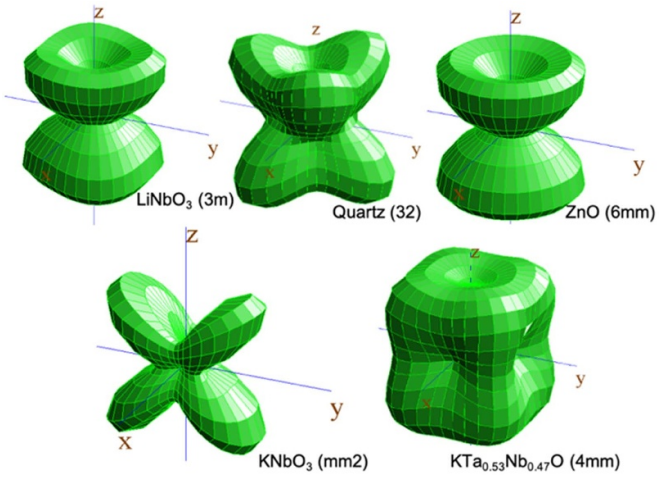

Figure 2. Geometrical representations of elastic compliance, s_{JK} of LN, quartz, ZnO, $KTN_{0.53}$ and KN representing different point groups. refaire.

$a = 3.974$ Å, $b = 5.695$ Å, and $c = 5.72$ Å, and the c-axis is parallel to the spontaneous polarization axis (figure 3). We would like to stress that in many papers and x-ray diffraction databases, it can be found the identification of othorhombic unit cell axis according to the rule $c < a < b$ without taking into account the polarization axis and therefore the point group is renamed m2m instead of mm2, as spontaneous polarization axis allowed by the symmetry only along the twofold symmetry axis.

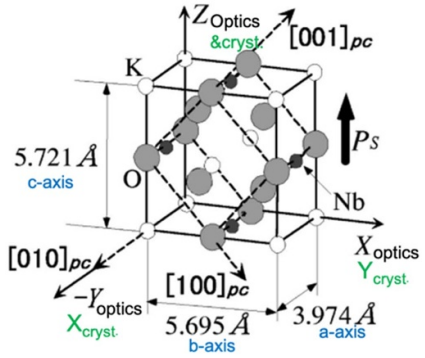

Figure 3. Illustration of identifications of X, Y, and Z-axes of orthorhombic $KNbO_3$ with respect to the a-, b-, and c-axes of orthrorhombic unit cell, used in optics and in crystallography. The realtionship between orthorhombic and pseudocubic (PC) unit cell is illustrated, as well. Reprinted from [22], with the permission of AIP Publishing.

Table 2. The equivalent planes of hexagonal, rhombohedral and peeudocubic unit cells used for the trigonal crystal system.

Hexagonal	Rhombohedral	Pseudocubic
(012)	(110)	(100)
(104) & (110)	(211) & $(10\bar{1})$	(110)
(006) & (202)	(222) & (200)	(111)
(116) & (122)	(321) & $(21\bar{1})$	(210)
(018) (214) (300)	(332), (310) & $(2\bar{1}\bar{1})$	(211)

In literature, nonstandard pseudocubic unit cells are frequently used for the trigonal and orthorhombic symmetries. In particular, the orientation of the perovskite material families based on (K,Na)(Nb,Ta)O_3, $BaTiO_3$, $BiFeO_3$ and their derivatives can be found frequently defined in pseudocubic settings. As KTN and BTO family materials present trigonal-orthorhombic-tetragonal-cubic phase transitions, the pseudocubic unit cell is used for all symmetries for convenience. Although, the axis of both tetragonal and pesudocubic cells coincide.

In the case of the trigonal crystal system, the standard unit cell is hexagonal, although these materials do not present sixfold symmetry. In addition to the pseudocubic cell, the rhombohedral cell is frequently used for the trigonal crystal class, as well. The families of equivalent planes of the rhombohedral, hexagonal and pseudocubic unit cells are summarized in the table 2. The (0001) planes of hexagonal cell are parallel to (111) pseudocubic and rhombohedral planes. The $\{100\}_{\mathrm{PC}}$ pseudocubic planes are parallel to the $\{01\bar{1}2\}_{\mathrm{H}}$ hexagonal planes, and $\{110\}_{\mathrm{PC}} \parallel \{11\bar{2}0\}_{\mathrm{H}}$.

In the case of the orthorhombic crystal system, the orthorhombic a-axis (X-axis in tensor notation), [100], councides with b-axis of pseudocubic cell (figure 3). The pseudocubic a- and c-axes are rotated from b-and c-orthorhombic ones by 45° around a-axis. We would like to

stress that if the optics settings are used the orthorhombic *a*-axis is parallel to -*Y* tensor axis but it still coincides with *b*-axis of pseudocubic cell.

If the physical properties of orthorhombic and trigonal/hexagonal materials are characterized/described in the pseudo-cubic settings, all rank tensors, defined in standard settings (table 1), have to be rotated by using these transformation matrices:

$$\begin{pmatrix} 1 & 0 & 0 \\ 0 & \sqrt{2}/2 & \sqrt{2}/2 \\ 0 & -\sqrt{2}/2 & \sqrt{2}/2 \end{pmatrix} \tag{7}$$

$$\text{and} \begin{pmatrix} 1 & 0 & 0 \\ 0 & \cos\phi & \sin\phi \\ 0 & -\sin\phi & \cos\phi \end{pmatrix}, \text{ respectively} \tag{8}$$

where angle φ corresponds to the angle between $(0001)_{\mathrm{H}}$ and $\left(01\bar{1}2\right)_{\mathrm{H}}$ planes of hexagonal cell (rotation around X-axis in a right handed side from Z-axis). The rotated 3rd rank tensors for the mm2 and 3m point groups can be found in the supplementary material. For example, in the case of 3m point group, if the $(100)_{\mathrm{PC}}$ oriented material in pseudocubic settings (corresponding to $\left(10\bar{1}2\right)$ plane of the hexagonal unit cell) is characterized in thickness and transverse modes, the related effective piezoelectric coefficients, d'_{33} and d'_{31} will be a product of the several piezoelectric constants:

$$\begin{aligned} d'_{33} = &\cos\varphi\left(d_{22}\cos^2\varphi + d_{15}\cos\varphi\sin\varphi\right) \\ &+ \sin\varphi\left(d_{31}\cos^2\varphi + d_{33}\sin^2\varphi\right) \text{ and} \end{aligned} \tag{9}$$

$$d'_{31} = d_{22}\sin\varphi + d_{31}\cos\varphi, \text{ respectively.} \tag{10}$$

In the case of the pseudocubic settings used for the orthorhombic system, the d'_{33} and d'_{31} will be defined as follows

$$d'_{31} = \sqrt{2}/2 d_{31}, d'_{32} = \sqrt{2}/2\left(-d_{24} + d_{32} + d_{33}\right), \tag{11}$$

$$\text{And } d'_{33} = \sqrt{2}/4\left(d_{32} + d_{33} + d_{24}\right). \tag{12}$$

For convenience, if the material is not oriented along standard *X, Y* and *Z*-axes, the tensors are transformed and the effective tensor coefficients are used, which are the products of different coefficients. The crystals are rotated along different axes to maximize their effective coefficients and to optimize the device performance. The 3D representation of the effective d'_{31} and d'_{33} coefficients of LN, ZnO, $KTN_{0.53}$ and KN are given in figures 4 and 5, respectively. One can note that efficient coefficients are highly dependent on the symmetry and the direction/material orientation. The d_{33} and d_{31} coefficients are compared to the maximum effective d'_{31} and d'_{33} coefficients of different materials in table 3. One can note that in the case of 6mm and 4mm point groups the maximum effective d'_{31} and d'_{33} coefficients correspond to Z orientation (*c*-axis) and they are equal to the d_{31} and d_{33} in standard settings. The

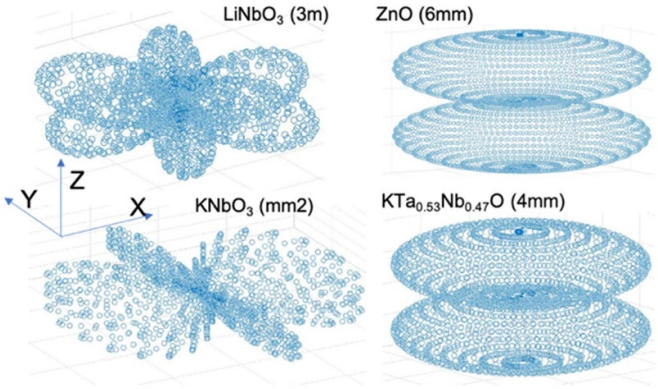

Figure 4. 3D representation of the effective d'_{31} coefficient of LN, ZnO, $KTN_{0.53}$ and KN in the *XYZ* coordinate system. The definition of *XYZ* directions for different point groups can be found in the table 1.

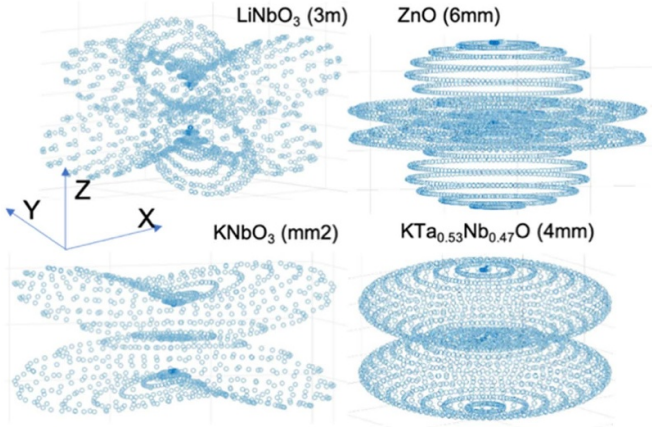

Figure 5. 3D representation of the effective d'_{33} coefficient of LN, ZnO, $KTN_{0.53}$ and KN in the *XYZ* coordinate system. The definition of *XYZ* directions for different point groups can be found in the table 1.

d'_{33} coefficient of $KNbO_3$ can be increased by a factor of three if the (011) plane orientation is considered instead of (001) in the orthorhombic cell. The (011) plane in orthorhombic cell is equivalent to (100) plane in the pseudocubic cell. The d_{33} of LN is only 6 pC N^{-1}, but this coefficient can be maximized to 39.5 pC N^{-1} if the $\left(10\bar{1}2\right)$ orientation tilted by 4.8° is considered. The maximum effective d'_{31} of LN is attained for the *Y*-cut ($(10\bar{1}0)$ plane of hexagonal cell). Therefore, the characterization or comparison of materials have to be done in the standard settings to avoid any confusion and they should include maximum effective coefficient comparison, as well.

2.3. Curie point groups and thin films

The tensors, given in the table 1, are valid only for the materials with single crystalline orientation. The presence of growth domains, a texture or a polycrystallinity has to be taken into account due to coexistence of several orientations. For example, perfectly polycrystalline and textured (the orientation is defined only along a single axis) materials (figure 6)

Table 3. Comparison of d_{33} and d_{31} coefficients in standard settings with maximum efficient d'_{33} and d'_{31} coefficients obtained at specific orientations of frequently studied piezoelectric materials representing different point groups. The closest crystallographic planes and rotation angles (θ—counterclockwise rotation around X-axis, ϕ—counterclockwise rotation around Z-axis) corresponding to the maximum performance are indicated, as well.

Point group	Material	d_{33}	max d_{33} (pC N^{-1})	max K_{33} (%)	d_{31}	max d_{31} (pC N^{-1})	max K_{31} (%)
3m	$LiNbO_3$	6	39.5 $\theta = 62°$ $\phi = 60°$ $(10\bar{1}2)$ $+4.8°$	38.4 $\theta = 123°$ $\phi = 120°$ $(10\bar{1}2)$ $+3.7°$	−1	−21.0 $\theta = 93°$ $\phi = 240°$ $(10\bar{1}0)$ $+3°$	10.2 $\theta = 82°$ $\phi = 180°$ $(10\bar{1}0)$ $-8°$
	$LiTaO_3$	8.2	14.6 $\theta = 56°$ $\phi = 60°$ $(10\bar{1}2)$ $-1°$	15.2 $\theta = 61°$ $\phi = 60°$ $(10\bar{1}2)$ $+3.8°$	−3.2	−7.3 $\theta = 106°$ $\phi = 120°$ (201) +6.8	4.0 $\theta = 71°$ $\phi = 300°$ (011) $-1°$
32	Quartz	0	−2,3 $(2\bar{1}\bar{1}0)$	1.0	0	2.3 $(2\bar{1}\bar{1}0)$	1.0
∞m	PZT-4Ceram.	289	289 (001)	46.2	−123	−123 (001)	10.9
4mm	$KTa_{0.53}Nb_{0.47}O_3$	132	132 (001)	47.6	−42	−42 (001)	10.9
6mm	AlN	5	5 (0001)	7.3	−2	−2 (0001)	1.2
	ZnO	12.4	12.4 (0001)	16.0	−5	−5 (0001)	2.6
mm2	$KNbO_3$	29.3	89.3 $\theta = 51°$ (011) $+5.8°$	70.6 $\theta = 46°$ (011) $+0.8°$	19.4	−19.4 (001)	19.4

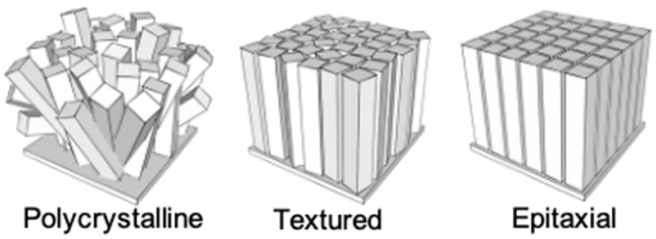

Figure 6. Schematic illustration of polycrystalline, textured and epitaxial materials.

will be described by the ∞∞m and ∞/mm Curie groups, respectively. In the case of the polycrystalline ferroelectric materials, the polarization of different domains can be aligned by applying an external electric field, usually applied above the Curie temperature and kept during cooling down to room temperature (RT). This electrical poling procedure allows obtaining textured ferroelectric ceramics with single direction of the polarization axis. The poled ceramics are described by symmetry of ∞m Curie group (poled ceramics for example PZT-4 or KNN). The general descriptions of elasticity, permittivity and piezoelectricity tensors of ∞∞m, ∞/mm and ∞m point groups are summarized in the table 4.

In the case of the epitaxial thin films, the growth domains may be present. In many cases, the effect of the growth domains on the tensor representation of properties can be taken into account by considering that the growth domains introduce an additional symmetry element. For example if the (001) orthorhombic thin film (point group mm2) is grown epitaxially on (001) cubic substrate, the film will contain at least four growth domains rotated by 90° in the substrate plane. These growth domains introduce a fourfold rotational symmetry axis along [001] axis at microscale, which can be representation by transformation matrix:

$$\begin{pmatrix} 0 & \bar{1} & 0 \\ 1 & 0 & 0 \\ 0 & 0 & 1 \end{pmatrix}. \tag{13}$$

The fourfold axis transforms X axis (coefficient 1) to -Y axis (- coefficient 2), Y (2) to X (1), and z-axis remains unchanged (coefficient 3). Thus, after applying fourfold rotational symmetry the piezoelectric tensor of mm2 point group (see table 1) will transform as follows (note that for the transformation we need to use tensor notation instead of matrix notation):

$$\begin{aligned} d_{31} = d_{311} &=> d_{322} = d_{32} \\ d_{32} = d_{322} &=> d_{311} = d_{31} \\ d_{33} = d_{333} &=> d_{333} = d_{33} \\ d_{24} = d_{223} &=> d_{113} = d_{15} \\ d_{15} = d_{113} &=> d_{223} = d_{24} \end{aligned}$$

The symmetry implies that the initial tensor and the tensor after symmetry application have to be equal. Therefore, the

Table 4. Piezoelectric, elastic stiffness and permittivity tensors of materials with $\infty\infty$m, ∞/mm and ∞m point groups. The relationship between key symmetry elements, unit cell axis and *XYZ* reference coordinate system, used for tensor description, is indicated. The difference between compliance and stiffness tensors is indicated, as well.

XYZ coordinate system: no constraints	
Piezoelectric tensor	Permittivity tensor
$\begin{pmatrix} 0 & 0 & 0 & 0 & 0 & 0 \\ 0 & 0 & 0 & 0 & 0 & 0 \\ 0 & 0 & 0 & 0 & 0 & 0 \end{pmatrix}$	$\begin{pmatrix} \varepsilon_{11} & 0 & 0 \\ 0 & \varepsilon_{11} & 0 \\ 0 & 0 & \varepsilon_{11} \end{pmatrix}$
Stiffness and compliance tensors	
$\begin{pmatrix} c_{11} & c_{12} & c_{12} & 0 & 0 & 0 \\ c_{12} & c_{11} & c_{12} & 0 & 0 & 0 \\ c_{12} & c_{12} & c_{11} & 0 & 0 & 0 \\ 0 & 0 & 0 & c_{44} & 0 & 0 \\ 0 & 0 & 0 & 0 & c_{44} & 0 \\ 0 & 0 & 0 & 0 & 0 & c_{44} \end{pmatrix}$, $c_{44} = 0.5(c_{11} - c_{12})$ $s_{44} = 2(s_{11} - s_{12})$	
∞/mm	
And $\infty \parallel c$, m $\perp c$, m $\perp$ (*a, b*) *XYZ* coordinate system: $z \parallel c$	
Piezoelectric tensor	Permittivity tensor
$\begin{pmatrix} 0 & 0 & 0 & 0 & 0 & 0 \\ 0 & 0 & 0 & 0 & 0 & 0 \\ 0 & 0 & 0 & 0 & 0 & 0 \end{pmatrix}$	$\begin{pmatrix} \varepsilon_{11} & 0 & 0 \\ 0 & \varepsilon_{11} & 0 \\ 0 & 0 & \varepsilon_{33} \end{pmatrix}$
Stiffness and compliance tensors	
$\begin{pmatrix} c_{11} & c_{12} & c_{13} & 0 & 0 & 0 \\ c_{12} & c_{11} & c_{13} & 0 & 0 & 0 \\ c_{13} & c_{13} & c_{33} & 0 & 0 & 0 \\ 0 & 0 & 0 & c_{44} & 0 & 0 \\ 0 & 0 & 0 & 0 & c_{44} & 0 \\ 0 & 0 & 0 & 0 & 0 & c_{66} \end{pmatrix}$, $c_{66} = 0.5(c_{11} - c_{12})$ $s_{66} = 2(s_{11} - s_{12})$	
∞m	
$\infty \parallel c$, m $\perp$ (*a, b*) *XYZ* coordinate system: $z \parallel c$	
Piezoelectric tensor	Permittivity tensor
$\begin{pmatrix} 0 & 0 & 0 & 0 & d_{15} & 0 \\ 0 & 0 & 0 & d_{15} & 0 & 0 \\ d_{31} & d_{31} & d_{33} & 0 & 0 & 0 \end{pmatrix}$	$\begin{pmatrix} \varepsilon_{11} & 0 & 0 \\ 0 & \varepsilon_{11} & 0 \\ 0 & 0 & \varepsilon_{33} \end{pmatrix}$
Stiffness and compliance tensors	
$\begin{pmatrix} c_{11} & c_{12} & c_{13} & 0 & 0 & 0 \\ c_{12} & c_{11} & c_{13} & 0 & 0 & 0 \\ c_{13} & c_{13} & c_{33} & 0 & 0 & 0 \\ 0 & 0 & 0 & c_{44} & 0 & 0 \\ 0 & 0 & 0 & 0 & c_{44} & 0 \\ 0 & 0 & 0 & 0 & 0 & c_{66} \end{pmatrix}$, $c_{66} = 0.5(c_{11} - c_{12})$ $s_{66} = 2(s_{11} - s_{12})$	

fourfold symmetry axis along Z-axis results in $d_{31} = d_{32}$ and $d_{15} = d_{24}$. The piezoelectric tensor of (001) orthorhombic film with four growth domains rotated by 90° in the substrate plane would be

$$\begin{pmatrix} 0 & 0 & 0 & 0 & d_{15} & 0 \\ 0 & 0 & 0 & d_{15} & 0 & 0 \\ d_{31} & d_{31} & d_{33} & 0 & 0 & 0 \end{pmatrix} \quad (14)$$

where d_{31} (d_{15}) of such film is theoretically an average value of d_{32} and d_{31} (d_{15} and d_{24}) of bulk material. It is important to note that this tensor is valid only for the films without ferroelectrics domains. If the ferroelectric domains are present, it results in the inversion symmetry and the transformation of Z axis (3) to $-Z$ axis (-3), $Y(2)$ to $-Y(-2)$ and $X(1)$ to $-X(-1)$ and consequently all the piezoelectric coefficients with opposite sign. If the material contains equal proportions of Z+ and Z− domains, the piezoelectric properties and all other 3rd and 1st rank tensor properties are zero. However, this proportion is never perfectly 50% and therefore polydomain samples still present weak piezoelectric properties. In the case of perfectly polycrystalline materials the 1 and 3 rank tensor properties including piezoelectric and pyroelectric ones are zero. The films rarely are perfectly polycrytalline and in most cases present preferential texture. In the films containing several orientations, the coefficients have to be estimated for each present orientation by tranforming the tensor and then, each coefficients is averaged for all orientations by taking into account of the volume fractions of each orientation.

One can note that the properties of the same material in the form of a single crystal, a thin film and ceramics will not necessarily be presented by the same tensor description and are highly dependent on the microstructure. For example, the piezoelectric (d in pC N^{-1}) tensor of $BiFeO_3$ can be represented by:

- Single-domain single crystal or single crystalline (0001) film (3m point group)

$$\begin{pmatrix} 0 & 0 & 0 & 0 & -62 & 43.6 \\ 21.8 & -21.8 & 0 & -62 & 0 & 0 \\ -3.7 & -3.7 & -16 & 0 & 0 & 0 \end{pmatrix}. \quad (15)$$

- Poled ceramics, poled (0001) textured or containing growth domains rotated in the substrate plane films ((111) pseudocubic orientation)

$$\begin{pmatrix} 0 & 0 & 0 & 0 & -62 & 0 \\ 0 & 0 & 0 & -62 & 0 & 0 \\ -3.7 & -3.7 & -16 & 0 & 0 & 0 \end{pmatrix}. \quad (16)$$

- $(01\bar{1}2)$ oriented single crystalline film ((100) pseudocubic orientation)

$$\begin{pmatrix} 0 & 0 & 0 & 0 & 2.9 & -125.8 \\ -23.3 & -30.5 & 34.0 & 1.9 & 0 & 0 \\ -25.3 & -25.8 & 64.4 & -11.0 & 0 & 0 \end{pmatrix}. \quad (17)$$

- $(01\bar{1}2)$ textured or epitaxial film with four in plane rotated domains

$$\begin{pmatrix} 0 & 0 & 0 & 0 & 2.4 & 0 \\ 0 & 0 & 0 & 2.4 & 0 & 0 \\ -25.6 & -25.6 & 64.4 & 0 & 0 & 0 \end{pmatrix}. \quad (18)$$

- Polycrystalline films without preferred orientation would have zero piezoelectric properties.

In the case of poled PZT ceramics or textured films (∞m Curie group), there are possible only three operational modes: longitudinal d_{33} mode, transverse d_{31} mode and bending-type d_{31} mode, where 3—is a polarization direction. In the case of the vibrational harvesting, using cantilevers, the 31 bending-type modes is considered, while in the static EH by applied pressure—d_{33} thickness mode. Therefore, the thin films and bulk piezoelectric materials are often compared in limited ways in terms of piezoelectric coefficients d_{31} and d_{33}. As shown above in the case of BFO, $d_{31} = -3.7$ pC N^{-1} and $d_{33} = -16$ pC N^{-1}, however if the $(01\bar{1}2)$ orientation is considered these coefficients are considerably increased ($d'_{31} = -25.6$ pC N^{-1} and $d'_{33} = 64.4$ pC N^{-1}). This demonstrates the importance of optimization of targeted coefficients by adapting the single crystal or thin film orientation.

2.4. Electromechanical coupling factor and FoM

The piezoelectric coefficients are important parameters, but they do not allow a definition of the electrical energy stored in the material under the strain. For this purpose an electromechanical coupling factor, K^2, has to be used. K^2 is defined by several physical properties such as piezoelectricity, permittivity and elasticity. The electro-mechanical coupling factor (nondimensional coefficient) describes the piezoelectric material's ability to convert the stored mechanical energy into an electric work

$$K^2 = \frac{\text{Created electrical energy}}{\text{Invested mechanical energy}}. \quad (19)$$

The theoretical K^2_{ij} of the material can be calculated for each excitation d_{ij} mode:

$$K^2_{iJ} = \frac{d^2_{iJ}}{s^E_{JJ}\varepsilon^T_{ii}}. \quad (20)$$

The 3D geometrical representations of the electromechanical coupling and the different coefficients K^2_{ij} of different piezoelectric materials belonging to different symmetry point groups are given in figure 7 and table 5. In the case of 6mm (ZnO, AlN) and 4mm point groups ($KTN_{0.53}$) the highest electromechanical coupling is present along Z-axis, which is defined by K^2_{33}. The quartz and LGS, representing the trigonal 32 point group, have the highest electromechanical efficiency along the X-axis corresponding to K^2_{11} factor. Orthorhombic $KNbO_3$ represents the maximum coupling in the {011} family planes with the main contribution of shear K^2_{24} coefficient. The shear electromechanical coupling, represented by K^2_{24} and K^2_{15} coefficients, are also dominating in the

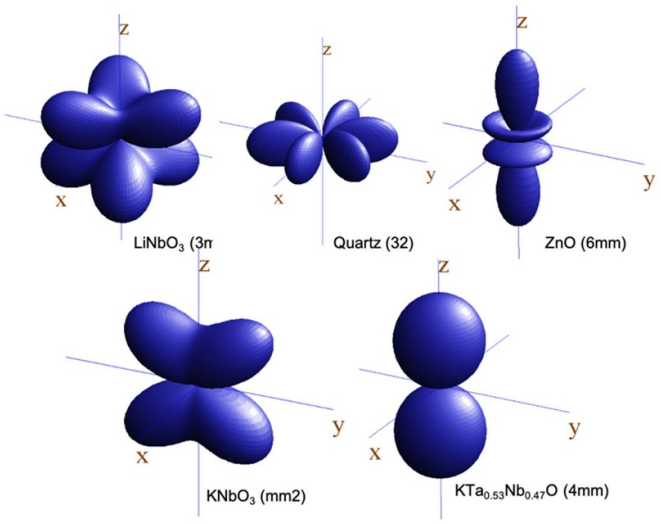

Figure 7. 3D geometrical representation of the electromechanical coupling of $LiNbO_3$, quartz, ZnO, $KNbO_3$ and KTN_{53}.

Table 5. Electromechanical coupling coefficients K^2_{ij} in standard *XYZ* settings (see tables 1 and 4 for the relationships with unit cell axis) of different piezoelectric materials belonging to different point groups.

Point group	Material	K^2_{11}	K^2_{22}	K^2_{33}	K^2_{31}	K^2_{32}	K^2_{14}	K^2_{15}	K^2_{24}
32	Quartz	1.0					0.06		
	LGS	1.3					0.6		
3m	$LiNbO_3$		10.2	2.9	0.1	0.1		37.2	37.2
	$LiTaO_3$		2.3	3.6	0.3	0.3		13.7	13.7
	$BiFeO_3$		15.8	13.6	0.7	0.7		36.0	36.0
6mm	AlN			7.51	1.30	1.30		0.90	0.90
	ZnO			15.8	1.30	1.30		3.9	3.9
∞m	PZT-4[a]			46.5	10.7	10.7		49.0	49.0
4mm	KTN_{53}			47.6	7.9	7.9		20.5	20.5
mm2	$KNbO_3$			31.5	19.4	4.6		20.7	79.9

[a] Poled ceramics.

trigonal 3m point group ($LiNbO_3$, $LiTaO_3$, $BiFeO_3$). If the *Z*-axis (*c*-axis) oriented materials are considered, only $KNbO_3$-$KTaO_3$ family materials offer higher K^2_{33} than $K^2_{33} = 46.5\%$ of PZT-4 ceramics (table 5). The effective $K^{2'}_{33}$ of $KNbO_3$ can be further increased from 31.5% to 70.6% if the (011) orientation is considered instead of (001) one (table 3).

The $K^{2'}_{33}$ of $LiNbO_3$ can be optimized by rotating the crystal orientation & tensor, (the 3D representation of K^2_{33} of $LiNbO_3$ is given in figure 8) to find the optimal orientation as in [24]. The polarization is normally along *Z*-axis, and this leads to using d_{31} with parallel plate electrodes, or d_{33} with IDTs. But in the case of $LiNbO_3$, we are considering single crystal cuts that are rotated around *X*-axis. Generally, they are defined using IEEE standard [25] notation as (*YXl*)/Θ, which means that the piezoelectric plate has length (l) along *X*-axis, width along *Z*-axis, and a surface normal is being parallel to *Y*-axis. The rotation (Θ) is done around the *X*-axis starting from the *Y*-axis. For $LiNbO_3$, as shown in Nakamura's work

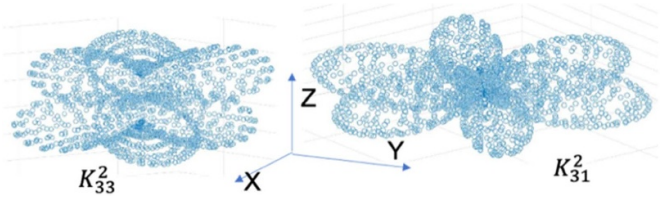

Figure 8. 3D representation of effective K^2_{33} and K^2_{31} electromechanical coupling factors of $LiNbO_3$. *XYZ* axes correspond to the standard tensor setting for 3m point group (see table 1).

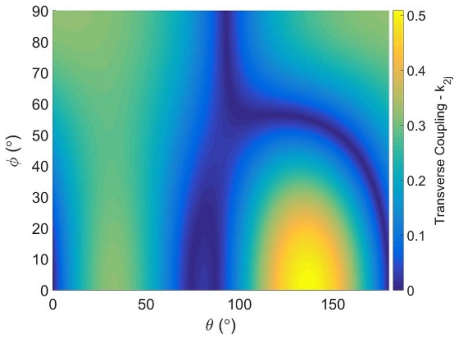

Figure 9. Optimization of effective transverse electromechanical coupling K'_{23} of $LiNbO_3$ by rotating around axis *X* by angle Θ and in the resulting plane XZ' by angle ϕ.

[26] the piezoelectric polarization can be projected along Y'-axis (i.e. rotated direction 2), while the length of the beam can be oriented along both *X*- or Z'-axis (i.e. directions 1, 3, respectively). Performing the rotation for the given angle in this notation gives the commonly known Y-rotated cuts. Nevertheless, in literature, sometime the reported orientation is named 32 [27, 28] or 31 [29]. Furthermore, a full theoretical study for Z-oriented $LiNbO_3$ is given by Yue and Yi-jiang in [24], where the notation adopted was the regular one with the investigation of $K^{2'}_{31}$ and $K^{2'}_{33}$. In particular, $LiNbO_3$ presents dielectric constant much lower than that of lead-based piezoelectric materials, which is very interesting in terms of electromechanical coupling. The high $K^{2'}_{33}$ (38.4%) can be attained for the $\left(01\bar{1}2\right)_H$ (or 33°Y in IEEE notation) oriented $LiNbO_3$ (table 3).

In the case of transverse mode, the *Z*-axis oriented $LiNbO_3$ has the lowest K^2_{31} from all the compared materials including polyvinylidene fluoride (PVDF) (table 6). It was shown in the section 2.2 and figures 7 and 8 that the highest piezoelectric response of $LiNbO_3$ is not aligned with respect to the unit cell *a*- and *c*-axis (*X* and *Z*-axis respectively). Similar performance to PZT-4 ($K^2_{31} = 10.2\%$, table 5) can be also obtained in Y-oriented $LiNbO_3$ (effective $K^{2'}_{31} = 10.2\%$, see table 3 and figure 8). If $K^{2'}_{23}$ for 137°Y $LiNbO_3$ orientation is considered, the transverse electromechanical coupling of $LiNbO_3$ can be further enhanced to 27.7% (figure 9), which is higher than PZT ceramics (table 6). The PMNT-PT and PZN-PT single crystals can offer much higher transverse coupling than $LiNbO_3$ single crystals, but these crystals contain lead, they are very expensive and are not produced in scale of wafers with large

Table 6. Comparison of transverse K_{31}^2, longitudinal K_{33}^2 and corresponding FoMs of piezoelectric materials for strain driven energy harvesters. The coefficients are given for the single-crystal materials with exception to ceramics of PZT-5H and PZT-5A, and polymer PVDF. ε_0 is the permittivity of the free space (8.85 pF m^{-1}). If it is not specified, the direction 3 corresponds to the *c*-axis of the standard unit cell (table 1) and the direction 1—*a*-axis.

Property	s_{11}^E	s_{11}^D	s_{33}^E	s_{33}^D		d_{31}	d_{33}	K_{31}^2	K_{33}^2	$\mathrm{FoM}_{31}^{\mathrm{S}}$	$\mathrm{FoM}_{33}^{\mathrm{S}}$
Units	pm^2 N^{-1}				$\frac{\varepsilon_{33}^{\mathrm{T}}}{\varepsilon_0}$	pC N^{-1}		%		kJ cm^{-3}	
AlN [31]	3.5	3.5	3.2	2.9	9.5	2	5.0	1.4	9.3	3.9	32.0
$BaTiO_3$ [32]	8.1	7.2	6.8	1.9	168	35	85.6	10.2	72.5	14.1	387.2
KNN-LT [33]	17.2	13.4	27	9.1	790	−163	354	22.2	66.4	16.5	73.1
KTN_{53}	5.8	1.7	9.5	5.0	435	−42	132	7.9	47.6	14.8	95.8
$KNbO_3$	5.1	−3.5	7.0	4.8	44	−19.5	29.3	19.1	31.5	46.4	65.7
(011)$KNbO_3$[a]	12.5	−0.3	12.5	3.7	95.2	−57.5	86.3	31.4	70.6	1194	191.3
BFO_{SC} [34–36]	7.8	4.9	6.1	5.3	29.1	−3.7	−16	0.7	16.3	1.3	31.9
$(10\bar{1}2)$BFO	7.8	4.3	16.7	5.6	42.1	−25.3	64.4	22.1	66.7	51.6	119.7
$(10\bar{1}4)$BFO[a]	16.7	1.8	8.6	5.6	35.0	34.1	−30.5	22.4	35.0	122.8	62.8
$LiNbO_3$ [37, 38]	5.8	5.2	5.1	5.0	28.9	−1.0	8.3	0.07	2.8	0.13	11
$LiNbO_3$ [38] (145° Y-cut)			6.9	4.4	67.7		−38.8		36.2		81.7
$LiNbO_3$ [38] (46° Y-cut)[a]	6.9	2.9			54.5	−27.9		23.4		80.8	
PMN-0.33PT [39]	69	36.3	120	11	8200	1540	2820	47.6	91.3	13.1	87.7
PZN-0.08PT [40]	87	55.9	140	17.4	7700	1455	2890	36.0	87.5	6.4	50.2
PZT-5A [41]	16.4	14.5	18.8	9.5	1700	171	374	11.6	49.5	8.2	52.0
PZT-5H	15.9	12.9	20.7	10.6	3935	320	593	19.4	48.8	14.3	46.0
PVDF [42, 43]	239	234	472	461	13	23.9	−35	2.0	2.3	0.09	0.05
ZnO [44]	7.9	7.6	6.8	5.2	11	−5.2	12.4	3.6	23.2	4.6	44.5

[a] Transverse 32 coefficients are given instead of 31 ones, s_{22} instead of s_{11}.

diameters (4–6 inches), which limits their implementation in real applications, while $LiNbO_3$ crystals with big diameters are grown by Czochralski technique and they can be diced in any desired orientation.

K_{31}^2 of *c*-axis oriented KNN-LT and $KNbO_3$ reaches the K_{31}^2 of PZT-5H (19.4%, see tables 5 and 6). $KNbO_3$ has very high shear K_{24}^2 electromechanical coupling (table 5), therefore the effective transverse coupling, $K_{32}^{2'}$, can be further increased to 31.4% by rotation to the diagonal of the plane 23 (corresponding to the coefficient 4 in matrix notation), which corresponds to the (011) orthorhombic crystal plane and by applying the stress along the new in-plane direction 2′ (perpendicular to the *X*-axis). $BiFeO_3$, belonging to the same point group as $LiNbO_3$, presents also highly anisotropic properties. The d_{31}, d_{32} and corresponding transverse couplings as a function of a rotation angle, Θ, around the *X*-axis are given in the figure 10. One can note very different change of the d'_{31} and d'_{32} coefficients as a function of the rotational angle. The maximum d'_{31} value is attained at around Θ = 80°, which corresponds to 10° tilted -Y-orientation (or $(\bar{1}010)$ planes). The d'_{32} reaches maximum at ∼ 52° (17° off the $(10\bar{1}4)_{\mathrm{H}}$ planes, which correspond to Θ = 35°). The highest effective transverse electromechanical coupling of lead-free materials is observed for the (011) $KNbO_3$ single crystals, which reaches $K_{32}^{2'}$ of 31% (table 6, figure 10) and becomes comparable to that of lead-based PZN-PT single-crystals.

Lead-based PMN-PT single crystals present the longitudinal K_{33}^2 as high as 91.3%. The PZT ceramics show also very high longitudinal electromechanical coupling (up to 49.5%). Nevertheless, the lead-free materials such as $BaTiO_3$, KNN-LT and (011) $KNbO_3$ can largely overpass the performance of lead-based ceramics and KTN crystals show comparable $K_{33}^{2'}$ to that of PZT (see table 6). The K_{33}^2 of $LiNbO_3$ is 2.8% and its optimized value reaches 38.4% for 51.6°Y-orientation, which remains below the highest performance of lead-based and lead-free materials. The $K_{33}^{2'}$ of $BiFeO_3$ is maximized to 69% at the Θ = 117° as shown in the figure 10 (8° off the $(10\bar{1}2)$ planes, which corresponds to Θ = 125°). One can note an important difference between the longitudinal coupling of $(10\bar{1}2)$ and $(10\bar{1}4)$ planes of $BiFeO_3$ (66% and 35%, respectively). Very similar angular dependence of $K_{33}^{2'}$ is also observed for the $LiNbO_3$, belonging to the same point group.

It is important to stress that the electromechanical coupling of the device is defined not only by the coupling of the piezoelectric material but also by the complete design of the device (electrode material/thickness/placement, other non-piezoelectric parts, etc) and in general, the K^2 of the device is smaller that the theoretical material K^2.

There are inertial and kinematic types of piezoelectric harvesters, which are driven by stress and by strain, respectively. The kinematic harvester performance is not dependent on the frequency and quality factor of the materials and it is directly linked to the deformation. The strain driven harvester $\mathrm{FoM}^{\mathrm{S}}$ is given as a function of piezoelectric, compliance and dielectric properties by

$$\mathrm{FoM}_{iJ}^{\mathrm{S}} = \frac{d_{iJ}^2}{s_{JJ}^E s_{JJ}^D \varepsilon_{ii}^{\mathrm{T}}} \tag{21}$$

where s_{JJ}^E and s_{JJ}^D are elastic compliance coefficients at constant field and dielectric displacement, respectively. In general, the s_{IJ}^D can be expressed as

Table 7. Comparison of transverse $K_{31}^{2\prime}$ and $\mathrm{FOM}^{\mathrm{T}}$ of piezoelectric materials for stress driven energy harvesters. The coefficients are given for the single-crystal materials with exception to ceramics of PZT-5H and PZT-5A, and polymer PVDF. ε_0 is the permittivity of the free space (8.85 pF m^{-1}). Q_m -mechanical quality factor. If it is not specified, the direction 3 corresponds to the c-axis of the standard unit cell (table 1) and the direction 1–a-axis.

Property Units	s_{11}^E pm^2 N^{-1}	$\frac{\varepsilon_{33}^{\mathrm{T}}}{\varepsilon_0}$	d_{31} pC N^{-1}	e_{31} C m^{-2}	K_{31}^2 %	$\mathrm{FoM}^{\mathrm{T}}$ kJ cm^{-3}	Q_m
AlN [31]	3.5	9.5	2	−0.58	1.4	4.0	10^3
$BaTiO_3$ [32]	8.1	168	35	0.68	10.2	0.3	400
KNN-LT [33]	17.2	790	−163	−6.28	22.2	5.6	—
KTN_{53}	5.8	435	−42	−5.2	7.9	7.0	
$KNbO_3$	5.1	44	−19.5	−1.1	19.1	3.2	
$BiFeO_{3,SC}$ [34–36]	7.8	29.1[a]	−3.7[a]	−2.28[a]	0.7	20.2	
$LiNbO_3$ [37, 38]	5.8	28.9	−1.0	0.30	0.07	0.35	10^4
$LiNbO_3$ (137° Y-cut)[b]	5.8	58	28.9	2.82	27.7	15.5	10^4
PMN-0.33PT [39]	69	8200	1540	−3.9	47.6	0.2	>100
PZN-0.08PT [40]	87	7700	1455	−5.1	36.0	0.4	40
PZT-5A [41]	16.4	1700	171	−10.4	11.6	7.2	80
PZT-5H	15.9	3935	320	−16.6	19.4	7.9	75
PVDF [42, 43]	239	13	23.9	0.055 [49]	2.0	0.03	17.2
ZnO [44]	7.9	11	−5.2	−0.54	3.6	3.0	—

[a] Calculated values.
[b] Transverse 23 coefficients are given instead of 31 ones.

$$s_{IJ}^D = s_{IJ}^E - d_{kI}\beta_{kl}d_{lJ}; \tag{22}$$

where β_{kl} can be found from $\beta_{kl}\varepsilon_{ij} = 1$.

In the case of 4mm, 6mm and 3m point groups, the s_{33}^D and s_{11}^D coefficients can be calculated by

$$s_{33}^D = s_{33}^E - \frac{d_{33}^2}{\varepsilon_{33}^{\mathrm{T}}}, \tag{23}$$

$$s_{11}^D = s_{11}^E - \frac{d_{31}^2}{\varepsilon_{33}^{\mathrm{T}}} \text{ for 4mm \&6mm}, \tag{24}$$

$$\text{And } s_{11}^D = s_{11}^E - \frac{d_{31}^2}{\varepsilon_{33}^{\mathrm{T}}} - \frac{d_{21}^2}{\varepsilon_{22}^{\mathrm{T}}} \text{ for 3m point group.} \tag{25}$$

The $\mathrm{FoM}^{\mathrm{S}}$ values for transverse logitudinal modes of the frequently used lead-based and lead-free materials are summarized in table 6. The K_{iJ}^2, defined by equation (20), differs from $\mathrm{FoM}^{\mathrm{s}}$ (equation (21)) just by a reciprocal value of s_{JJ}^D. Moreover, the s_{JJ}^D coefficient presents close value to that of s_{JJ}^E coefficient, which is already taken into account in the K_{iJ}^2 expression. Therefore, K_{iJ}^2 and $\mathrm{FoM}_{iJ}^{\mathrm{S}}$ present similar orientation dependences (as an example, K_{iJ}^2 and $\mathrm{FoM}_{iJ}^{\mathrm{S}}$ of $BiFeO_3$ are compared in figure 10) and the materials with high electromechanical coupling factors also present a high $\mathrm{FoM}^{\mathrm{S}}$.

In the case of strain-driven harvesters operating in transverse mode, lead-free materials $BaTiO_3$, KTN, KNN-LT offer the same performance as lead-based PZT-5H and PMN-PT (table 6), while $KNbO_3$, $(10\bar{1}2)$ and $(10\bar{1}4)$ $BiFeO_3$ and 46°Y-cut $LiNbO_3$ overpass in terms of $\mathrm{FoM}_{31}^{\mathrm{S}}$ all these materials.

The longitudinal strain FoM of several lead-free materials ($BaTiO_3$, (011) $KNbO_3$ and $KTN_{0.53}$) goes beyond that of lead-based materials. The $\mathrm{FoM}_{31}^{\mathrm{S}}$ of $BaTiO_3$ reaches as high value as 387 kJ cm^{-3} (higher by a factor of four than that of PMN-PT). The $\mathrm{FoM}_{32}^{\mathrm{S}}$ values of 145°Y $LiNbO_3$ and $(10\bar{1}2)$ and $(10\bar{1}4)$ $BiFeO_3$ also approaches the highest FoM expected for the lead-based materials such as PMN-PT single-crystals. Polymers have decent FoMs and very low stiffness. These features are interesting for sensor applications or human body motion energy harvesting, where robustness and flexibility have priority over high coupling.

The inertial (vibrational or flexural) harvesters undergoing an acceleration under applied stress and the maximum generated power can be described for 31 operational mode as

$$P_{\max} = \frac{1}{4}\left(\frac{e_{31}^2}{\varepsilon_{33}^T}\right)\left(\frac{1-\nu_b}{Y_b}\right)\left(\frac{m}{\omega_0}\right)Q_{\mathrm{tot}}^2 a_0^2 \tag{26}$$

where Y_b is the Young modulus, ν_b -Poisson's ratio, m-mass, ω_0- resonance frequency, Q_{tot}- total electrical and mechanical quality factor, and a_0- excitation accelaration [45]. The Young modulus and Poisson's ration of the substrate can be used for the thin-film based transducers [45]. Their efficiency is highly dependent on the excitation frequency, acceleration, the natural frequency of the structure as well as the total quality factor. The mechanical part (Q_m) of the total quality factor depends on the piezoelectric material and substrate mechanical properties and the design of the heterostructure (thiknesses of different materials, tip mass, clamping, etc).

The mechanical quality factors of the commonly used piezoelectric single-crystal and ceramic materials are compared in the table 7. One can note very high Q_m factors of AlN, $BaTiO_3$ and $LiNbO_3$. However, much lower total Q values are attained in the piezoelectric energy transducers. For example, in the case of $LiNbO_3$/Si based tranducers, the quality factor of 396 was reported, which is highly overpassing the values of the

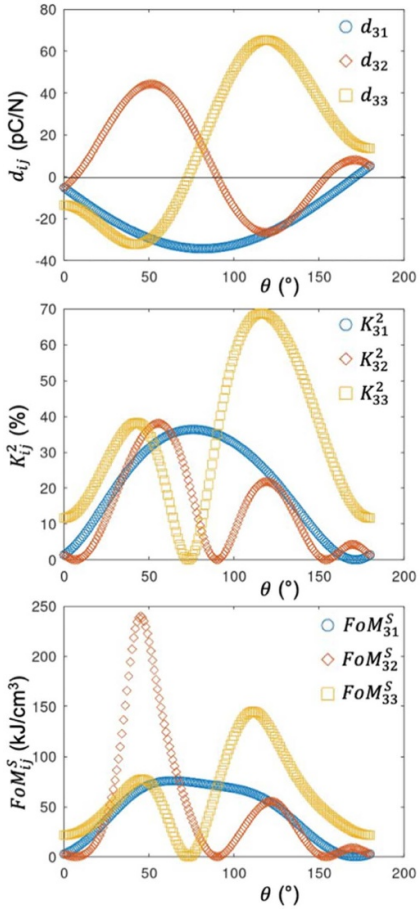

Figure 10. The piezoelectric coefficients d_{ij}, the electromechanical coupling factors $K^{2'}_{iJ}$, and strain figures of merit $\mathrm{FoM}^{\mathrm{S}}_{iJ}$ (with $i = 3$ and $J = 1$–3) of trigonal $BiFeO_3$ as a function angle Θ, rotated around the X-axis (a-axis of the hexagonal unit cell). The positive Z-axis (c-axis or spontaneous polarization axis) corresponds to $\Theta = 0^\circ$, while -Y-axis (perpendicular to $(\bar{1}010)$ family planes)—to $\Theta = 90^\circ$.

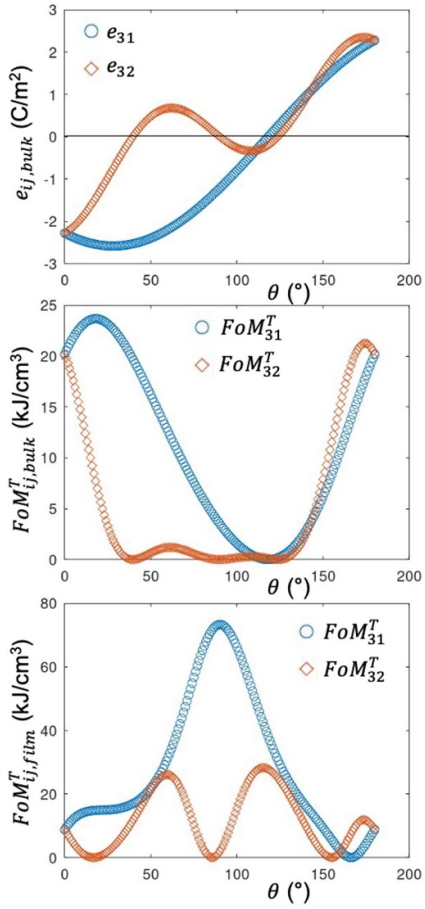

Figure 11. The piezoelectric coefficients e_{iJ} (bulk), and stress figures of merit $\mathrm{FoM}^{\mathrm{T}}_{iJ}$ (with $i = 3$ and $J = 1$–2) of single crystal(bulk) and clamped thin films of $BiFeO_3$ as a function angle Θ, rotated around the X-axis (a-axis of the hexagonal unit cell). The positive Z-axis (c-axis or spontaneous polarization axis) corresponds to $\Theta = 0^\circ$, while -Y-axis (perpendicular to $(\bar{1}010)$ family planes)—to $\Theta = 90^\circ$.

quality factors possible to attain by using lead-based materials [46]. The quality factor can be further increased if the transducer is placed in the vacuum conditions as demonstrated Q_{tot} of 810 for an AlN MEMS device [47]. Furthermore, the contribution of the piezoelectric material to the generated power by stress-driven harvester (equation (26)) can be described by an FoM for 31 transverse mode ($\mathrm{FoM}^{\mathrm{T}}_{31}$):

$$\mathrm{FoM}^{\mathrm{T}}_{31} = \frac{e^2_{31}}{\varepsilon^{\mathrm{T}}_{33}}. \tag{27}$$

The $\mathrm{FoM}^{\mathrm{T}}$ of different lead-based and lead-free piezoelectric materials, estimated from the piezoelectric and permittivity coefficients available in the literature, is given in comparison to $K^{2'}_{31}$ values in table 7. The lead-based PMN-PT and PZN-PT single crystals present the highest K^2_{31} values from studied materials thanks to extremely high d_{31} coefficients, but they show very low $\mathrm{FoM}^{\mathrm{T}}$ defined by e_{31} and extremely high permittivity. The e'_{31} and corresponding $\mathrm{FoM}^{\mathrm{T}}_{31}$ present similar orientation dependence as can be seen in the figure 11, while the big discrepancy can be seen in the angular dependences of $\mathrm{K}^{2'}$ and $\mathrm{FoM}^{\mathrm{T}}$ (figures 10 and 11, respectively). For example, the -Y-orientation of $BiFeO_3$ presents the $K^{2'}_{31}$ close to its maximum value (figure 10) and FoM^T_{31} close to its minimum value (figure 11). Very high $\mathrm{FoM}^{\mathrm{T}}$ can be obtained for Z-axis oriented $BiFeO_3$. This indicates that $\mathrm{FoM}^{\mathrm{T}}$ (equation (27)) is more relevant factor than material K^2 (equation (20)) for the comparison of the material performance in vibrational energy transducers, evaluated in terms of generated power (equation (26)). The FoM^T_{31} of AlN, ZnO, $KNbO_3$ and KNN-LT are slightly smaller than that of PZT ceramics, while $KTN_{0.53}$ show equivalent performance to PZT. The Z-axis oriented $LiNbO_3$ has quite low FoM^T_{31} (0.35), which is comparable to that of $BaTiO_3$ and lead-based single crystals. The $\mathrm{FoM}^{\mathrm{T}}_{23}$ higher by a factor of two with respect to that of PZT ceramics was obtained for the 137°Y oriented $LiNbO_3$. The highest FoM^T_{32} is expected for the $BiFeO_3$, but its piezoelectric constants were only estimated theoretically and the experimental measurements on this material are struggling due to very high leakage currents. The case of the $BiFeO_3$ is another

example of a disagreement between K^2 and FoM^T values: K^2 is very low but FoM^T is extremely high. According to equation (5), the e_{31} of bulk trigonal material (also valid for tetragonal and hexagonal ones) is

$$e_{31} = d_{3Q}c^E_{Q1} = d_{31}\left(c^E_{11} + c^E_{21}\right) + d_{33}c^E_{31}. \tag{28}$$

Therefore, the comparison of different materials in terms of their d_{31} for vibrational harvesting applications, frequently used in literature, is not necessarily correct, as e_{31} is a product of several piezoelectric and stiffness constants.

In the case of the vibrational energy harvesting, the bulk piezoelectric materials are rarely used as they are very stiff and it is difficult to get some energy at low acceleration levels. In most of the cases the composite structures consist of piezoelectric thick film (grown, bonded or glued) on nonpiezoelectric substrate offering flexibility. Therefore, the film is clamped and as indicated above the stiffness of the heterostructure is mainly defined by the elastic properties of the substrate. Therefore, in the case of the film/substrate composite structure, the electromechanical coupling of film/substrate composite structure, K^2_f, has to be described not by equation (20) but by the relationship including substrate properties has to be used [48]

$$K^2_f = 2\left(\frac{e^2_{31}}{\varepsilon^T_{33}}\right)_{\text{film}}\left(\frac{1-\nu_b}{Y_b}\right)_{\text{substrate}}. \tag{29}$$

This K^2_f definition (equation (29)) as well as FoM^T expressed by equation (27) are in line with the generated power expression given in equation (26). In the case of the clamped films, the piezoelectric and dielectric coefficients also are not equal to those of bulk materials. According to Muralt's definition [48], the $e_{31,f}$, $d_{33,f}$, and $\varepsilon_{33,f}$ of the (001) oriented piezoelectric film with isotropic properties in the substrate plane (valid for the trigonal, hexagonal and tetragonal symmetries) and $T_3 = 0$ can be derived from constitutive equations:

$$S_1 = s^E_{11}T_1 + s^E_{12}T_2 + d_{31}E_3, \tag{30}$$

$$S_2 = s^E_{11}T_2 + s^E_{12}T_1 + d_{31}E_3, \tag{31}$$

$$S_3 = s^E_{13}(T_1 + T_2) + d_{33}E_3, \tag{32}$$

$$D_3 = d_{31}(T_1 + T_2) + \varepsilon^T_{33}E_3. \tag{33}$$

Considering $S_1 = S_2 = 0$ and $T_1 = T_2$, the $e_{31,f}$, $d_{33,f}$, and $\varepsilon_{33,f}$ are described by

$$e_{31,f} = \frac{d_{31}}{s^E_{11} + s^E_{12}} = e_{31} - \frac{c^E_{13}}{c^E_{33}}e_{33}, \tag{34}$$

$$d_{33,f} = \frac{e_{33}}{c^E_{33}} = d_{33} - \frac{2s^E_{13}}{s^E_{11} + s^E_{12}}d_{31}, \tag{35}$$

$$\varepsilon^T_{33,f} = \varepsilon^T_{33} - \frac{2d^2_{31}}{s^E_{11} + s^E_{12}}, \text{ respectively.} \tag{36}$$

In the case of the films with anisotropic properties in the substrate plane, such as orthorhombic $KNbO_3$ or other growth orientations than c-axis one of tetragonal, hexagonal or trigonal films, the $d_{31} \neq d_{32}$, $s^E_{11} \neq s^E_{22}$, $s^E_{13} \neq s^E_{23}$ and $T_1 \neq T_2$, while s^E_{12} and s^E_{13} remain equal to s^E_{21} and s^E_{31}, respectively, even after the tensor transformation due to symmetric nature of the elasticity tensor. The corresponding constitutive eaquations will be

$$S_1 = s^E_{11}T_1 + s^E_{12}T_2 + d_{31}E_3, \tag{37}$$

$$S_2 = s^E_{22}T_2 + s^E_{12}T_1 + d_{32}E_3, \tag{38}$$

$$S_3 = s^E_{13}T_1 + s^E_{23}T_2 + d_{33}E_3, \tag{39}$$

$$D_3 = d_{31}T_1 + d_{32}T_2 + \varepsilon^T_{33}E_3. \tag{40}$$

Again, assuming that $S_1 = S_2 = 0$, the anisotropic thin film coefficients with anisotropic properties in the substrate plane 12 can be be obtained

$$e_{31,f} = \frac{s^E_{22}d_{31} - s^E_{12}d_{32}}{s^E_{11}s^E_{22} - \left(s^E_{12}\right)^2}, \tag{41}$$

$$e_{32,f} = \frac{s^E_{11}d_{32} - s^E_{12}d_{31}}{s^E_{11}s^E_{22} - \left(s^E_{12}\right)^2}, \tag{42}$$

$$d_{33,f} = d_{33} + \frac{s^E_{13}\left(s^E_{12}d_{32} - s^E_{22}d_{31}\right) + s^E_{23}\left(s^E_{12}d_{31} - s^E_{11}d_{32}\right)}{s^E_{11}s^E_{22} - \left(s^E_{12}\right)^2}, \tag{43}$$

$$\varepsilon^T_{33,f} = \varepsilon^T_{33} - \frac{s^E_{22}d^2_{31} - 2s^E_{12}d_{31}d_{32} + s^E_{11}d^2_{32}}{s^E_{11}s^E_{22} - \left(s^E_{12}\right)^2}. \tag{44}$$

The piezoelectric and permittivity coefficients (estimated by using equations (34)–(36)) of (001) oriented $BiFeO_3$, $LiNbO_3$, $LiTaO_3$, AlN, ZnO, PZT, KTN_{53}, and $BaTiO_3$ thin films are compared to those of bulk materials in the tables 8 and 9. The high-symmetry rotational axis along c-axis of tetragonal and hexagonal materials (4mm and 6mm point groups), makes that the piezoelectric, dielectric and elastic properties are little dependent on the orientation in the ab-plane. In the case of c-axis oriented thin films with 3m point group ($LiNbO_3$, $BiFeO_3$, and $LiTaO_3$), the presence of four growth domains (rotated by 90° in the substrate plane) or the absence of the defined orientation in the ab-plane (textured films) would cancel d_{22} (e_{22}) and s_{14} (c_{14}) coefficients and the coefficients related to them by symmetry (as an example for d and e see equation (16), resulting in tensor definitions like in the 6mm and 4mm point groups (table 1). Finally, no change is induced to the coefficients $e_{31,f}$, $d_{33,f}$, $\varepsilon^T_{33,f}$(equations (41)–(44)) by the disorder in the ab plane of tetragonal, hexagonal and trigonal c-axis oriented films. As shown above, it is not the case in the orthorhombic materials and other growth orientations than c-axis one of trigonal, hexagonal and tetragonal materials. Therefore, the e_{32} and FoM^T_{32} and the effect of the orientation disorder in the substrate plane were estimated in these cases, as well (table 9).

The level of the change of the thin film coefficients with respect to those of the bulk materials is highly material dependent and it varies from less than 1% up to more than 50% (tables 8 and 9). As expected [48], the $d_{33,f}$ of films is smaller than that of the bulk materials with exception to (0001) $BiFeO_3$, in which it is slightly increased with respect to the bulk value. The $\varepsilon^{T}_{33,f}$ is also smaller than that of the bulk materials. The FoM^{S}_{33} of thin films tends to decrease in comparison to that of the bulk materials, as well (table 8). For example, for the PZT it would change from 40.6 kJ cm^{-3} to the 12.1 kJ cm^{-3} (calculated using coefficient set given in table 8). The FoM^{S}_{33} of lead-free (001) oriented $BaTiO_3$, KNT_{53}, and $KNbO_3$ thin films are 53.3 kJ cm^{-3}, 46.7 kJ cm^{-3}, and 47.9 kJ $cm^{-3,}$ respectively. Although, these values were significantly reduced with respect to the bulk values (table 6), they remain competitive even with the bulk PZT ceramics. The thin films of ZnO and AlN with $FoM^{S}_{33} = 20.5$ kJ cm^{-3} are also overpassing of FoM^{S}_{33} of PZT films. High FoM^{S}_{33} can be also obtained in epitaxial or textured $(10\bar{1}2)$ and $(10\bar{1}4)$ BFO and $LiNbO_3$ films. The highest FoM^{S}_{33} with value of 67 kJ cm^{-3} can be attained in (011) oriented $KNbO_3$ films and this value is very little dependent on the film in plane orientation. (101) orientation of $KNbO_3$ presents very high permittivity (figure 1, table 8) and this reduces drastically its FoM^{S}_{33}.

The $e'_{31,f}$ coefficients and FOM^{T} of piezoelectric thin films are compared to those of bulk materials in the table 9. The absolute value of $e'_{31,f}$ of tetragonal and hexagonal films is increased with respect to the bulk value. The increase of $e_{31,f}$ due to the film clamping is observed also in the (001) textured films (or containing four in-plane rotated growth domains), independently of their symmetry and growth orientation, which present highly isotropic symmetry of the plane parallel to the substrate plane (point group ∞m) as in the of hexagonal and tetragonal symmetry (point groups 4mm and 6mm). In the case of these materials, the FOM^{T} of thin films is higher than that of bulk materials due to the increased $e_{31,f}$ and reduced $\varepsilon^{T}_{33,f}$ [48]. In single crystalline films with more anisotropic symmetries than 4mm/6mm/∞m such as trigonal 3m and orthorhombic mm2 point groups, the effect of the film clamping on the $e_{31,f}$ coefficient can be positive or negative ant it depends on the material and its orientation. The change FoM^{T}_{31} and FoM^{T}_{32} of thin films and bulk $BiFeO_3$ as a function of the out-of-plane orientation (3) in the *YZ* plane is illustrated in the figure 11. The FoM^{T} anisotropy in *YZ* plane of $BiFeO_3$ films is completely different from that of the bulk $BiFeO_3$ (see figure 11). For example, the maximum FoM^{T} in the transverse 31 mode for the Y-oriented films and this value is at least twice bigger than the maximum $FoM^{T}_{32,f}$, while in the bulk $BiFeO_3$, the maximum FoM^{T}_{31} is at $\Theta = 45°$ and its value is close to the maximum FoM^{T}_{32}. The maximum values of FoM^{T}_{31} and $FoM^{T}_{32}$are not observed at the same angles in both cases however, they have very close values at $\Theta = 130°$, indicating that proximity $(10\bar{1}2)$ planes ($\Theta = 125°$) are relatively isotropic in terms of transverse excitation in the substrate plane.

One can also note highly anisotropic in-plane nature (a difference in e_{31} and e_{32} values) of the orthorhombic $KNbO_3$, while trigonal $(10\bar{1}2)$ oriented $LiNbO_3$/$LiTaO_3$ & $BiFeO3$ films and single crystal properties are more isotropic in terms of FoM^{T} in the substrate plane (table 9). However, this is valid just around this $(10\bar{1}2)$ orientation, as can be seen in figure 11. However, the absence of the in-plane orientation reduces drastically the transverse FoM^{T} of the other textured orientations than $(10\bar{1}2)$ and (0001) $BiFeO_3$ films due to opposite signs of the e_{31} and e_{32} coefficients. The disorder of the film orientation in the substrate plane (directions 1 and 2), will average the related piezoelectric and elastic coefficients (equations (41) and (42)) resulting in the averaged $e_{31,f}$ and FOM^{T} values with respect to the maximum ones of the single-crystalline films.

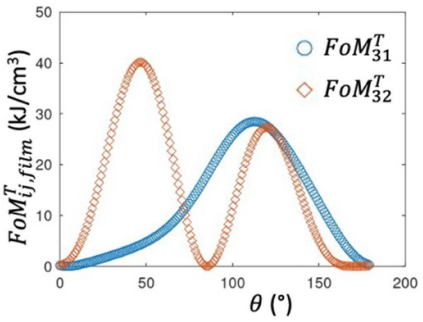

Figure 12. The stress figures of merit FoM^{T}_{iJ} (with $i = 3$ and $J = 1$–2) of clamped $LiNbO_3$ thin films as a function angle Θ, rotated around the *X*-axis (*a*-axis of the hexagonal unit cell). The positive *Z*-axis (*c*-axis or spontaneous polarization axis) corresponds to $\Theta = 0\,°$, while -*Y*-axis (perpendicular to $(\bar{1}010)$family planes)—to $\Theta = 90°$.

Several times higher transverse FoM^{T} can be obtained in the case of piezoelectric thin films with respect to that of the bulk materials (tables 7 and 9). In the case of the single crystals, the highest values were predicted for the 137°Y-$LiNbO_3$ and (0001) $BiFeO_3$ (FoM^{T}_{32} of 15.5 kJ cm^{-3} and 20.2 kJ cm^{-3}, respectively). Y-oriented single-crystalline $BiFeO_3$ films would offer the FoM^{T} in 31 trasnverse mode of 73 kJ cm^{-3} and $(10\bar{1}2)$ oriented films—26.4 kJ cm^{-3}. Although, the $LiNbO_3$ belongs to the same point group as $BiFeO_3$, its transverse 32 mode shows similar performance to that the 31 one and the $(10\bar{1}2)$ oriented single-crystalline or textured films are most promising in terms of FoM^{T} (26.6 kJ m^{-3}). Fortunately, the textured growth or 90° in-plane growth domains does not reduce these values and the performance of such $BiFeO_3$ and $LiNbO_3$ films is expected to be better by a factor of 2 than that of the textured (0001) ZnO or AlN films and close to that of textured PZT films. In order to avoid the reduction of the performance due to in-plane orientation disorder, we need to look for the out-of-plane orientations presenting highly isotropic in-plane properties such as high e_{31} and e_{32} coefficients with close absolute values. In the case of $LiNbO_3$ thin films, at around $\Theta = 125°$ (corresponds to $(10\bar{1}2)$ orientation) FoM^{T}_{31} and FoM^{T}_{32} values are the same (figure 12) and the $e_{31,f}$ and $e_{32,f}$ are almost equal (table 9). This makes, that the $(10\bar{1}2)$ orientation of $LiNbO_3$ offers FoM^{T} of around 26.6 kJ cm^{-3} independently of its in-plane orientation.

Table 8. Comparison of the FoM^S_{33} for strain driven energy harvesters in 33 operational mode, d'_{33}, and ε'_{33} coefficients of frequently studied piezoelectric bulk materials and thin films with trigonal, hexagonal (H), tetragonal (tetr), and orthorhombic (ortho) symmetry. The coefficients of the textured films (not presenting ordered orientation in the substrate plane) or epitaxial films with four growth domains, rotated around growth axis by 90° in the substrate plane were estimated (indicated by subscript 'text'). The s'^E_{33} and s'^D_{33} are given, as well.

		d'_{33}	d'_{33},f	s'^E_{33}	s'^D_{33}			$FoM^S_{33\ bulk}$	$FoM^S_{33,f}$
	Material and its orientation 3	pC N^{-1}		pm^2 N^{-1}		$\varepsilon'^T_{33}/\varepsilon_0$	$\varepsilon'^T_{33,f}/\varepsilon_0$	kJ cm^{-3}	
Trigonal	(0001) $BiFeO_3$	−16	−18.3	6.1	5.1	29.1	28.3	31.9	42.9
	(10$\bar{1}$2) $BiFeO_3$	64.4	29.2	16.7	5.6	42.1	27.2	120	37.8
	(10$\bar{1}$2) $BiFeO_{3text}$	64.4	29.3	16.7	5.6	42.1	27.2	120	38.0
	(10$\bar{1}$4) $BiFeO_3$	−30.5	−18.8	8.6	5.6	35.0	25.2	62.8	33.8
	(10$\bar{1}$4) $BiFeO_{3text}$	−30.5	−25.4	8.6	5.6	35.0	33.8	62.8	44.9
	(0001) $LiNbO_3$	8.3	5.4	5.1	5.0	28.9	28.8	11	4.5
	(10$\bar{1}$2) $LiNbO_3$	−39.1	−25.1	6.9	4.4	69.5	54.8	80.7	42.1
	(10$\bar{1}$2) $LiNbO_{3\ text}$	−39.1	−5.3	6.9	4.4	69.5	55.3	80.7	42.5
	(0001) $LiTaO_3$	8.2	6.2	4.3	3.0	44.1	43.6	8.8	5.1
	(10$\bar{1}$2) $LiTaO_3$	−15.0	−12.1	4.1	3.5	42.9	39.4	41.0	29.0
	(10$\bar{1}$2) $LiTaO_{3text}$	−15.0	−12.0	4.1	3.5	42.9	39.5	41.0	28.4
H	(0001) AlN	5	3.9	3.2	2.9	9.5	9.1	32.0	20.5
	(0001) ZnO	12.4	7.9	6.8	5.2	11	9.8	44.5	20.5
Tetr	(001)PZTcr or text[a]	289	130	18.8	9.5	1300	883	40.6	**12.1**
	(001)KTN_{53}	132	78.5	9.5	5.0	435	314.2	95.8	**46.7**
	(001)KNN-LT	354	65.5	27	9.1	790	293	73.0	6.7
	(001) $BaTiO_3$	85.6	27.9	6.8	1.9	168	128	387.2	**53.3**
Ortho	(001) $KNbO_3$	29.3	22.4	7.0	4.8	44	35.2	65.7	**47.9**
	(001) $KNbO_{3\ text}$	29.3	24.9	7.0	4.8	44	42.6	65.7	**49.0**
	(101) $KNbO_3$	59.6	43.3	5.3	4.5	498	440.5	33.4	19.9
	(101) $KNbO_{3\ text}$	59.6	44.2	5.3	4.5	498	470.2	33.4	19.4
	(011) $KNbO_3$	86.3	38.4	12.5	3.7	95.2	53.9	190.8	**66.6**
	(011) $KNbO_{3\ text}$	86.3	38.6	12.5	3.7	95.2	54.1	190.8	**67.1**

[a] cr stands for ceramics, PZTcr and (001) textured PZT films belong to ∞m point group with tensor definitions equivalent to 4mm point group.

The highest FoM^T_f of the thin films is expected for the $KNbO_3$ based materials reaching 58 kJ cm^{-3} for the single crystalline (011) $KNbO_3$ with stress applied along *Y*-axis and the single crystalline or textured KTN_{53}. In the case of the textured (011) $KNbO_3$ this value is slightly reduced (54 kJ m^{-3}). High $FoM^T_{32,f}$ (41 kJ cm^{-3}) is also predicted for the single crystalline (001) $KNbO_3$ films but FoM^T_f is low for the (001) textured films. These values are considerably higher that the calculated one for the textured PZT films (28.8 kJ cm^{-3}).

3. Piezoelectric materials for energy harvesting

In the previous section the perfomance of the piezoelectric thin films was estimated theoretically from the physical constants of the bulk materials (mainly single crystals) in terms of the FoM of strain- and stress-driven piezoelectric energy transducers. In this section, we will overview the experimentally measured piezoelectric thin film properties, summarized in the table 10, of the potential lead-free materials for the piezoelectric EH applications as demonstrated in the tables 8 and 9. The piezoelectric coefficients of thin films measured by piezoelectric force microscopy were not considered due to their unreliability. Moreover, the bonded/glued thick films on Si or metal substrates can be also fabricated from the ceramics or single crystals by ion-slicing or polishing techniques. Bonding/polishing techniques become in particular interesting when the piezoelectric films with the thicknesses of tens of microns are needed. Therefore, the availability of high-quality bulk materials is discussed, as well.

3.1. $BaTiO_3$

$BaTiO_3$ ceramics is one of the very first piezoelectric material to find its way in industrial applications of capacitors due to its very high dielectric constant and piezoelectric transducers, in which it was lately replaced by PZT ceramics [50, 51]. Single crystal $BaTiO_3$ substrates (electrically poled, but containing a/c domains) with several orientations ((100), (110), (001) and (111)) are commercially available but with very limited dimensions of 10 mm × 10 mm × 1 mm [52–54]. The single crystalline films were produced by ion slicing technique from $BaTiO_3$ single crystals [55]. However, the high price and small dimensions of available single crystals limit the practical applications of the $BaTiO_3$ single crystals. Therefore, $BaTiO_3$ thin films with highly controlled orientation and properties open new perspectives for the $BaTiO_3$ applications. At present, $BaTiO_3$ thin films are highly studied for electronics field effect transistors (FETs) and integrated photonics due to its extremely high electro-optical coefficient [56]. This material has tetragonal Perovskite structure at RT (point

Table 9. Comparison of the FoM^T for stress driven energy harvesters in 31/32 operational mode, e'_{31}, and ε'_{33} coefficients of frequently studied piezoelectric bulk materials and thin films with trigonal, hexagonal (H), tetragonal (tetra), and orthorhombic symmetry. In the case of anisotropy in the substrate plane, the e_{32} coefficient and the related FoM^T_{32} are indicated. The coefficients of the textured films (not presenting ordered orientation in the substrate plane) or epitaxial films with four growth domains, rotated around growth axis by 90° were estimated, (indicated by subscript 'text').

		e'_{31} (e'_{32})	$e'_{31,f}$ ($e'_{32,f}$)			FoM^T (bulk) 31 (32)	FoM^T_f 31 (32)
	Material and its orientation 3	C m^{-2}		$\varepsilon'^T_{33}/\varepsilon_0$	$\varepsilon'^T_{33,f}/\varepsilon_0$	kJ cm^{-3}	
Trigonal	(001) $BiFeO_3$	−2.3	−0.95	29.1	28.3	20.2	3.6
	$(10\bar{1}2)$ $BiFeO_3$	0.3	2.7	42.1	27.2	0.2	**30.4**
		(00)	(2.4)			(0)	**(24.9)**
	$(10\bar{1}2)$ $BiFeO_{3\ text}$	0.15	2.6	42.1	27.2	0.1	27.5
	$(10\bar{1}4)$ $BiFeO_3$	−2.6	1.9	35.0	25.2	21.1	15.8
		(−0.3)	(−1.3)			(0.4)	(7.1)
	$(10\bar{1}4)$ $BiFeO_{3\ text}$	−1.45	−1.1	35.0	33.8	7.0	3.5
	(0001) $LiNbO_3$	0.3	−0.22	28.9	28.8	0.35	0.2
	$\left(10\bar{1}2\right)$ $LiNbO_3$	1.49	3.53	67.7	53.5	3.7	**26.4**
		(1.86)	(3.57)			(5.8)	**(26.9)**
	$\left(10\bar{1}2\right)$ $LiNbO_{3\ text}$	1.68	3.55	67.7	53.5	5.8	**26.6**
	(0001) $LiTaO_3$	−0.22	−0.71	44.1	43.6	0.12	1.3
	$(10\bar{1}2)$ $LiTaO_3$	1.7	−2.36	42.9	39.4	7.6	16.0
		(0.96)	(−1.91)			(2.4)	(10.4)
	$(10\bar{1}2)$ $LiTaO_{3\ text}$	1.21	−2.15	42.9	39.5	4.2	13.2
H	(0001) AlN	−0.6	−0.9	9.5	9.1	4.0	10.3
	(0001) ZnO	−0.5	−1.1	11	9.8	3.0	13.1
Tetra	(001)PZTcr or text[a]	−5.2	−15.0	1300	883	2.4	**28.8**
	(001)KTN_{53}	−5.2	−12.7	435	314.2	7.0	**58.3**
	(001)KNN-LT	−6.28	−13.5	790	293	5.6	**70**
	(001) $BaTiO_3$	0.7	−5.2	168	128	0.3	**23.4**
Orthorhombic	(001) $KNbO_3$	2.5	0.8	44	35.2	16	2.2
		(−1.1)	(−3.6)			(3.2)	**(41.2)**
	(001) $KNbO_{3\ text}$	0.68	−1.3	44	42.6	1.2	4.4
	(101) $KNbO_3$	1.8	−1.2	498	440.5	0.7	0.3
		(−7.0)	(−10.1)			(11.1)	**(26.0)**
	(101) $KNbO_{3\ text}$	−2.6	−5.5	498	470.2	1.5	7.4
	(011) $KNbO_3$	−0.8	−4.6	95.2	53.9	0.8	**43.6**
		(−1.14)	(−5.3)			(1.5)	**(58.3)**
	(011) $KNbO_{3\ text}$	−0.97	−5.1	95.2	54.1	1.2	**54.4**

[a] cr stands for ceramics, PZTcr and (001) textured PZT films belong to ∞m point group with tensor definitions equivalent to 4mm point group (table 4).

group 4mm). It is a ferroelectric material with the Curie temperature (T_C) of 120 °C. In general, $BaTiO_3$ properties are in large part dependent on the proximity of the phase transitions, composition and dopants concentration, while the properties of the thin films are additionally affected by the presence of the strain. In the case of the epitaxial $BaTiO_3$ thin films, the strain highly affects the Curie temperature and it was demonstrated that $T_C > 600$ °C and a significant increase of remanent polarization can be reached in the films under compressive biaxial stress [57]. Tuning of the film local dielectric constant can be directly achieved by modifying the Ba/Ti cation ratio and the strain state. Local variation of the dielectric function in a film is associated with the vicinity of the phase boundary between the out-of-plane and in-plane orientations of the tetragonal $BaTiO_3$ films. The strain in the film is dependent not only on the substrate used for the epitaxy, but also on the deposition conditions such as deposition temperature or the partial oxygen pressure used during film deposition [58]. Ti/Ba ratio is not only influences the film crystallographic structure but it has an effect on its physical properties, as well [59]. $BaTiO_3$ electric properties are strongly influenced by the oxygen vacancy concentration. A better control of the oxygen flow during a process can help to reduce leakage current and so maintain a constant dielectric constant [60].

The A/B site doping or co-doping is a very convenient method to modify the properties of $BaTiO_3$ by a substitution of the A-site with the rare-earth elements and the B-site with transition metals. For example, in the case of the B-site, Fe was found to significantly enhance the ferroelectric properties of the $BaTiO_3$ thin film [61]. Moreover, the band gap is also strongly affected by the doping amount of Fe and by the oxygen vacancies [62]. In a similar way, the Ti substitution by Mn has an impact on material symmetry with a change from tetragonal to cubic one and it helps to reduce leakage current [60]. The A-site doping by Ce and Eu was reported [63]. The impact of the cerium doping on film capacitance and dielectric

loss was investigated, but as before for a high doping concentration the change of symmetry from a ferroelectric phase to a paraelectric phase was observed.

To improve the functional properties, $BaTiO_3$ was combined with other materials, as well. The most used one for this purpose was $BiFeO_3$ which has been incorporated with pure or doped $BaTiO_3$. This combination of the materials has an impact on the structure, ferroelectric properties, piezoelectric properties and the Curie temperature. For example, the $(1-x)BiFeO_3-xBaTiO_3-Bi(Zn_{0.5}Ti_{0.5})O_3$ ceramics shows good piezoelectric performance even at high temperatures (550 °C) [64]. High dielectric constants have also been measured creating new perspectives for the fast charging-discharging applications and the energy-storage capacitor applications [65]. In less conventional way, $BaTiO_3$ films have been modified by octadecyl phosphonic acid and/or phosphonic acid to induce a significant band edge offset on the surface [66]. $BaTiO_3$ ceramics was recently used in the layered structures with high porosity in order to increase the performance of the strain-driven EH performance in thickness mode 33 [67]. In the structures with layered porosity the d'_{33} coefficient remains similar to that of the dense $BaTiO_3$ while the permittivity is highly reduced by the presence of the pores. This approach is not compatible with the stress-driven harvesters, as d_{31} coefficient is highly reduced due to the porosity.

As demonstrated in the section 2, (001) textured or epitaxial $BaTiO_3$ thin films are in particular interesting for both strain- and stress-driven energy harvesters. The (100) orientation of $BaTiO_3$ presents the stress and strain FoMs by several orders smaller than those of the (001) orientation due to extremely high permittivity along a-axis ($\frac{\varepsilon^T_{11}}{\varepsilon_0} = 3600$). $BaTiO_3$ thin film growth by different physical and chemical methods (metal-organic chemical vapor deposition (MOCVD) [68, 69], pulsed laser deposition (PLD) [56, 58, 70] magnetron sputtering [56, 71], molecular bean epitaxy (MBE) [56], atomic layer deposition (ALD) [72, 73], sol-gel [74], activated reactive evaporation [75], aqueous chemical solution deposition [76], etc) was reported in the literature. The structural quality of the films grown by ALD was very low as the films consisted of a mixture of polycrystalline and amorphous parts [73]. At RT, the tetragonality of $BaTiO_3$ is very low (a/c ration is 1.01), therefore the film orientation is highly dependent on the state of the strain induced by a substrate. It is known that the compressive strain favors the growth of c-axis oriented $BaTiO_3$ films [57]. High-quality epitaxial (001) $BaTiO_3$ films have been grown on single crystalline substrates ((100) $SrTiO_3$, (110) $DyScO_3$, (110) $GdScO_3$, Pt(001), etc) [56, 59, 70] while the a-axis oriented $BaTiO_3$ has been obtained on epitaxial (100) Pt on MgO [74] and (100) single crystalline Pt [59]. There is also a possibility to grow (110) orientation on (110) $SrTiO_3$ and (110) single crystalline Pt [75]. However, as indicated above the (100) and (110) orientations do not present a particular interest for the EH applications due to their extremely high out-of-plane permittivity. The characterization of piezoelectric properties of $BaTiO_3$ films were rarely reported. In the case of the c-axis oriented $BaTiO_3$ films, the conducting $SrTiO_3$:Nb substrate was used for the piezoelectric properties characterization (table 10) [77]. The reported d_{33} value as expected for the thin films was lower (50 pC N^{-1}) than the bulk one (85.6 pC N^{-1}), but higher than the coefficient estimated for the thin film (27.9 pC N^{-1}) using equation (35) (table 10).

The single-crystal substrates used for the epitaxial $BaTiO_3$ are not viable in terms of size and price for the real EH applications. The films grown on the (111) textured Pt on SiO_2/Si or Si based substrates, compatible with piezoelectric transduction applications, presented polycrystalline microstructure independently on the deposition method used [73, 76, 78, 79] Such polycrystalline films were poled and transferred on the plastic substrates by wet etching of the Si substrate for the EH applications (the ability to generate the PD of 7 mW cm^{-3} was reported) [80]. The textured $LaNiO_3$ buffer layer was introduced to ameliorate the orientational quality of the films and highly a-axis oriented films were obtained [81].

A considerable effort was done to ameliorate $BaTiO_3$ thin film structural properties on Si substrates by implementing a template based on epitaxial $SrTiO_3$ thin films on Si grown by MBE [56, 71, 94]. This template allows to grow epitaxially c-axis oriented $BaTiO_3$ thin films. However, the strain relaxation occurs with the increase of the film thickness and c/a/c/a domain structure forms [56]. The electro-optic and ferroelectric properties were studied of $BaTiO_3/SrTiO_3$/Si films, but so far little is known about their piezoelectric properties. More recently, a (001)TiN/Si(100) template was used for the epitaxial $BaTiO_3$ film with in-plane and out-of-plane c-axis orientation growth by means of PLD. However, the c-axis films were highly defective [95].

3.2. ZnO and AlN

Non-ferroelectric piezoelectric materials such as ZnO and AlN and their derivatives have much lower K^2_{31} and K^2_{33} factors than PZT, but in the form of the thin films AlN and ZnO offer higher $FoM^S_{33,f}$ than PZT films although $FoM^T_{31,f}$ remains lower than that of PZT (tables 8 and 9). The main advantage of the AlN and ZnO films is their fabrication maturity and compatibility with conventional integrated circuit technology fabrication processes (Complementary Metal Oxide Semiconductor—CMOS). They present hexagonal symmetry and wurtzite structure (point group 6mm) giving as a result similar configuration of the piezoelectric tensor as in PZT ceramics and independence of the (0001) oriented film properties on the in-plane orientation. Moreover, (0001) orientation of AlN and ZnO corresponds to the dense planes and the fast-growing direction. Therefore, (0001) textured films can be obtained on many different substrates. (0001) textured ZnO and AlN films are usually sputtered on several types of substrates including bottom electrode/Si structures, and used especially for shear and bulk acoustic resonators. The piezoelectric properties of these films are well documented in the literature, as well (table 10). The $FoM^T_{31,f}$ of (0001) textured AlN on Pt/Si substrate is in a good agreement with the theoretical value [86]. In the case of epitaxial (0001) AlN films

Table 10. Comparison of the FOM^T for stress driven energy harvesters in 31 operational mode, $e'_{iJ,f}$, $d'_{iJ,f}$ and $\varepsilon'_{33,f}$ coefficients expected theoretically and measured experimentally for piezoelectric thin films. The calculated values are indicated by 'calc.' and bold font). Note that there is no difference in the calculated values for textured and epitaxial films of (001) oriented tetragonal materials such as KNN and $BaTiO_3$. (001) tetragonal orientation corresponds (001) orientation in pseudo-cubic system, as well.

Material	e_{31} (d_{31})	e_{33} (d_{33})	e_{15} (d_{15})	$\varepsilon^T_{33,f}/\varepsilon_0$ (freq.)	$FoM^T_{31,f}$
	C m^{-2} (pC N^{-1})				kJ cm^{-3}
(0001)$BiFeO_3$/(111) $SrRuO_3$/(111)$SrTiO_3$					
Film calc.	**−1.0**	**(−18.3)**		**28.3**	**3.6**
Film [82]	−1.3			58	2.9
(10$\bar{1}$2) $BiFeO_3$					
Film calc.	**2.6**	**(29.3)**		**27.2**	**27.5**
SRO/STO [82] (4 growth domains)	−3,5			122 (10 kHz)	10.0
Nb-STO [83] (4 growth domains)	−4,3				
LNO/SiO_2/Si (textured)	−4,3 [84] −3,6 [85]				
(0001)AlN, AlScN on Pt/Si based substrates (textured)					
AlN film calc.	**−0.9**	**(3.9)**		**9.1**	**10.3**
AlN [86]	−1.0	(3.4)		10.4 (10 kHz)	9.6
$Al_{0.86}Sc_{0.14}N$ [87]	−0.5	1.9	−0.26	13.3	1.9
$Al_{0.68}Sc_{0.32}N$ [87]	−0.7	2.8	−0.23	21.9	2.2
Epitaxial (0001)AlN and ZnO on C-sapphire					
AlN [88]	(−2.7)	(5.5)	(−4.1)	12	
ZnO [89]	−0.5	1.2	−0.5	8.5	2.9
ZnO film calc.	**−1.1**	**(7.9)**		**9.8**	**13.1**
$[001]_{pc}$ epitaxial $K_{1-x}Na_xNbO_3$ (KNN) on (001)Pt/(001)MgO					
X = 0.5 KNN ceramics	**(51)**	**(148)**		**496**	
X = 0.5 0.67KNN-0.33LT film calc.	**−13.5**	**(65.5)**		**293**	**70**
$x = 1$ $SrRuO_3$ buffer [90]	−0.9			270	0.3
$x = 0.84$ $+(110)_{pc}$ SRO buffer [90]	−2.4			320	1.8
$X = 0.38$ [91]	−3.6			185	7.0
$[001]_{pc}$ textured KNN, on (111)Pt/Ti/SiO_2/(100)Si					
$X = 0.44$ [9090]	−5.5			598	5.1
$x = 0.55$ polycr [92].	−14.4 (138)			∼1100	18.9
$+ (110)_{pc}$[93]	(210)			832–892	
Epitaxial (001)$BaTiO_3$/(100)$SrTiO_3$:Nb					
Film		(50) [77]			
Film calc.	**−5.2**	**(27.9)**		**128**	**23.4**

on C-sapphire, slightly increased values of the coefficients d_{31} and d_{33} were measured [88] (table 10) with respect to those of the bulk AlN (table 6), although the reduced $d_{33,f}$ was expected for the thin film. The measured piezoelectric properties of epitaxial ZnO on C-sapphire are much lower than those expected theoretically [89] (table 10).

Regarding energy harvesting, in [96], ZnO films were implemented in piezoelectric MEMS vibration energy harvesters with two piezoelectric elements for higher output performance (figure 13), where the energy harvester was fabricated on a Si wafer by means of standard micro-machining techniques. The resonance frequency was 1300.1 Hz, achieving 1.25 μW for 1 g acceleration level.

The results are very promising for AlN film integration in vibrational energy harvesting. One of the first successful implementations of the material was by Marzencki *et al* [97] where AlN was sputtered on a Si beam, achieving 0.8 μW at 1495 Hz for 2 g acceleration level (figure 14(a)). Similar results were observed by Elfrink *et al* [98] where in vacuum conditions an AlN MEMS device was capable to harvest 32 μW at 1 g having a quality factor of 810 [47]. More recently Jia and Seshia [99] obtained a peak this material, power output of 20.5 μW at 0.28 g (@210 Hz) for an AlN-on-SOI cantilever with 70% of its beam dedicated to housing a silicon and mass. Alamin Dow *et al* [100] achieved 10 μW at 0.75 g, further reducing the resonance frequency of the cantilever (186 Hz).

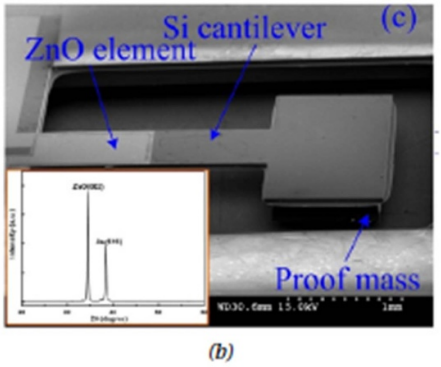

Figure 13. SEM image of ZnO/Si piezoelectric cantilever (the diffractogram indicates the (0001) orientation of ZnO film on (111) Pt layer in the inset). Reprinted from [96], with the permission of AIP Publishing.

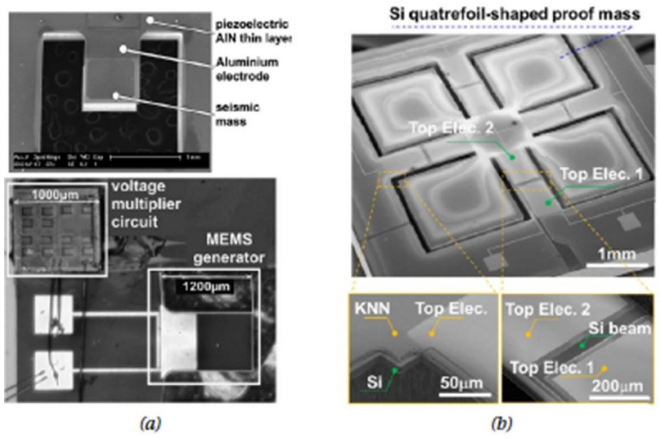

Figure 14. Pb-free energy harvesters: (a) AlN based silicon cantilever; Reprinted from [97], Copyright (2008), with permission from Elsevier. (b) nonlinear KNN quad-cantilever harvester. © 2014 IEEE. Reprinted, with permission, from [129].

Andosca *et al* [101] proposed an AlN MEMS device capable of working at 58 Hz, which generated 63 μW at 0.7 g. One of the highest power densities (2.5 mW cm^{-3} g^{-2}) at resonant frequency of 149 Hz were attained by Jackson *et al* [102]. Concerning AlN transducers on metal substrate, Cao *et al* [103] deposited by sputtering AlN on stainless steel and implemented a copper tip mass, obtaining 5.13 μW at 69.8 Hz for 1 g acceleration. Moreover, it was observed that doping AlN with Sc, increases piezoelectric properties and electro-mechanical coupling [104, 105]. However, the measured $FoM^{T}_{31,f}$ of AlN doped Sc remains much lower thant that of pure AlN (table 10). Recently AlScN was considered as a transducer for vibrational energy harvesting, but not implemented as such [106, 107]. Le VanMinh *et al* doped AlN with MgZr [108], and fabricated a MEMS scale device with 792 Hz resonance frequency, and harvesting 1.3 μWat 0.82 g.

3.3. Potassium and sodium niobates

The report on the preparation of $KNbO_3$ dates back to Joly in 1877 [109]. The discovery of $BaTiO_3$ ferroelectric properties in 1946 led to the investigation of other similar types of materials and their properties and the first report of KN ferroelectric properties was done in 1949 by Mathias [110]. Mathias *et al* managed to grow $KNbO_3$ single crystals with up to 1 cm edge length using spontaneous nucleation and slow cooling method [111]. Since it was too conductive in nature, the dielectric property investigation could not be done but the ferroelectric nature and phase transitions from orthorhombic to tetragonal at 224 °C, and from tetragonal to cubic at 434 °C were reported [111]. In 1954, the third transition to rhombohedral at −10 °C was reported [112]. In the literature, top seeded solution growth (TSSG) and Kyrpoulus methods are extensively used to grow stoichiometric $KNbO_3$ crystals [113–115]. One of the largest KN single crystal obtained is in the range of 50 ×50 ×15 mm^3 by the TSSG method [116]. The growth of larger KN single crystals suffers from the incongruent melting behaviour at high temperatures [117] and the development of fine cracks due to the phase transitions and formation of domain structures in the system while cooling down [118]. The commercially available dimensions of KN single crystals are in the range of 10 ×10 ×3 mm^3 [119].

Growth of stochiometric KN thin films is challenging as the K_2O is volatile at high temperatures. Many works previously try to overcome this problem by trying to provide excess potassium sources. Most of the previous works use single crystalline substrates MgO, $SrTiO_3$, $KTaO_3$, $LaAlO_3$, and $KTaO_3$ substrates to obtain highly oriented and epitaxial films and the deposition techniques used include MOCVD, liquid phase epitaxy, sol-gel, sputtering, hydrothermal growth, and PLD [120–125]. The epitaxial relationships were established on these substrates. Epitaxial or preferentially oriented and stoichiometric KN films with (101) orientation are grown on (100) oriented $SrTiO_3$ and MgO substrates using PLD [122, 126]. (101) orientation presents high permittivity along the growth direction and the presence of four growth domains, rotated by 90° in the plane, imposed by the cubic substrates, reduce the expected $FoM^{T}_{31,f}$ for $KNbO_3$ films to relatively low value of 7.4 kJ cm^{-3} (table 9). These cubic substrates impose the presence of growth domains, which results in the properties equivalent to the textured films (111) oriented films were obtained on *c*-axis oriented $LiNbO_3$ substrates and polycrytalline ones on C-sapphire [127]. The expected values for the $FoM^{S}_{31,f}$ and $FoM^{T}_{31,f}$ are close to those for the standard ZnO and AlN films (table 8). Epitaxial KN film was also obtained using MOCVD on $SrTiO_3$ and MgO substrates but post-deposition annealing with a $KNbO_3/K_3NbO_4$ powder mixture was needed to reach the desired stoichiometry [128].

KN thin films on Si substrates show polycrystalline or even amorphous growth [130–132]. KN film with *b*-axis orientation on Pt(111)/Ti/SiO_2/Si grown by using the chemical solution deposition method was reported [133]. However, this textured orientation would allow attaining only $FoM^{T}_{31,f}$ of 0.15 kJ cm^{-3} and $FoM^{S}_{33,f}$ of 0.17 kJ cm^{-3}. An attempt to obtain homogenous KN film on Pt/Ti/SiO_2/Si was successful with the RF magnetron sputtering at RT followed by annealing at 800 °C for 90 min under the K_2O atmosphere [121]. But the piezoelectric properties were only measured using the piezoelectric force microscopy technique. KN thin films

were grown on TiN/SiO_2/Si which were either amorphous or amorphous with nanocrystals [121]. Most of the works focus on the improvement of film quality and obtaining stoichiometric films rather than on the piezoelectric properties. To summarize, the growth of $KNbO_3$ thin film growth need to be further optimized to offer better control of film composition and to find out a way to grow epitaxial or textured (011) orientation on electrode/substrate heterostructures, which are of special interest for both strain and stress driven harvesters (tables 8 and 9).

(K,Na)NbO_3 (KNN) based ceramics has been extensively studied in the literature as a potential candidate for PZT replacement due to its high d_{33} and high Curie temperature. Wu *et al* have reviewed the different strategies used for tuning the piezoelectric, dielectric and structural properties including phase boundaries of KNN [134]. The early attempts on the growth of crystals with compositions between ($K_{0.5}$ Na $_{0.5}$)NbO_3 and pure $NaNbO_3$ were done by Shirane *et al* [135] and the crystals obtained were of composition ($Na_{0.9}$ $K_{0.1}$)NbO_3. It is reported that KNN crystals with compositions close to K $_{0.5}$$Na_{0.5}$$NbO_3$ can be obtained using the flux method and solid-state crystal growth method but the maximum size reported is in the range of $5 \times 5 \times 2$ mm^3 [136–138]. But still, there is no report on the complete set of piezoelectric, elastic, and dielectric coefficient characterization of pure KNN single crystals. It is difficult to fabricate good quality single crystals with desired stoichiometry due to the volatilization of elements. Nevertheless, the complete set of the dielectric, elastic and piezoelectric constants was reported for the (Li,Ta) modified KNN (KNN-LT) crystals with size of $9 \times 9 \times 11$ mm^3 grown by TSSG [33].

Developing high-quality KNN-based thin films is still a challenge due to the complications in the fabrication process because of its highly volatile constituents, sodium and potassium oxides, and composition differing from stoichiometry, and secondary phase formations [134]. Evaporation of the alkali ions from the films causes the formation of oxygen vacancies in the films, leading to a high leakage current in the films which deteriorates the ferroelectric and piezoelectric properties of the films [139]. Papers have reported highly oriented growth of KNN thin films on Pt/Ti/SiO_2/Si and $Pt_{80}Ir_{20}$ substrates [140–142]. KNN films on SiO_2/(001)Si substrates showed amorphous nature at low temperatures (∼350 °C) but formed more crystalline films with a preferred orientation of (001) at 450 °C–550 °C using RF magnetron sputtering [143]. (001) oriented KNN films with thickness of 3 μm were grown on (100)Pt/MgO(100) epitaxially and on (111)Pt/Ti/SiO_2/(100)Si in a textured way by using RF magnetron sputtering [91]. The high transverse piezoelectric coefficients $e_{31,f}$ (−3.6 and −5.5 C m^{-2}, respectively) were measured for these films. Although from the tensors point of view, no difference is expected for the (001) tetragonal textured and epitaxial films, the big difference in relative dielectric constant was found (158 and 598, respectively), indicating permittivity dependence on the microstructure and defects in the film. The corresponding calculated $FoM^T_{31,f}$ were 7.0 kJ cm^{-3} and 5.1 kJ cm^{-3} (table 10), which are by order of magnitude lower than that expected for the KNN-LT films (table 10), but they are very similar to that of the single crystals KNN-LT (5.6 kJ cm^{-3}, table 7). Piezoelectric properties were also reported for the KNN films with Na-rich compositions on Pt/MgO substrates with additional buffer layer of $SrRuO_3$ [90]. However, the FoMs of such films are less promising than that of the KNN films with K/Na ratio close to 1 (table 10). Shibata *et al* have demonstrated the d_{31} coefficient and dielectric constant dependence on the K/Na ratio in the films [92]. The $d_{31,f}$ coefficient presents its maximum at Na composition of 55% and the $e_{31,f}$ could be maximized to as high values as −14.4 C m^{-2} and leakage current could be reduced by thermal post-treatment of KNN/Pt/Ti/SiO_2/Si heterostructure, which densified the films and reduced the defect concentration [92]. Although, these films were not perfectly textured (rather polycrystalline), they presented one of the highest $FoM^T_{31,f} = 18.9$ kJ cm^{-3} measured for the lead-free piezoelectric thin films (table 10). MEMS devices were fabricated from the KNN/Pt/Ti/SiO_2/Si heterostructures by means of dry etching and it has been demonstrated that the microfabrication does not affect the KNN piezoelectric properties [93].

$(1 - x)KTaO_3 - xKNbO_3$ (KTN_x) solid solutions with compositions $x > 0.2$ present with increasing temperature trigonal-orthorhombic-tetragonal-cubic phase transitions [144]. The trigonal (3m) /orthorhombic (mm2)/tetragonal(4mm) phases are ferroelectric and cubic one is paraelectric. The transition temperatures and the symmetry of the RT phase are highly dependent on the Ta/Nb ratio [144]. The tetragonal-cubic phase transition of $KTN_{0.65}$ is at 10 °C and the compositions with $0.50 < x < 0.60$ are tetragonal at RT, while KTN with Nb-rich compositions are orthorhombic as $KNbO_3$ [144]. Moreover, the phase transition temperatures of clamped KTN thin films are modulated with respect to those of bulk KTN [145]. In a proximity of tetragonal-cubic phase transition, KTN is a very promising material with the highest electro-optic, nonlinear optic and opto-mechanical performance known for photonic applications thanks to a very high relative permittivity (>50 000), a giant Pockels effect (up to 104 pm V^{-1},) and very high Kerr coefficients ($>10^{-14}$ m^2 V^{-2}). Therefore, it was a considerable effort to synthesize these materials in the form of the single crystals. KTN crystal growth by means of the TSSG method and temperature gradient transport technique has been reported [146, 147]. NTT Science and Core Technology has claimed an ability to grow KTN crystals up to a size of $40 \times 40 \times 30$ mm^3 and KTN films with controlled thicknesses of 5–10 μm by means of liquid epitaxy [148]. KTN crystals with dimensions in a scale of 1 cm are available commercially.

As this material is not available in the form of large crystals, its application in photonic devices are limited. Moreover, as it was shown above tetragonal KTN in the form of thin films is highly promising in terms of $FoM^T_{31,f}$ for the vibrational EH applications. The main advantage of the (001) oriented tetragonal phase over the orthorhombic one is its $FoM^T_{31,f}$ insensibility to the in-plane orientation. KTN thin films with different Ta/Nb ratio have been grown on MgO, $KTaO_3$ and GaAs substrates [149–152]. The growth orientation of

KTN films on (100) MgO substrates is dependent on the Ta/Nb composition. The films containing a higher Ta fraction were oriented [010] cubic direction, while those with higher Nb fraction orienting towards orthorhombic [101] direction [151]. Cubic $K_{0.94}Ta_{0.68}Nb_{0.40}O_3$ films on GaAs show and R-sapphire grow with orientation (100) [150]. The tetragonal $KTa_{0.5}Nb_{0.5}O_3$ and $KTa_{0.6}Nb_{0.4}O_3$ on R plane sapphire show preferential (100) orientation with minor orientations (110) and (111) [153]. The *a*-axis orientation cannot offer high FoM due to its extremely high permittivity ($\varepsilon_{11}/\varepsilon_0$=1190). The *c*-axis oriented $KTa_{0.5}Nb_{0.5}O_3$ grows epitaxially on (001) $KTaO_3$ and (001) MgO substrates [154]. Further efforts are needed to obtain such tetragonal *c*-axis oriented films on bottom electrode and substrates compatible with vibrational EH applications.

Regarding the potassium and sodium niobate family, in particular the implementation of KNN to energy harvesters based on Si substrates resulted promising results. This family of material belongs to the poled ceramics group, so has similar symmetry as PZT. These piezoelectric ceramics are developed using $NaNbO_3$ and $K_{0.5}Na_{0.5}NbO_3$. For instance, Kanno *et al* [155] fabricated one of the first prototypes of KNN vibrational energy harvesters by RF sputtering, achieving 1.1 μW at 1036 Hz (@1 g), and compared the results with similar unimorph devices with PZT, having 1 μW output in the same conditions. More recently, Shiraishi *et al* deposited KNN by hydrothermal method on metal foils [156], obtaining 126 Hz resonance frequency and 7.7 μW at 1.02 g, while Won *et al* used chemical solution deposition, adding small concentration of Mn to enhance the piezoelectric properties of the film [157], obtaining a power output of 3.62 μW at 132 Hz (1 g). Among the highest PD achieved with KNN there is the work of Van Minh *et al* [129]. In this work, the device was fabricated on silicon substrate with four tip masses in order to have large frequency bandwidth and high-power output (figure 14(b)), obtaining 0.73 μW at 1509 Hz (1.02 g). Nevertheless, due to the challenges of optimization synthesis and processing of upscaling to industrial level remains one of the most important issues in its implementation.

3.4. $LiNbO_3$ and $LiTaO_3$

$LiNbO_3$ and $LiTaO_3$ single crystals are industrially produced piezoelectric materials easily accessible, rare-earth and toxic-element-free, cheap, available in the form of wafers (with diameter up to 6 inches), widely exploited for developments of acoustics and optical devices [158], and presenting similar efficiency in EH as commonly used PZT. $LiNbO_3$ and $LiTaO_3$ are ferroelectric materials that belongs to 3m point group at RT. The major advantages of $LiNbO_3$ and $LiTaO_3$ over PZT are: (a) extremely chemically inert and lead-free materials; (b) very high Curie temperatures (>1150 °C and 600 °C–700 °C, respectively) thus compatible with EH and actuation at high temperatures (PZT limit <150 °C). The piezoelectric transducers based on $LiNbO_3$ single crystals operating up to 1000 °C have been reported by Baba *et al* [159]. High-temperature strain-driven EH was demonstrated up to 500 °C and the high-temperature limit has resulted from the failure of the mechanical set-up and not from the piezoelectric material itself [160]. However, the $LiNbO_3$ and $LiTaO_3$ applications in acoustics are limited to 300 °C by the increased losses at high temperatures due to ionic conductivity. It is important to note that the requirements in terms of losses are much lower in the case of EH applications and that at RT in the form of single crystal $LiNbO_3$ and $LiTaO_3$ have very high-quality factor and low dielectric losses (typically under 0.1%) [161]. As shown above the high efficiency of the piezoelectric transduction based on $LiNbO_3$ can be attained in the crystal orientations with an oblique *c*-axis. $LiTaO_3$ presents much lower strain- and stress-FoMs than those of $LiNbO_3$ due to its lower piezoelectric coefficients (tables 8 and 9).

From the application point of view in the fields of integrated photonics, high-frequency acoustic filters, and lead-free MEMS piezoelectric transducers, $LiNbO_3$ and $LiTaO_3$ thin films are of particular interest. Despite this high industrial interest, the synthesis of the $LiTaO_3$ and $LiNbO_3$ thin films is far from being a routine due to difficulties to control and to measure in precision the nonstoichiometry of volatile Li_2O [162] on which the physical properties are highly dependent, to electrically pole the grown films, and to integrate with Si based substrates [158]. $LiNbO_3$ and $LiTaO_3$ can be grown epitaxially with different orientations ((0001)/*Z*, $(10\bar{1}0)$/*Y*, $(11\bar{2}0)$/*X*, $(10\bar{1}2)$/33°Y) on sapphire substrates [158]. They also grow epitaxially on $SrTiO_3$, $LaAlO_3$, MgO, etc (see review by Bartasyte *et al* [129] for the epitaxial relationships). The films on SiO_2/Si are polycrystalline and interact chemically through the Li_2O diffusion to the substrate. The literature reports $LiNbO_3$/$LiTaO_3$ films on the bottom electrodes containing heterostructures or metal substrates are rare. Recently, 2–4 μm thick $LiTaO_3$ films on stainless steel substrates were fabricated by means of sol-gel method and post thermal treatment for the vibrational EH applications and the reported generated PD by this heterostructure was 4–20 nW m^{-3} at acceleration of 1.5 g [163]. The *c*-axis textured films can be grown on the (111) Pt film electrodes. However, the *c*-axis oriented films do not offer high electro-mechanical coupling and such films cannot be competitive with the standard AlN or ZnO films available at industrial level. Recently, $(10\bar{1}2)$/33°Y textured growth of $LiNbO_3$ by means of direct liquid injection chemical vapor deposition (DLI-CVD) was achieved on textured $(10\bar{1}2)$ $LaNiO_3$ buffer layer on SiO_2/Si based heterostructures [164]. As textured $(10\bar{1}2)$ $LaNiO_3$ layers can be sputtered on any substrate/heterostructure withstanding 500 °C, this approach allows to grow highly coupled orientation $LiNbO_3$ films on technology important heterostructures based on Si and Pt electrodes. The challenge remaining to overcome is the electrical poling of these films in order to attain single ferroelectric domain state which would allow to attain high $FoM^T_{31,f}$ for the textured $LiNbO_3$ films. Additional difficulty in growing thick $LiNbO_3$/$LiTaO_3$ thin films is their big thermal expansion in the *XY* plane, which is higher by a factor of 10 than that of the Si substrates. This results in the high tensile stresses and cracking of the thick films on Si substrates.

To overcome these difficulties with the grown $LiNbO_3$ and $LiTaO_3$ thin films and to respond to the industrial and academic demand, the top-down fabrication methods of thin films

from the bulk $LiNbO_3$/$LiTaO_3$ wafers were developed. The main advantages of top-down methods are the single-crystal and single-domain quality of films and the free-choice of the film orientation (independent on the crystallographic planes and the substrate) enabling the maximum possible FoMs possible. Moreover, even very thick films single-crystal films on flexible Si, metal or polymer heterostructures, compatibles with the energy harvesting/actuation applications can be fabricated by polishing/bonding techniques [30, 165]. At present, the ion-slicing and polishing/bonding techniques reached the industrial maturity and such single-crystal films are available from several enterprises (SOITEC, NANOLN, NGK, Paltrow Technologies, etc).

In the past, EH demonstrations were investigated only by using industrially available $LiNbO_3$ wafers with a thickness of 300–1000 Å. The use of $LiNbO_3$ as a transducer has been considered in some papers using inverted domain bulk plates or simple bulk single crystal. For instance, Funasaka *et al* [166] fabricated a piezoelectric generator where an impact hammer applied vibrations to $LiNbO_3$ 140°-Y crystal cut beam and electrical energy was yielded from the vibrations, obtaining 10 V in open circuit conditions and high resonance frequency 5.17 kHz. Nakamura *et al* [26] identified $LiNbO_3$ 137°-Y crystal cut, as the most suitable for bending actuation. This orientation presented piezoelectric strain coefficient d'_{23} =30 pC N^{-1}, very low dielectric constant ($\varepsilon'^{T}_{22}/\varepsilon_0 = 58.8$), and thus high transverse electro-mechanical coupling factor, $K'^{2}_{23} = 26\%$. Unfortunately, this single crystal orientation is still not commercially available (as industrial demand of $LiNbO_3$ actuators and harvesters is still not present), and can be purchased only as custom one. More recently, Vidal *et al* [29] designed and tested a low-frequency vibration energy harvester, using the same reversed domain technology and obtaining a thick bimorph $LiNbO_3$ 128° Y-cut patch (1 mm) bonded with epoxy on a metal substrate. However, they achieved low resonance frequency 32 Hz and high PD 9.2 mW g^{-2} with a very large resistive load 65 MΩ, because of very poor capacitance (38 pF). Moreover, Bedekar *et al* [167] have studied mechanical EH for high-temperature applications, where Y-36° bulk single crystal $LiNbO_3$ was mechanically excited in thickness mode. Also, Kawamata and Morita worked with $LiNbO_3$ (Y-36° crystal cut) in thickness mode as stack actuator [168, 169], finding it suitable for a multilayered device.

In the case of micro-energy harvesters where lateral dimensions are limited, thick wafers cannot be used due to issues in impedance–matching with EH circuits as well as structural compatibility with the substrate. Moreover, bulk $LiNbO_3$ crystals are very brittle and only low displacement can be attained. Therefore, $LiNbO_3$ film technology has to be implemented in vibrational EH to overcome such issues and provide realistic operations. Despite their promising properties, the application of $LiNbO_3$ films in piezoelectric vibrational EH was started to study very recently [46]. A considerable effort has been made towards their integration in the conventional processing of MEMS and EH devices. We have identified the optimized orientation for our application among the commercially

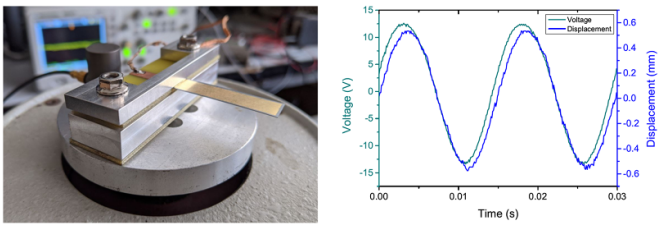

Figure 15. (*YXl*)/128° $LiNbO_3$ /brass harvester with tip mass: photo of mounted cantilever set-up (left) and characterization of voltage and displacement in open-circuit conditions (right) [30].

available $LiNbO_3$ single crystal cuts, considering its electromechanical properties as well as the possibility of integration in a suitable micro-fabrication process. A beam with a tip mass, based on the 128°Y $LiNbO_3$ single-crystal film bonded on silicon, was investigated for the vibrational EH at low frequencies (150 Hz). Highly coupled devices ($K^2 = 2.8\%$) with high quality factor ($Q = 396$) have been demonstrated. The measured PD 965 μW cm^{-2} g^{-2}, which is among the highest reported values for vibrational harvesters based on lead- and lead-free materials [46]. The vibrational microharvesters based on thick $LiNbO_3$ films were successfully applied for the wireless sensor nodes [170] and the e-gadgets [171]. The $LiNbO_3$ films were also integrated with the flexible metal substrates to overcome the fragility issues of the silicon beams [30, 164]. The (YXl)/128° $LiNbO_3$ /Brass harvester (figure 15) with tip mass for an active area of 260 mm^2, a resonance frequency of 66 Hz, and an acceleration of 0.1 g, the PD is equal to 612 μW cm^{-2} g^{-2}. Even though this value is smaller than the silicon counterpart, if we consider the normalized power densities, we achieved 9.22 μW cm^{-2} g^{-2} Hz^{-1} and 371 μW cm^{-3} g^{-2} Hz^{-1}, which is an improvement compared to previous results on Si substrates (6.4 μW cm^{-2} g^{-2} Hz^{-1} and 149 μW/cm^{-3} g^{-2} Hz^{-1}). Further works are undergoing on the optimization and fabrication of bimorph structures to further increase the harvested PD. The first integrated MEMS-scale energy converters based on single-crystal $LiNbO_3$ films were reported last year [172]. $LiNbO_3$ MEMS cantilevers under flexural deformation with acceleration of 2.5 g have produced a PD of 1.9 nW·mm^{-3}·g^{-2} at resonance frequency of 4.1 kHz. These lead-free vibrational energy scavengers at MEMS scale open new possibilities for the autonomous integrated systems, miniaturized sensors and transducers.

3.5. $BiFeO_3$

Bulk and thin films of $BiFeO_3$ belonging to the point group as $LiNbO_3$ and $LiTaO_3$ present a competitive FoM for the stress-driven energy harvesters although, the thin films have to be oriented with $(10\bar{1}2)$ planes parallel to the surface (tables 7 and 9). $(10\bar{1}4)$ orientation with single-crystalline or textured quality shows also reasonable performance. In the case of strain-driven harvesters, even textured (0001), $(10\bar{1}2)$ and $(10\bar{1}4)$ (corresponding to $(111)_{PC}$, $(100)_{PC}$ and $(110)_{PC}$ orientations in pseudo-cubic cell, respectively) $BiFeO_3$ show high potential for both 33 and 31 transduction modes (table 8).

Several papers report the growth of $BiFeO_3$ single crystals from millimeter to centimeter size. Crystals are grown by melting Bi_2O_3 & Fe_2O_3, and sometimes B_2O_3 is added as a flux, reducing the mixture liquidus [173, 174]. Works on Bi_2O_3 and Fe_2O_3 quality and in-depth knowledge Bi_2O_3–Fe_2O_3 phase diagram [175] lead to the improvement of the final BFO single crystal quality. X-ray analysis have reported that growth direction in a flux is along the polar axis $[0001]_H$ of the structure [176], indicating the dense planes and the fast growth orientation, which can be obtained in self-textured films. Laser-diode heating floating-zone method enabled the growth of so far the largest $BiFeO_3$ single crystals with a diameter of 4 mm and a length up to 50 mm [177]. The advantage of this technique is the possibility to reshape the single crystal and to adapt it to the study of specific properties [178]. Finally, fluoride ion-assisted hydrothermal method can be used to grow various size of BFO micro-crystals. The produced nanoplates lateral size range from 6.5 to 14,4 μm wide with a thickness which can be tailored from 80 nm to 1,14 μm [179].

The A/B site single or co-doping are the most established methods used to tune properties of BFO films or ceramics [180, 181]. Light BFO doping with rare-earth elements [182] or transition metals [183] have been used for the tuning of multiferroic, ferroelectric, dielectric, magnetic and photovoltaic properties [184–186]. Highly doped systems also present a potential in an enhancement of the physical properties. As it has been demonstrated for $BiFeO_3$–$BaTiO_3$ system, the superior concentration of doping elements may result in inhomogeneous solid solutions and the material may present multiple phases [187]. Modifications induced by doping are not only functional but also structural. In the case of fibers, the doping helps to increase a specific surface area and a pore size and to reduce a grain size [188]. The doping is the favorite techniques to tune BFO properties due to its simplicity. However, growth process conditions can also have a significant effect on the physical and structural properties. For example, a processing atmosphere and a gas ratio used in the fabrication of ceramics or films can have an influence on the microstructure and the quantity of impurities as well as on the photovoltaic properties [184, 189]. Superlattice structures have been investigated as another way to combine material properties of BFO and other functional materials. Most studied system is $BiFeO_3$–$BaTiO_3$ superlattices with the special interest for the magnetoelectric coupling [190–192]. Tunability of ferroelectricity and ferromagnetism have also been investigated in other multilayers such as $BiFeO_3$–$BiMnO_3$ [193], $BiFeO_3$–Fe_3O_4 [194] and $BiFeO_3$—$La_{2/3}Sr_{1/3}MnO_3$ [195], as well.

As for $LiNbO_3$, the major advantage of $BiFeO_3$ for high temperature applications is its very high Curie temperature (830 °C). The Curie temperature can be tuned by doping or by changing a stoichiometry. The dielectric behavior was investigated over a wide range of temperature (from RT to at least 350 °C) for doped and undoped $BiFeO_3$[196], $BiFeO_3$–$BaTiO_3$ [197, 198] or related ceramic systems [199, 200]. The permittivity as well as the dielectric loss increase with the increase of the temperature. The $BiFeO_3$–$PbTiO_3$ ceramic shows an increase of conductivity up to 350 °C and change of the permittivity and dielectric loss [201]. A temperature dependence of d_{33} piezoelectric coefficient has been reported for the $(1-x)BiFeO_3$–$xBaTiO_3$ ceramics [202]. For the ceramics with $x = 0.265$, the coefficient d_{33} increases up to 280 °C due to the increase of the dielectric constant and then it decreases rapidly at higher temperatures due to thermal depolarization. The maximum of d_{33} is observed at lower temperatures for the higher x values. A study of Ca-doped $BiFeO_3$–$BaTiO_3$ ceramics has found a similar behavior for the electromechanical coupling. [187] In some modified BFO systems, a doping or a combination with lead-free material may lead to ceramic properties with high thermal stability [203]. For example, $LiNbO_3$ doping gives the permittivity stability in the 200 °C–500 °C temperature range [204]. Mg-doped $BiFeO_3$–$BaTiO_3$ ceramics presents a constant d_{33} coefficient up to 400 °C [205]. Few studies can be found on the temperature dependence of $BiFeO_3$ film properties. The permittivity increases with the increase of the temperature in the temperature range from −193 °C to 27 °C [206] and then it remains stable up to 400 °C [207].

The BFO thin film properties are also dependent on a strain state which can be tuned by a lattice mismatch between BFO and its substrate. The strain effect on the bandgap and the ferroelectric properties has been demonstrated for the BFO films on $SrRuO_3$ buffer layer using different substrates such as $LaAlO_3$ (LAO), $SrTiO_3$ (STO), MgO and TiN-buffered Si substrates [208]. Compressive strain in the films can be varied by chaging the thickness of a strain tuning layer or of the BFO itself [209, 210]. Finally, the strain engineering can be achieved via self-assembled nano composites, such as $BiFeO_3$-$CoFe_2O_4$, in which the structural constraints between two material enable a magneto-structural coupling between antiferromagnetic BFO and ferrimagnetic CFO [211].

The final step needed for the improvement of the piezoelectric properties of $BiFeO_3$ is the electrical poling in order to control the polarization state. The polarization relaxation, the polarization fatigue, and the polarization itself can have influence on conduction currents in the material. A linear dependence of the conduction current on the polarization was measured [212]. Therefore, the poling can help to improve not only the piezoelectric transduction efficiency but also the photovoltaic efficiency in pure $BiFeO_3$ [213] or multi-doped BFO systems [214] and so bring adapted solutions for either EH or sensor applications [215]. In a similar way, the application of magnetic field can be used to tune photoelectrochemical behaviors [189].

Epitaxial growth of $BiFeO_3$ by different deposition techniques (MOCVD, PLD or MBE) has been mainly studied by using single crystal substrates, such as $SrTiO_3$ with or without $SrRuO_3$ bottom electrode, and conductive Nb: $SrTiO_3$ [180, 216–219]. The BFO film orientation in pseudo-cubic settings matches the one of $SrTiO_3$ ($(100)_{pc}$, $(110)_{pc}$ and $(111)_{PC}$, for the corresponding hexagonal orientations see table 2). The epitaxial BFO growth was also obtained by means of spin-coating [220], sputtering [208], and PLD [221]. The $SrRuO_3$ (SRO) is one of the most use bottom electrodes for deposition of BFO doped and un-doped systems on single crystal substrates or Si-based structures [222]. Independently of the deposition technique (spin coating [220], sputtering [208] or by PLD

[221]), $(100)_{PC}$ and $(111)_{PC}$ epitaxial BFO growth have been obtained on epitaxial SRO bottom electrodes, which orientation is determined by substrate orientation [189, 223–225].

Other structurally matching single-crystal substrates (MgO, $KTaO_3$, $LaAlO_3$ and YSZ) [226] or in combination with bottom electrodes have been used for the epitaxial BFO growth, as well. Such epitaxial BFO films on cubic substrates do not present potential for the stress-driven harvester applications due to incompatibility of the substrates and the four growth domains in the substrate plane resulted from the cubic symmetry of the substrate, which destroys the high FoM^T values. The measured e_{31} piezoelectric coefficients of $(111)_{PC}$ and $(100)_{PC}$ epitaxial BFO films on SRO/STO were -1.3 pC N^{-1} and -3.5 pC N^{-1}, respectively [82]. Similar e_{31} value of -4.3 pC N^{-1} was also reported for the $(100)_{PC}$ films on STO:Nb substrates [83]. The permittivity of these films was higher than that calculated for BFO films (see table 10) and the $FoM^T_{31,f}$ of $(100)_{PC}$ films was as high as 10 kJ cm^{-3} (however, this does not overpass the performance of standard AlN films).

Direct growth of BFO on Si has resulted in (100) oriented and polycrystalline films obtained by spray pyrolysis [227] and by laser-MBE [228], respectively. $LaNiO_3$ is a conductive perovskite which displays promising results as a bottom electrode and a growth template for high quality BFO films on Si. The studies show that both $LaNiO_3$ and $BiFeO_3$ are prepared by sol-gel process on Si based substrates. The polycrystalline BFO films with orientation $(100)_{PC}$ and $(110)_{PC}$ preferential orientations on $LaNiO_3$ were synthesized by means of sol-gel technique on Si substrates [229–231]. The e_{31} for the textured $(100)_{PC}$ BFO films on $LaNiO_3$/Si [84, 85] were the same as those reported for the $(110)_{PC}$ epitaxial films [82, 83] (table 10). Transparent conductive oxides, FTO or ITO, coated on glass or quartz substrates were also served for polycrystalline BFO depositions [232], and these structures were used for the studies of photovoltaic properties [233, 234]. IrO_2 can be also used as bottom electrode and buffer layer for the growth of polycrystalline BFO on Si as demonstrated by MOCVD method [235]. Platinum bottom electrode on TiO_2(or Ti)/SiO_2/Si has been used for depositions of polycrystalline BFO by means of sol-gel and PLD [236–238]. Polycrystalline BFO with preferential $(100)_{PC}$ orientation has been obtained on (111) Pt by means of a chemical solution route [239]. More recently, nanosheets of $Ca_2Nb_3O_{10}$ have been successfully used as a seed layer for highly oriented $(100)_{PC}$ BFO grown on Si [240]. $BiFeO_3$ films directly deposited on metallic substrates have not been intensively investigated. Nevertheless, few attempts were reported: BFO with a preferential $(110)_{PC}$ orientation deposited by PLD on flexible magnetic Ni tapes [241] and polycrystalline films screen printed on noble metal foils (Ag, Au and Pt) [242]. The thin film synthesis with high quality texture on low-cost substrates such as metal ones still need to be pushed forward. As discussed above, both textured $(100)_{PC}$ and $(110)_{PC}$ films presents a particular interest for the strain-driven energy harvesters while their performance will limited in the stress-driven ones.

Finally, despite its huge interest for EH very few devices have been designed and tested [85, 243]. Thanks to the various strategies explored, we have a broad understanding of the material possibilities and huge flexibility to adapt the material to the working environment of EH device [244]. Several works report the structures for EH applications, based on $BiFeO_3$ films on silicon or $SrTiO_3$, deposited by means of magnetron sputtering [85, 245], having 151.2 Hz resonance frequency with 2.4 μW power output at 0.3 g. Yoshimura *et al* achieved 98 Hz resonance for 2 nW power output (0.05 g) by implementing BFO films on Si, grown by means of sol-gel method [243, 246].

3.6. Quartz and langasites

Quartz is a trigonal material (point group 32) and its first phase transition occurs at 573 °C from α-quartz to β-quartz [247, 248] at atmospheric pressure. At about 900 °C β-quartz becomes fully HP-tridymite, which transforms at about 1475 °C into cristobalite. Finally, quartz melts at about 1750 °C. Quartz is not pyroelectric and not ferroelectric, thus, it does not require electrical poling. The piezoelectric coefficients and permittivity of quartz are very low. Although, the electromechanical coupling and strain and stress FoMs are low ($FoM^T_{31} = 0.7$ kJ cm^{-3} & $FoM^S_{33} = 1$ kJ cm^{-3} for X-cut quartz), the quartz is the 2nd most abundant mineral after feldspaths. In the nature, crystal can measure several meters in length. Commonly, the hydrothermal growth is used at industrial scale (Neyco, Nano Quarz Wafer, Quartz unlimited) for synthesis of high-quality quartz crystal with lateral dimensions up to 300 mm [249–251]. The synthetic quartz crystals present high-quality factors and high-thermal stability of properties and they are used in optics [252], the microelectronic industry [253], and sensors/microbalances [254–259]). This conventional autoclave method is time and energy consuming (growth rate between 0.25 mm d^{-1}–0.35 mm d^{-1} [260]) but natural quartz crystals are not used due to low quality, limited transparency, inclusions/dislocations, etc [261]. Nevertheless, such natural quartz crystals could be considered for the environmentally-friendly and cheap piezoelectric EH applications which require only small amounts of energy or very low frequency of sensing. Thick quartz films could be fabricated on metal substrates by bonding and polishing technique.

Only a few groups work have been working on the growth of quartz thin films in the last 20 years because it requires high temperature to crystallize the films. It is really hard to grow crystalline and epitaxial quartz on Si and converting amorphous silica in quartz is a promising approach [262]. The difficulty in converting silica into quartz is related to silica stability and the really small difference in free energy of formation of both materials [263]. Takahashi *et al* demonstrated [264–266] demonstrate an epitaxial growth of (001) and (011) quartz parallel on C- and A-sapphire by means of catalyst-enhanced atmospheric pressure vapor phase epitaxy, respectively. For this purpose, two quartz buffer layers (with thicknesses of

100 nm and 50 nm)) are used in order to maximize the quality of the final quartz film with thickness of 100 μm. An AT-cut surface was obtained: the tilt from (011) face is obtained by tuning the second buffer layer thickness. Quartz layers with thicknesses up to 100 μm, obtained by means of vapor phase epitaxy, are studied for the applications of bulk acoustic wave devices for instance [266]. Quartz films can be grown epitaxially on (100) Si by means of soft chemistry (sol-gel method) thanks to the use of a catalyst (Sr and Ca are the most used ones). The epitaxial relationship of Si (100)//alpha-quartz (100) and Si (010)//alpha-quartz (010) were reported [262, 267, 268]. Note that a minimum thickness of amorphous silica is needed for the quartz nucleation. The monolithic implementation of sub-micron epitaxial quartz films on Si in sensors is under study [269].

Langasite family materials with general formula $A_3BC_3D_2O_{14}$ (A–decahedral site, B–octahedral site, C and D–tetrahedral site) are synthetic piezoelectric materials interesting for the absence of Curie point and phase transition up to their melting point (usually >1400 °C) and for their non-pyroelectricity and non-ferroelectricity [270]. The most studied material from this class is the langasite with the chemical formula of $La_3Ga_5SiO_{14}$ (LGS), belonging to the same trigonal point group 32 as quartz. Piezoelectric LGS has no phase transition from RT to melting point at about 1470 °C where Ga-bearing lanthanum silicate forms [271]. The conductivity increases by several orders than La is partially replaced by Sr in LGS [272, 273].

The synthesis of homogeneous LGS crystals is more difficult than that of quartz because of the mobility of gallium oxide and oxygen nonstoichiometry. The window on phase diagram enabling the formation of LGS is narrow [271, 274]. Thus, the crystallization of LGS is extremely dependent on the composition of the melt and the migration gallium oxides at high-temperatures make difficult to obtain homogenous crystals with big dimensions. However, single crystal wafers with diameters up to 100 mm, grown by Czochralski method, are available in industry [275] (Phila Optics Inc. MSE supplies, etc).

Electromechanical coupling factors and FoMs of LGS are higher than those of quartz, but their values are still low. The quality factor is high but lower than quartz. This is one of the most used crystals for high temperature surface acoustic wave (SAW) sensors due to its high-temperature piezoelectricity and stability [276–280]. Thermal treatments up to 1000 °C for several days did not induce any noticeable change in the LGS surface morphology and SAW resonance behavior. Bedekar *et al* [167], comparatively studied mechanical EH from single crystal materials (YCOB, LGS, and $LiNbO_3$) for high-temperature applications, it was shown that although LGS and YCOB PD is three orders of magnitude lower than that of PZT, the remains the same at 600 °C as at RT.

There are few literature reports on the growth of LGS films. (0001) oriented LGS films with thickness of 300 μm on (111) $MgAl_2O_4$ substrates were grown in time of 30 min by means of liquid phase epitaxy $PbO:Bi_2O_3$ flux [281]. (110) oriented films with thickness of 1 μm on SiO_2(200 nm)/Si were obtained by means of sol-gel method followed by crystallisation during post-growth annealing at 1300 °C [282]. PLD growth of LGS films with thicknesses up to 3 μm on LGS and Si (with native oxide and oxidized one) substrates was studied, as well [272]. In the case of Si substrates, the crystallization after annealing was observed only on non-oxidized substrates. High temperature is mandatory (over 1000 °C) for good crystallinity of heteroepitaxial LGS layers (the homoepitaxial layers crystallize at lower temperatures) [281]. It seems to be difficult to obtain a pure LGS phase (formation of gallium oxide or lanthanum oxide) with only single orientation [273].

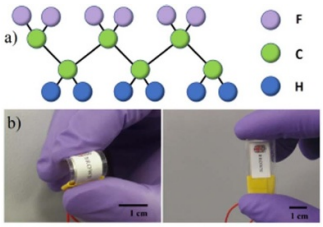

Figure 16. PVDF flexible energy harvesting: (a) polymeric chain structure; (b) flexible energy harvester on paper from Won *et al*. Reprinted from [283], with the permission of AIP Publishing.

3.7. PVDF

PVDF is a polymer material that has been used in EH due to its flexibility and robustness. It becomes piezoelectric after stretching during sintering, to induce a polar phase. Figure 16 represents how carbon atoms are forming a polymeric chain with fluorine and hydrogen atoms. This chain can be poled through electric field as in the case of ceramics. They are used on flexible substrates like plastic polymers or on paper (figure 16) [283]. They have small strain piezoelectric coefficient, but due to a small permittivity, the electro-mechanical coupling is comparable to AlN or ZnO. In EH they can be used in body-motion devices. Due to relatively easy manufacturing process, they can be used with a large surface and mass, as in [42], where Song *et al* achieved 112.8 μW at 34.4 Hz (0.5 g). However, the drawbacks of PVDF are the low figure of merit and high sensitivity to temperature (maximum operational temperature is 150 °C). Rammohan *et al* implemented a multilayer and a multistep PVDF harvester, with partial active cover of the beam, obtaining 4.53 μW at 33.3 Hz and 8.59 μW at 30.7 Hz respectively, in same acceleration conditions (0.5 g) [284].

4. Discussion and concluding remarks

To summarize, better performance of piezoelectric energy transducers in comparison to those based on lead containing materials can be obtained by using environmentally friendly materials in the bulk or thin film form. In particular, 137°Y-$LiNbO_3$ and $BiFeO_3$ are interesting for the bulk stress-driven transducers. The extremely high performance (overpassing that of lead-based materials) is expected for the bulk transducers based on 137°Y-$LiNbO_3$ not only due to very high

transverse FoM^T value but also due to very high-quality factor. In the thin-film based vibrational energy harvesters $BiFeO_3$ and $LiNbO_3$show high-performance in the form of the single-crystalline or textured $(10\bar{1}2)$ oriented films. The highest FoM_f^T values for the MEMS vibrational energy transducers can be obtained by $KNbO_3$ based thin films such as (001) $KTN_{0.53}$, (001) KNN-LT and (011) $KNbO_3$ films, in which the high performance is preserved also in the case of the textured films.

In the case of the strain-driven bulk harvesters, (011) $KNbO_3$, $BiFeO_3$ and $LiNbO_3$ show the best performance for transverse mode, while (011) $KNbO_3$, KTN and $BaTiO_3$ are more adapted for the longitudinal one. Such transducers based on lead-free piezoelectric thin films such as $BiFeO_3$, $BaTiO_3$, LiNbO3 and $KNbO_3$ based materials also show very high performance (much better than that of PZT films). Moreover, the $FoM_{33,f}^S$ of these materials is little dependent on the misorientation in the substrate plane allowing to expect such high performance in textured films, as well.

However, the properties of grown films are not only by the clamping of the substrate, but also frequently they are not single-crystalline and may contain various types of structural defects (such as grain boundaries, growth domains, twins, dislocations, nonstoichiometry, point defects, strain gradients, etc). Therefore, the physical properties of the grown films may significantly differ from of the bulk single-crystals and those estimated by taking into account the substrate clamping effect (equations (34)–(44)) as it was shown in the table 10. Moreover, the grown ferroelectric films contain the ferroelectric domains, which tend to average to zero the piezoelectric tensor components therefore, these films require electrical poling post-processing. As discussed above, the polycrystalline films do not present particular interest for the piezoelectric transducers due to their low piezoelectric efficiency. Moreover, the piezoelectric thin films have to be grown on the cheap and big-scale substrates containing a bottom electrode. The most commonly used substrates are Si due to its compatibility with MEMS technology and metal foils due to their robustness and flexibility. In order to be applied for the piezoelectric energy harvesting, the piezoelectric thin films have to offer a high FoM. As demonstrated above, the high FoM requires the thin films with the controlled out-of-plane orientation and in the case of highly anisotropic materials even the defined in plane orientation. Taking into account that the piezoelectric thin films have to be grown on the Si substrates containing amorphous SiO_2 surface layer (native or deposited for the electrical isolation from the semiconducting Si substrate) or polycrystalline metal foils, the in-plane orientation control becomes impossible. The epitaxial growth of ferroelectric thin films was reported on the (100)$SrTiO_3$/(100)Si templates, in which amorphous SiO_2 was eliminated before the epitaxial growth of $SrTiO_3$ by molecular beam epitaxy [56]. Nevertheless, the cubic in-plane symmetry of this template induces four growth domains rotated by 90° in the substrate plane in the anisotropic orientations of the films such as for example $(10\bar{1}2)$ orientation of trigonal materials. As mentioned above, the presence of these domains will result in the averaging of the in-plane properties and the resulting coefficients will be equivalent to those of the textured films. The films with several orientations in the plane are suitable for the strain driven harvesters operating in longitudinal mode as their FoM is little dependent on the in-plane orientation (table 8). Nevertheless, the high transverse FoM_T can be attained in textured or epitaxial films with growth domains of (001) oriented tetragonal films (KTN, KNN, $BaTiO_3$), (011) orthorhombic $KNbO_3$ and $(10\bar{1}2)$ $LiNbO_3$ and $BiFeO_3$ films (table 9). In general, the material has to present the piezoelectric, dielectric and elastic coefficients, implied in the FoM, little dependent on the in-plane orientation.

The choice of the bottom electrode is mainly limited by the deposition temperature of the piezoelectric thin film. Many crystalline materials require relatively-high deposition temperatures therefore, frequently used bottom electrodes for the piezoelectric thin films are noble metals such as Pt and Ir, or conducting oxides such as $SrRuO_3$, $LaNiO_3$, IrO_2, RuO_2, etc (111) Pt and $(10\bar{1}2)$ $LaNiO_3$ are also used for the growth orientation templates, as they grow naturally textured with these orientations on any substrate. Conducting $SrTiO_3$:Nb substrates enables epitaxial growth of many perovskite materials and characterization of their piezoelectric an dielectric properties. However, these substrates are available only with small dimensions and they are very expensive.

Additionally, the piezoelectric thin film thickness, required for the harvesting or actuation applications, is in the order of several microns, which adds additional difficulty in an orientation control of the grown thin films. Again, the top-down method—bonding/polishing of single crystals or ceramics do not have this limitation and the fabrication of thick films is much easier than the thin films. Very high-output power (1.2 mW for system of six beams), obtained from low frequency vibrations, was reported for the piezoelectric energy harvester based on bimorph PZT/$LaNiO_3$/HfO_2/Ni/HfO_2/$LaNiO_3$/PZT structure thanks to the high FoM of the optimized PZT layers with thicknesses of 5.4 μm [285].

The FoM is certainly important, but it only tells how much electrical energy is stored in the piezoelectric material subject to a strain. In reality the overall coupling coefficient (which differs from that of the material defined above) including the passive parts count as well. Moreover, the damping by piezoelectric harvesting should be close to the other mechanical losses of the system. Finally, the electrical impedance must be matched to the charge collecting circuit. This means that the harvester fabricated from the materials with high FoM would not necessarily be of high performance if the design of mechanical and electrical parts is not adapted. Thus, EH from vibrations and motions requires a total holistic approach from vibration or movement source, materials, MEMs to the electronic circuit storing energy [6].

A summary of the state of the art of the Pb-free energy harvesters in transverse mode is presented in table 11 and figure 17. All materials are compared in terms of areal PD normalized with respect to the operational/resonance frequency(normalized power density, NPD). The growth of tetragonal and hexagonal films with (001) out-of-plane orientation is well mastered for KNN, AlN and ZnO in the state-of-the-art. Therefore, it is not surprising that in the case of the

Table 11. Comparison of Pb-free piezoelectric harvesters in terms of areal power density (PD) and normalized with respect to the operational/resonance frequency (NPD).

Material	Power (μW)	a (g)	Freq. (Hz)	Areal PD (μW cm^{-2} g^{-2})	Areal NPD (μW cm^{-2} g^{-2} Hz^{-1})
PZT [286]	423	1.5	143.5	348	2.43
PZT [287]	321	3	100.8	65	0.64
PZT [286]	9	0.15	72	1039	14.43
PZT-5H [288]	40	0.2	36	490	13.61
PMN-PT [289]	1850	3.2	102	361	3.54
PZN-PT [290]	430	0.3	37.5	6336	176.95
KNN [157]·	3.62	1	132	72.4	0.55
AlN [101]·	32	0.5	58	196	3.38
AlN [99]·	20.5	0.28	210		(249)
ZnO [96]	1.3	1	1300		(3.0)
BFO [85]·	2.4	0.3	151	—	
BFO [83]	0.002	0.05	98	27.1	
PVDF [284]	8.59	0.5	30.8	19	0.62
LN (YXl)/128°	41.5	0.1	105.9	965	9.11

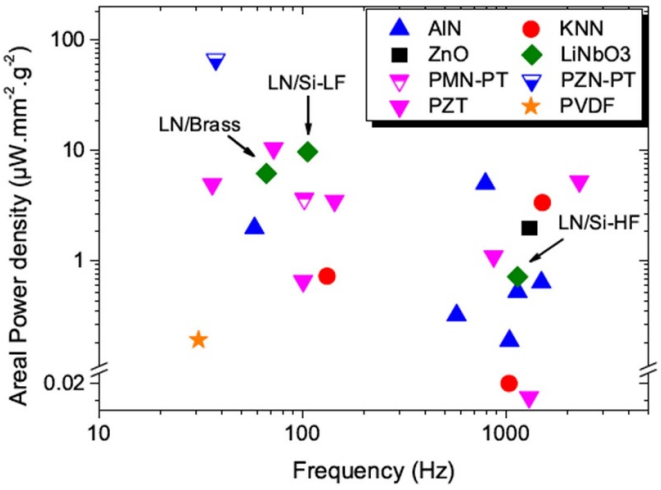

Figure 17. Comparison of state-of-the-art harvesters for low and high frequency applications. $LiNbO_3$ devices displayed with the following notation: $LiNbO_3$ on silicon device for high frequency application (LN/Si-HF); $LiNbO_3$ on silicon device for low frequency application (LN/Si-LF); $LiNbO_3$ on brass substrate for low frequency application (LN/Brass).

high-frequency energy harvesting, the more mature Pb-free material so far is AlN films, which in terms of PD is showing comparable results to Pb-based MEMS devices, especially when packaged in vacuum conditions. One can note also a good performance of KNN and ZnO films. The films of more anisotropic materials such as $BiFeO_3$, $LiNbO_3$ and $KNbO_3$ although theoretically presenting much higher FoM tha AlN or ZnO, they need further developments not only to optimize their physical properties but also attain the growth of orientations offering high FoM.

In the case of the low-frequency energy harvesting, the lead-free based materials are dominating in the high-performance devices (figure 17). Nevertheless, $LiNbO_3$ is showing the same performance as PZT in low-frequency vibrational energy harvesters. $LiNbO_3$ is available in a form of single crystals with big dimensions and of reasonable price (25$/6 inch wafer) and the single-crystal thick films with custom orientation offering extremely high FoM were fabricated by bonding-polishing on Si or metal substrates.

To summarize, lead-free materials are able to compete with lead-based ceramics in the EH applications. Generally speaking, wurtzites (ZnO and AlN) have lower FoMs, but they present other advantages: biocompatibility, technological maturity, implementation with CMOS technology. Therefore, these materials are in particular interesting for the MEMS scale devices. KNN films are gaining in the maturity of the growth process and it is another potential lead-free material for piezoelectric MEMS. $LiNbO_3$ single-crystal films offer a low-cost solution of lead-free materials for low-frequency energy harvesting. The availability of lead-free and environmentally friendly piezoelectric materials, offering high-performance, opens new avenues for the mass-deployment of autonomous and place-and-forget sensors (IoTs and IoHs) and the communication technologies.

Data availability statement

The data generated and/or analysed during the current study are not publicly available for legal/ethical reasons but are available from the corresponding author on reasonable request.

Acknowledgments

This research was funded by the European MSCN-ITN ENHANCE program Grant No. 722496, French RENATECH network, and EUR EIPHI Program Grant No. ANR-17-EURE-0002 and French ANR project FIESTA ANR-20-CE05-0026.

References

[1] Roundy S, Wright P K and Rabaey J M 2004 *Energy Scavenging for Wireless Sensor Networks* (New York: Springer)

[2] Anton S R and Sodano H A A 2007 Review of power harvesting using piezoelectric materials (2003–2006) *Smart Mater. Struct.* **16** R1–R21

[3] Cook-Chennault K A, Thambi N and Sastry A M 2008 Powering MEMS portable devices—a review of non-regenerative and regenerative power supply systems with special emphasis on piezoelectric energy harvesting systems *Smart Mater. Struct.* **17** 043001

[4] Mitcheson P D, Yeatman E M, Rao G K, Holmes A S and Green T C 2008 Energy harvesting from human and machine motion for wireless electronic devices *Proc. IEEE* **96** 1457

[5] Safaei M, Sodano H A and Anton S R 2019 A review of energy harvesting using piezoelectric materials: state-of-the-art a decade later (2008–2018) *Smart Mater. Struct.* **28** 113001

[6] Spreemann D and Manoli Y 2012 *Electromagnetic vibration energy harvesting devices: architectures, design, modeling and optimization* Springer Series in Advanced Microelectronics Book 35 (Springer)

[7] Elvin N G, Elvin A A and Spector M 2001 A self-powered mechanical strain energy sensor *Smart Mater. Struct.* **10** 293–399

[8] Elvin N G, Elvin A A and Choi D H 2003 A self-powered damage detection sensor *J. Strain Anal.* **38** 115–24

[9] Guyomar D, Jayet Y, Petit L, Lefeuvre E, Monnier T, Richard C and Lallart M 2007 Synchronized switch harvesting applied to self-powered smart systems: piezoactive microgenerators for autonomous wireless transmitters *Sens. Actuators* A **138** 151–60

[10] Lallart M, Guyomar D, Jayet Y, Petit L, Lefeuvre E, Monnier T, Guy P and Richard C 2008 Synchronized switch harvesting applied to self-powered smart systems: piezoactive microgenerators for autonomous wireless receivers *Sens. Actuators* A **147** 263–72

[11] Shi Y, Wang Y, Deng Y, Gao H, Lin Z, Zhu W and Ye H 2014 A novel self-powered wireless temperature sensor based on thermoelectric generators *Energy Convers. Manage.* **80** 110–6

[12] Paradiso J A and Feldmeier M 2001 A compact, wireless, self-powered pushbutton controller *Ubicomp 2001* (*LNCS vol 2201*) pp 299–304

[13] Enocean GmbH *Self-powered Sensors: Energy harvesting sensors for energy-efficient, comfortable and safe buildings* (available at: www.enocean.com/en/applications/self-powered-sensors/)

[14] Micropelt GmbH *LoRaWAN room thermostat MLRTPS with setpoint adjustment and presence detector* (available at: www.micropelt.com/en.html)

[15] Bonnaud O A 2020 The technological challenges of microelectronics for the next generations of connected sensors *Int. J. Plasma Environ. Sci. Technol.* **14** e01002

[16] Beeby S P, Tudor M J and White N M 2006 Energy harvesting vibration sources for microsystems applications *Meas. Sci. Technol.* **17** R175

[17] Kiziroglou M E and Yeatman E M 2021 Micromechanics for energy generation *J. Micromech. Microeng.* **31** 114003

[18] Tang L, Yang Y and Soh C K 2013 Broadband vibration energy harvesting techniques *Advances in Energy Harvesting Methods* ed N Elvin and A Erturk (New York: Springer)

[19] He C, Kiziroglou M, Yates D C and Yetaman E 2011 A MEMS self-powered sensor and RF transmission platform for WSN nodes *IEEE Sens. J.* **11** 3437

[20] Yeatman E M 2013 Size requirements for micro-scale motion energy harvesters *Nanoenergy Lett.* **6** 9–10

[21] Wada S, Muraoka K, Kakemoto H, Tsurumi T and Kumagai H 2004 Enhanced piezoelectric properties of potassium niobate single crystals by domain engineering *Jpn. J. Appl. Phys.* **43** 6692–700

[22] Nakamura K, Tokiwa T and Kawamura Y 2002 Domain structures in $KNbO_3$ crystals and their piezoelectric properties *J. Appl. Phys.* **91** 9272–6

[23] Auld B A 1973 *Acoustic Fields and Waves in Solids* vol 1 (New York: Wiley)

[24] Nakamura K and Shimizu H 1986 Ferroelectrics Hysteresis-free piezoelectric actuators using $LiNbO_3$ plates with a ferroelectric inversion layer *Ferroelectrics* **93** 211–6

[25] 1988 IEEE Standard on Piezoelectricity: An American National Standard *ANSI/IEEE Std 176–1987*

[26] Nakamura K, Ando H and Shimizu H 1987 Bending vibrator consisting of a $LiNbO_3$ plate with a ferroelectric inversion layer *Jpn. J. Appl. Phys.* **26** 198–200

[27] Kubasov I V, Popov A V, Bykova A S, Temirov A A, Kislyuk A M, Zhukov R N, Kiselev D A, Chichkov M V, Malinkovich M D and Parkhomenko Y N 2017 Deformation anisotropy of Y + 128°-cut single crystalline bidomain wafers of lithium niobate *Russ. Microelectron.* **46** 557–63

[28] Vidal J V, Turutin A V, Kubasov I V, Malinkovich M D, Parkhomenko Y N, Kobeleva S P, Kholkin A L and Sobolev N A 2017 Equivalent magnetic noise in magnetoelectric laminates comprising bidomain $LiNbO_3$ crystals *IEEE Trans. Ultrason. Ferroelectr. Freq. Control* **64** 1102–19

[29] Vidal J V, Turutin A, Kubasov I V, Kislyuk A M, Malinkovich M D, Parkhomenko Y N, Kobeleva S P, Pakhomov O V, Sobolev N A and Kholkin A L 2019 Low-frequency vibration energy harvesting with bidomain $LiNbO_3$ single crystals *IEEE Trans. Ultrason. Ferroelectr. Freq. Control* **66** 1480–7

[30] Clementi G 2020 University of Bourgogne-Franche-Comté *PhD Thesis*

[31] Tsubouch K and Mikoshiba N 1985 Zero-temperature-coefficient SAW devices on aln epitaxial films *IEEE Trans. Sonics Ultrason.* **32** 634–44

[32] Jaffe B, Cook J W R and Jaffe H 1971 *Piezoelectric Ceramics* (New York: Academic)

[33] Huo X, Zheng L, Zhang R, Wang R, Wang J, Sang S, Wang Y, Yang B and Cao W 2014 A high quality lead-free (Li,Ta) modified (K,Na)NbO_3 single crystal and its complete set of elastic, dielectric and piezoelectric coefficients with macroscopic 4mm symmetry *Cryst. Eng. Commun.* **16** 9828

[34] Hemme P *et al* 2021 Elastic properties assessment in the multiferroic $BiFeO_3$ by pump and probe method *Appl. Phys. Lett.* **118** 062902

[35] Petousis I, Mrdjenovich D, Ballouz E, Liu M, Winston D, Chen W, Graf T, Schladt T, Persson K and Prinz F 2017 High-throughput screening of inorganic compounds for the discovery of novel dielectric and optical materials *Sci. Data* **4** 160134

[36] Jain A *et al* 2013 Commentary: The Materials Project: A materials genome approach to accelerating materials innovation *APL Mater.* **1** 011002 (Material ID: mp-23501)

[37] Yue W and Yi-Jian J 2003 Crystal orientation dependence of piezoelectric properties in $LiNbO_3$ and $LiTaO_3$ *Opt. Mater.* **23** 403–8

[38] Kovacs G, Anhorn M, Engan H E, Visintini G and Ruppel C C W 1990 Improved material constants for $LiNbO_3$ and $LiTaO_3$ *Ultrasonics Symp.* p 435

[39] Zhang R, Jiang B and Cao W 2011 Elastic, piezoelectric, and dielectric properties of multidomain $0.67Pb(Mg_{1/3}Nb_{2/3})O_3$-$0.33PbTiO_3$ single crystals *J. Appl. Phys.* **90** 3471–5

[40] Jiang W, Zhang R, Jiang B and Cao W 2003 Characterization of piezoelectric materials with large piezoelectric and electromechanical coupling coefficients *Ultrasonics* **41** 55–63

[41] Erturk A and Inman D J 2011 *Piezoelectric Energy Harvesters* (New York: *Wiley*)

[42] Song J, Zhao G, Li B and Wang J 2017 Design optimization of PVDF-based piezoelectric energy harvesters *Heliyon* **3** e00377

[43] Broadhurst M G and Davis G T 1984 Physical basis for piezoelectricity in PVDF *Ferroelectrics* **60** 3–13

[44] Jaffe H and Berlincourt D A 1965 Piezoelectric transducer materials *Proc. IEEE* **53** 1372–86

[45] Kamel T M, Elfrink R, Renaud M, Hohlfeld D, Goedbloed M, de Nooijer C, Jambunathan M and van Schaijk R 2010 Modeling and characterization of MEMS-based piezoelectric harvesting devices *J. Micromech. Microeng.* **20** 105023

[46] Clementi G *et al* 2021 A low-cost alternative lead-free piezoelectric material for vibrational energy harvesters *Appl. Phys. Lett.* **119** 013904

[47] Elfrink R *et al* 2010 Vacuum-packaged piezoelectric vibration energy harvesters: damping contributions and autonomy for a wireless sensor system *J. Micromech. Microeng.* **20** 104001

[48] Muralt P 2000 Ferroelectric thin films for micro-sensors and actuators: a review *J. Micromech. Microeng.* **10** 136–46

[49] Wada Y and Hayakawa R 1981 A model theory of piezo- and pyroelectricity of poly(vinylidene fluoride) electret *Ferroelectrics* **32** 115–8

[50] Bechmann R 1956 Elastic, piezoelectric, and dielectric constants of polarized barium titanate ceramics and some applications of the piezoelectric equations *J. Acoust. Soc. Am.* **28** 347–50

[51] Vijatovic M M, Bobic J D and Stojanovic B D 2008 History and challenges of barium titanate Part II *Sci. Sinter.* **40** 235–44

[52] Mateck.com 2021 MaTecK—$BaTiO_3$—barium titanate crystal (available at: https://mateck.com/info/batio3-barium-titanate-crystal.html) (Accessed 19 October 2021)

[53] MSE Supplies LLC 2021 $BaTiO_3$ BTO barium titanate crystal substrates (available at: www.msesupplies.com/products/batio3-bto-barium-titanate-crystal-substrates?variant=31370513907770) (Accessed 19 October 2021)

[54] Alineason 2021 Oxide—alineason (available at: www.alineason.com/produkte/kristalle/oxide/) (Accessed 19 October 2021)

[55] Park Y B, Ruglovsky J L and Atwater H A 2004 Microstructure and properties of single crystal $BaTiO_3$ thin films synthesized by ion implantation-induced layer transfer *Appl. Phys. Lett.* **85** 455–7

[56] Kormondy K *et al* 2017 Microstructure and ferroelectricity of $BaTiO_3$ thin films on Si for integrated photonics *Nanotechnology* **28** 075706

[57] Choi K *et al* 2004 Enhancement of ferroelectricity in strained $BaTiO_3$ thin films *Science* **306** 1005–9

[58] Aidoud A, Maroutian T, Matzen S, Agnus G, Amrani B, Driss-Khodja K, Aubert P and Lecoeur P H 2017 Tuning the growth and strain relaxation of ferroelectric $BaTiO_3$ thin films on $SrRuO_3$ electrode: influence on electrical properties *Eur. Phys. J. Appl. Phys.* **80** 30303

[59] Magnan H, Deleuze P, Brehin J, Plays T, Stanescu D, Flavell W, Silly M, Domenichini B and Barbier A 2020 Tuning the charge carriers migration in epitaxial $BaTiO_3$ thin-film photoanodes *J. Phys. Chem.* C **124** 10315–23

[60] Shuai Y, Zhou S, Bürger D, Reuther H, Skorupa I, John V, Helm M and Schmidt H 2011 Decisive role of oxygen vacancy in ferroelectric versus ferromagnetic Mn-doped $BaTiO_3$ thin films *J. Appl. Phys.* **109** 084105

[61] Liu Z, Deng H, Yang P and Chu J 2009 Enhanced ferroelectric properties of Fe-doped $BaTiO_3$ thin film deposited on $LaNiO_3$/Si substrate by sol–gel technique *Mater. Lett.* **63** 2622–4

[62] Wang Y, Liang W, Huang W, Gao M, Zhang Y and Lin Y 2016 Structural and optical properties of the Fe-doped $BaTiO_3$ thin films grown on $LaAlO_3$ by polymer-assisted deposition technique *J. Mater. Sci.: Mater. Electron.* **27** 6382–8

[63] Cernea M, Matei I, Iuga A and Logofatu C 2001 Preparation and characterization of Ce-doped $BaTiO_3$ thin films by r.f. sputtering *J. Mater. Sci.* **36** 5027–30

[64] Sun Y, Yang H, Xu J, Huang W, Jiang M and Chen Q 2021 The (1-x)$BiFeO_3$-x$BaTiO_3$-$Bi(Zn_{0.5}Ti_{0.5})O_3$ high temperature lead-free piezoelectric ceramics with strong piezoelectric properties *J. Mater. Sci., Mater. Electron.* **32** 19713–23

[65] Tang Z, Ge J, Ni H, Lu B, Tang X, Lu S, Tang M and Gao J 2018 High energy-storage density of lead-free $BiFeO_3$ doped $Na_{0.5}Bi_{0.5}TiO_3$-$BaTiO_3$ thin film capacitor with good temperature stability *J. Alloys Compd.* **757** 169–76

[66] Schulmeyer T, Paniagua S, Veneman P, Jones S, Hotchkiss P, Mudalige A, Pemberton J, Marder S and Armstrong N 2007 Modification of $BaTiO_3$ thin films: adjustment of the effective surface work function *J. Mater. Chem.* **17** 4563

[67] Roscow J I, Lewis R W, Taylor J and Bowen C R 2017 Modelling and fabrication of porous sandwich layer barium titanate with improved piezoelectric energy harvesting figures of merit *Acta Mater.* **128** 207–17

[68] Kwak B, Zhang K, Boyd E, Erbil A and Wilkens B 1991 Metalorganic chemical vapor deposition of $BaTiO_3$ thin films *J. Appl. Phys.* **69** 767

[69] Presti F, Pellegrino A L and Malandrino G 2022 Metal-organic chemical vapor deposition of oxide perovskite films: a facile route to complex functional systems *Adv. Mater. Interfaces* **9** 2102501

[70] Suzuki T, Nishi Y and Fujimoto M 1999 Analysis of misfit relaxation in heteroepitaxial $BaTiO_3$ thin films *Phil. Mag.* A **79** 2461–83

[71] Wagué B, Brubach J, Niu G, Dong G, Dai L, Roy P, Saint-Girons G, Rojo-Romeo P, Robach Y and Vilquin B 2020 Structural studies of epitaxial $BaTiO_3$ thin film on silicon *Thin Solid Films* **693** 137636

[72] Vehkamäki M, Hatanpää T, Hänninen T, Ritala M and Leskelä M 1999 Growth of $SrTiO_3$ and $BaTiO_3$ thin films by atomic layer deposition *Electrochem. Solid-State Lett.* **2** 504–6

[73] Falmbigl M *et al* 2017 $BaTiO_3$ thin films from atomic layer deposition: a superlattice approach *J. Phys. Chem.* C **121** 16911–20

[74] Lu H A, Wills L A and Wessels B 1994 Electrical properties and poling of $BaTiO_3$ thin films *Appl. Phys. Lett.* **64** 2973

[75] Iijima K, Terashima T, Yamamoto K, Hirata K and Bando Y 1990 Preparation of ferroelectric $BaTiO_3$ thin films by activated reactive evaporation *Appl. Phys. Lett.* **56** 527–9

[76] Bakken K, Blichfeld A, Chernyshov D, Grande T, Glaum J and Einarsrud M 2020 Mechanisms for texture in $BaTiO_3$ thin films from aqueous chemical solution deposition *J. Sol-Gel Sci. Technol.* **95** 562–72

[77] Thery V, Bayart A, Blach J F, Roussel P and Saitzek S 2015 Effective piezoelectric coefficient measurement of $BaTiO_3$ thin films using the x-ray diffraction technique under electric field available in a standard laboratory *Appl. Surf. Sci.* **351** 480–6

[78] Chinchamalatpure V, Ghosh S and Chaudhari G 2010 Synthesis and electrical characterization of $BaTiO_3$ thin films on Si(100) *Mater. Sci. Applic.* **1** 187–90

[79] Hayashi T, Oji N and Maiwa H 1994 Film thickness dependence of dielectric properties of $BaTiO_3$ thin films prepared by sol-gel method *Jap. J. Appl. Phys.* **33** 5277–80

[80] Park K, Xu S, Liu Y, Hwang G, Kang S, Wang Z and Lee K 2010 Piezoelectric $BaTiO_3$ thin film nanogenerator on plastic substrates *Nano Lett.* **10** 4939–43

[81] Guo Y P, Suzuki K, Nishizawa K, Miki T and Kato K 2005 Dielectric and piezoelectric properties of highly (100)-oriented $BaTiO_3$ thin film grown on a $Pt/TiO_x/SiO_2/Si$ substrate using $LaNiO_3$ as a buffer layer *J. Cryst. Growth* **284** 190–6

[82] Ujimoto K, Yoshimura T, Ashida A and Fujimura N 2012 Direct piezoelectric properties of (100) and (111) $BiFeO_3$ epitaxial thin films *Appl. Phys. Lett.* **100** 102901

[83] Yoshimura T, Kariya K, Okamoto N, Aramaki M and Fujimura N 2018 Direct piezoelectric properties of $BiFeO_3$ epitaxial films grown by combinatorial sputtering *J. Phys.: Conf. Ser.* **1052** 012020

[84] Kariya K, Yoshimura T, Murakami S and Fujimura N 2014 Enhancement of piezoelectric properties of (100)-orientated $BiFeO_3$ films on $(100)LaNiO_3/Si$ *Jpn. J. Appl. Phys.* **53** 09PA14

[85] Aramaki M, Yoshimura T, Murakami S, Satoh K and Fujimura N 2019 Demonstration of high-performance piezoelectric MEMS vibration energy harvester using $BiFeO_3$ film with improved electromechanical coupling factor *Sens. Actuators* A **291** 167–73

[86] Dubois M A and Muralt P 1999 Properties of aluminum nitride thin films for piezoelectric transducers and microwave filter applications *Appl. Phys. Lett.* **74** 3032–4

[87] Kurz N, Ding A, Urban D F, Lu Y, Kirste L, Feil N M, Žukauskaitė A and Ambacher O 2019 Experimental determination of the electro-acoustic properties of thin film AlScN using surface acoustic wave resonators *J. Appl. Phys.* **126** 075106

[88] Tsubouchi K, Sugai K and Mikoshiba N 1981 AlN material constants evaluation and SAW properties on AlN/Al_2O_3 and AlN/Si *Ultrasonics Symp.* p 375

[89] Carlotti G and Socino G 1987 Acoustic investigation of the elastic properties of ZnO films *Appl. Phys. Lett.* **51** 1889–91

[90] Kanno I, Mino T, Kuwajima S, Suzuki T, Kotera H and Wasa K 2007 Piezoelectric properties of $(K,Na)NbO_3$ thin films deposited on $(001)SrRuO_3/Pt/MgO$ substrates *IEEE Trans. Ultrason. Ferroelectr. Freq. Control* **54** 2562–6

[91] Shibata K, Oka F, Ohishi A, Mishima T and Kanno I 2008 Piezoelectric properties of $(K,Na)NbO_3$ films deposited by RF magnetron sputtering *Appl. Phys. Express* **1** 011501

[92] Shibata K, Suenaga K, Watanabe K, Horikiri F, Nomoto A and Mishima T 2011 Improvement of piezoelectric properties of $(K,Na)NbO_3$ films deposited by sputtering *Jpn. J. Appl. Phys.* **50** 041503

[93] Kurokawa FYokokawa R, Kotera H, Horikiri F, Shibata K, Mishima T, Sato M and Kanno I 2012 Micro fabrication of lead-free $(K,Na)NbO_3$ piezoelectric thin films by dry etching *Micro Nano Lett.* **7** 1223–5

[94] Dubourdieu C *et al* 2013 Erratum: switching of ferroelectric polarization in epitaxial $BaTiO_3$ films on silicon without a conducting bottom electrode *Nat. Nanotechnol.* **8** 881

[95] Vura S, Jeyaselvan V, Biswas R, Raghunathan V, Selvaraja S and Raghavan S 2021 Epitaxial $BaTiO_3$ on Si(100) with in-plane and out-of-plane polarization using a single TiN transition layer *ACS Appl. Electron. Mater.* **3** 687–95

[96] Wang P and Du H 2015 ZnO thin filmpiezoelectric MEMS vibration energy harvesters with two piezoelectric elements for higher output performance *Rev. Sci. Instrum.* **86** 075002

[97] Marzencki M, Ammar Y and Basrour S 2008 Integrated power harvesting system including a MEMS generator and a power management circuit *Sens. Actuators* A **145-146** 363–70

[98] Elfrink R, Kamel T M, Goedbloed M, Matova S, Hohlfeld D, Van Andel Y and Van Schaijk R 2009 Vibration energy harvesting with aluminum nitride-based piezoelectric devices *J. Micromech. Microeng.* **19** 249–52

[99] Jia Y and Seshia A A 2016 Power optimization by mass tuning for MEMS piezoelectric cantilever vibration energy harvesting *J. Microelectromech. Syst.* **25** 108–17

[100] Alamin Dow A B, Bittner A, Schmid U and Kherani N P 2014 Design, fabrication and testing of a piezoelectric energy microgenerator *Microsyst. Technol.* **20** 1035–40

[101] Andosca R, McDonald T G, Genova V, Rosenberg S, Keating J, Benedixen C and Wu J 0212 Experimental and theoretical studies on MEMS piezoelectric vibrational energy harvesters with mass loading *Sens. Actuators* A **178** 76–87

[102] Jackson N, O'Keeffee R, Waldron F, O'Neill M and Mathewson A 2014 Evaluation of low-acceleration MEMS piezoelectric energy harvesting devices *Microsyst. Technol.* **20** 671–80

[103] Cao Z, Zhang J and Kuwano H 2012 Design and characterization of miniature piezoelectric generators with low resonant frequency *Sens. Actuators* A **179** 178–84

[104] Matloub R, Hadad M, Mazzalai A, Chidambaram N, Moulard G, Sandu C S, Metzger T and Muralt P 2013 Piezoelectric $Al_{1-x}Sc_xN$ thin films: a semiconductor compatible olution for mechanical energy harvesting and sensors *Appl. Phys. Lett.* **102** 10–13

[105] Akiyama M, Umeda K, Honda A and Nagase T 2013 Influence of scandium concentration on power generation figure of merit of scandium aluminum nitride thin films *Appl. Phys. Lett.* **102** 021915

[106] Mayrhofer P M, Rehlendt C, Fischeneder M, Kucera M, Wistrela E, Bittner A and Schmid U 2017 ScAlN MEMS cantilevers for vibrational energy harvesting purposes *J. Microelectromech. Syst.* **26** 102–12

[107] Barth S, Bartzsch H, Gloess D, Frach P, Herzog T, Walter S and Heuer H 2014 Sputter deposition of stress-controlled piezoelectric AlN and AlScN films for ultrasonic and energy harvesting applications *IEEE Trans. Ultrason. Ferroelectr. Freq. Control* **61** 1329–34

[108] Minh L V, Hara M, Yokoyama T, Nishihara T, Ueda M and Kuwano H 2015 Highly piezoelectric MgZr co-doped aluminum nitride-based vibrational energy harvesters *IEEE Trans. Ultrason. Ferroelectr. Freq. Control* **62** 2005–8

[109] Joly A 1877 Recherches sur les composés du nobium et du tantale *Ann. Sci. Éc. Norm. Supér.* **6** 6125–86 (available at: www.numdam.org/article/ASENS_1877_2_6__125_0.pdf)

[110] Matthias B T 1949 New ferroelectric crystals *Phys. Rev.* **75** 1771

[111] Matthias B T and Remeika J P 1951 Dielectric properties of sodium and potassium niobates *Phys. Rev.* **82** 727–9

[112] Shirane G, Danner H, Pavlovic A and Pepinsky R 1954 Phase transitions in ferroelectric $KNbO_3$ *Phys. Rev.* **93** 672–3

[113] Hurst J J and Linz A 1971 Crystal growth and neutron characterization of potassium niobate *Mater. Res. Bull.* **6** 163–8

[114] Fukuda T, Uematsu Y and Ito T 1974 Kyropoulos growth and perfection of $KNbO_3$ single crystal *J. Cryst. Growth* **24–25** 450–3

[115] Xing W, Looser H, Wüest H and Arend H 1986 Progress in $KNbO_3$ crystal growth *J. Cryst. Growth* **78** 431–7

[116] Yamanouchi K, Wagatsuma Y, Odagawa H and Cho Y 2001 Single crystal growth of $KNbO_3$ and application to surface acoustic wave devices *J. Eur. Ceram. Soc.* **21** 2791–5

[117] Reisman A and Holtzberg F 1955 Phase equilibria in the system K_2CO_3-Nb_2O_5 by the method of differential thermal analysis *J. Am. Chem. Soc.* **77** 2115–9

[118] Liang L, Li Y L, Hu S Y, Chen L Q and Lu G H 2010 Piezoelectric anisotropy of a $KNbO_3$ single crystal *J. Appl. Phys.* **108** 094111

[119] Rouffaud R, Marchet P, Hladky-Hennion A C, Bantignies CPham-Thi M and Levassort F 2014 Complete electroelastic set for the (YXt)-45° cut of a $KNbO_3$ single crystal *J. Appl. Phys.* **116** 194106

[120] Chow A F, Lichtenwalner D J, Woolcott J R R, Graettinger T M, Auciello O and Kingon A I 1994 Epitaxial $KNbO_3$ thin films on $KTaO_3$, $MgAl_2O_4$ and MgO substrates *Appl. Phys. Lett.* **65** 1073–5

[121] Lee T H, Hwang H G, Jang S, Wang G, Han S, Kim D H, Kang C Y and Nahm S 2017 Low-temperature-grown $KNbO_3$ thin films and their application to piezoelectric nanogenerators and self-powered ReRAM device *ACS Appl. Mater. Interfaces* **9** 43220–9

[122] Rousseau A, Laur V, Guilloux-Viry M, Tanné G, Huret F, Députier S, Perrin A, Lalu F and Laurent P 2006 Pulsed laser deposited $KNbO_3$ thin films for applications in high frequency range *Thin Solid Films* **515** 2353–60

[123] Odagawa H, Kotani K, Cho Y and Yamanouchi K 1999 Observation of ferroelectric polarization in $KNbO_3$ thin films and surface acoustic wave properties *Jpn. J. Appl. Phys.* **38** 3275–8

[124] Kakimoto K, Hibino T, Masuda I and Ohsato H 2005 Development of transparent single-crystalline $KNbO_3$ thin film by LPE technique *Sci. Technol. Adv. Mater.* **6** 61–65

[125] Swartz S L, Melling P J and Grant C S 1989 Ferroelectric thin films by sol-gel processing *MRS Proc.* **152** 227

[126] Zaldo C, Gill D S, Eason R W, Mendiola J and Chandler P J 1994 Growth of $KNbO_3$ thin films on MgO by pulsed laser deposition *Appl. Phys. Lett.* **65** 502–4

[127] Martín M J, Alfonso J E, Mendiola J, Zaldo C, Gill D S, Eason R W and Chandler P J 1997 Pulsed laser deposition of $KNbO_3$ thin films *J. Mater. Res.* **12** 2699–706

[128] Romanov M V, Korsakov I E, Kaul A R, Stefanovich S Y, Bolshakov I A and Wahl G 2004 MOCVD of $KNbO_3$ ferroelectric films and their characterization *Chem. Vap. Depos.* **10** 318–24

[129] Van Minh L, Hara M and Kuwano H 2014 High performance nonlinear micro energy harvester integrated with (K, Na)NbO_3/Si composite quad-cantilever *IEEE 27th Int. Conf. on Micro Electro Mechanical Systems*

[130] Nystrom M J, Wessels B W, Studebaker D B, Marks T J, Lin W P and Wong G K 1995 Epitaxial potassium niobate thin films prepared by metalorganic chemical vapor deposition *Appl. Phys. Lett.* **67** 365–7

[131] Christen H M, Boatner L A, Budai J D, Chisholm M F, Géa L A, Marrero P J and Norton D P 1996 The growth and properties of epitaxial $KNbO_3$ thin films and $KNbO_3$/$KTaO_3$ superlattices *Appl. Phys. Lett.* **68** 1488–90

[132] Yang R, Shen S Y, Wang C B, Shen Q and Zhang L M 2008 Pulsed laser deposition of stoichiometric $KNbO_3$ films on Si (100) *Thin Solid Films* **516** 8559–63

[133] Suzuki H, Ohno T, Miyazaki H, Fu D S, Ishikawa K and Kodaira K 2001 Orientation control of $KNbO_3$ thin film on silicon wafer with chemical solution deposition *Key Eng. Mater.* **206–213** 1493–6

[134] Wu J, Xiao D and Zhu J 2015 Potassium–sodium niobate lead-free piezoelectric materials: past, present, and future of phase boundaries *Chem. Rev.* **115** 2559–95

[135] Shirane G, Newnham R and Pepinsky R 1954 Dielectric properties and phase transitions of $NaNbO_3$ and (Na,K)NbO_3 *Phys. Rev.* **96** 581–8

[136] Jiang M *et al* 2019 Ultrahigh piezoelectric coefficient of a lead-free $K_{0.5}Na_{0.5}NbO_3$-based single crystal fabricated by a simple seed-free solid-state growth method *J. Mater. Chem.* C **7** 14845–54

[137] Gupta S and Priya S 2011 Ferroelectric properties and dynamic scaling of ⟨100⟩ oriented $(K_{0.5}Na_{0.5})NbO_3$ single crystals *Appl. Phys. Lett.* **98** 242906

[138] Lin D, Li Z, Xu Z and Yao X 2009 Characterization of KNN single crystals by slow-cooling technique *Ferroelectrics* **381** 1–8

[139] Seog H J, Ullah A, Ahn C W, Kim I W, Lee S Y, Park J, Lee H J, Won S S and Kim S H 2018 Recent progress in potassium sodium niobate lead-free thin films *J. Korean Phys. Soc.* **72** 1467–83

[140] Cho C R and Grishin A 2000 Background oxygen effects on pulsed laser deposited $Na_{0.5}K_{0.5}NbO_3$ films: from superparaelectric state to ferroelectricity *J. Appl. Phys.* **87** 4439–48

[141] Kugler V M, Söderlind F, Music D, Helmersson U, Andreasson J and Lindbäck T 2004 Microstructure/dielectric property relationship of low temperature synthesised (Na,K)NbO_x thin films *J. Cryst. Growth* **262** 322–6

[142] Schroeter C, Wessler B and Eng L M 2007 High throughput method for $K_{0.5}Na_{0.5}NbO_3$ thin films preparation by chemical solution deposition *J. Eur. Ceram. Soc.* **27** 3785–8

[143] Kugler V M, Söderlind F, Music D, Helmersson U, Andreasson J and Lindbäck T 2003 Low temperature growth and characterization of (Na,K)NbO_x thin films *J. Cryst. Growth* **254** 400–4

[144] Triebwasser S 1959 Study of ferroelectric transitions of solid-solution single crystals of $KNbO_3$-$KTaO_3$ *Phys. Rev.* **114** 63

[145] Bartasyte A, Kreisel J, Peng W and Guilloux-Viry M 2010 Temperature-dependent Raman scattering of $KTa_{1-x}Nb_xO_3$ thin films *Appl. Phys. Lett.* **96** 262903

[146] Meng X, Tian H, Hu C, Yang J, Li L, Yang B and Zhou Z 2019 Elastic, piezoelectric, and dielectric properties of high-quality $KTa_{0.53}Nb_{0.47}O3$ single crystal with tetragonal phase *J. Alloys Compd.* **773** 21–26

[147] Kallur V A and Pandey R K 1994 Crystal growth and properties of potassium tantalate niobate, KTa_{1-x} Nb_xO_3 ferroelectric *Ferroelectrics* **158** 55–60

[148] NTT Science and Core Technology Successful preparation of KTN crystals with the highest reported electro-optic effect and the potential for providing a great improvement in optical device performance (available at: www.ntt-review.jp/archive/ntttechnical.php?contents=ntr200312056.pdf)

[149] Hulliger J, Gutmann R and Wa¨gli P 1989 Growth of monocrystalline thin films of potassium-tantalate-niobate (KTN) by liquid-phase epitaxy *Thin Solid Films* **175** 201–6

[150] Sashital S R, Krishnakumar S and Esener S 1993 Synthesis and characterization of rf-planar magnetron

sputtered $KTa_xNb_{1-x}O_3$ thin films *Appl. Phys. Lett.* **62** 2917–9
[151] Fernandez F E, Pumarol M, Marrero P, Rodriguez E and Mourad H A 1997 Study of KTN thin films of variable composition grown by pulsed laser deposition *MRS Proc.* **493** 365
[152] Rousseau A, Guilloux-Viry M, Dogheche E, Bensalah M and Remiens D 2007 Growth and optical properties of $KTa_{1-x}Nb_xO_3$ thin films grown by pulsed laser deposition on MgO substrates *J. Appl. Phys.* **102** 093106
[153] Laur V, Moussavou A, Rousseau A, Tanne G, Laurent P, Bouquet V, Guilloux-Viry M and Huret F 2006 KTN ferroelectric thin-films: application to the realization of tunable microwave devices *European Microwave Conf.* pp 835–8
[154] Jia Y, Winkler M, Cheng C, Feng C, Kirste L, Cimalla V, Žukauskaitė A, Szabados J, Breunig I and Buse K 2018 Pulsed laser deposition of ferroelectric potassium tantalate-niobate optical waveguiding thin films *Opt. Mater. Express* **8** 541
[155] Kanno I, Ichida T, Adachi K, Kotera H, Shibata K and Mishima T 2012 Powergeneration performance of lead-free (K,Na)NbO_3 piezoelectric thin-film energy harvesters *Sens. Actuators* A **179** 132–6
[156] Shiraishi T, Kaneko N, Kurosawa M, Uchida H, Suzuki Y, Kobayashi T and Funakubo H 2015 Vibration-energy-harvesting properties of hydrothermally synthesized (K,Na)NbO_3 films deposited on flexible metal foil substrates *Jpn. J. Appl. Phys.* **54** 10ND06
[157] Won S S, Lee J, Venugopal V, Kim D J, Lee J, Kim I W, Kingon A I and Kim S H 2016 Lead-free Mn-doped $(K_{0.5},Na_{0.5})NbO_3$ piezoelectric thin films for MEMS based vibrational energy harvester applications *Appl. Phys. Lett.* **108** 0–5
[158] Bartasyte A, Margueron S, Baron T, Oliveri S and Boulet P 2017 Toward high-quality epitaxial $LiNbO_3$ and $LiTaO_3$ thin films for acoustic and optical applications *Adv. Mater. Interfaces* **4** 1–36
[159] Baba A, Searfass C T and Tittmann B R 2010 High temperature ultrasonic transducer up to 1000 °C using lithium niobate single crystal *Appl. Phys. Lett.* **97** 232901
[160] Le Boulbar E D and Bowen C R 2015 Study of Y-cut $LiNbO_3$ (010) crystal under oscillated vibration at high temperature for energy harvesting in hostile environment *Joint IEEE ISAF/ISIF/PFM Proc.* p 292
[161] Cochard C, Spielmann T, Bahlawane N, Halpin A and Granzow T 2017 Broadband characterization of congruent lithium niobate from mHz to optical frequencies *J. Phys. D: Appl. Phys.* **50** 36LT01
[162] Bartasyte A, Plausinaitiene V, Abrutis A, Murauskas T, Boulet P, Margueron S, Gleize J, Robert S, Kubilius V and Saltyte Z 2012 Residual stress and clamped thermal expansion in $LiNbO_3$ and $LiTaO_3$ thin films *Appl. Phys. Lett.* **101** 122902
[163] Verma A, Panayanthatta N, Ichangi A, Fischer T, Montes L, Bano E and Mathur S 2021 Interdependence of piezoelectric coefficient and film thickness in $LiTaO_3$ cantilevers *J. Am. Ceram. Soc.* **104** 1966–77
[164] Bartasyte A, Kuprenaite S and Astié V 2020 Layered solid state element comprising a ferroelectric layer and method for manufacturing the same *Patent* WO2021244978A1 (https://doi.org/10.1039/c9dt04732h)
[165] Bartasyte A, Margueron S, Gauthier-Manuel L, Clementi G, Ouhabaz M and Bassignot F 2020 Dispositif piézo-électrique comprenant des films piézo-électriques $LiNbO_3$ et/ou $LiTaO_3$ monocristallins flexibles intégrés sur un substrat flexible et procédés de fabrication associés *Patent* EP3989299A1
[166] Funasaka T, Furuhata M, Hashimoto Y and Nakamura K 1998 Piezoelectric generator using a $LiNbO_3$ platewith an inverted domain *Proc. IEEEUltrasonics Symp.* vol 1 pp 959–62
[167] Bedekar V, Oliver J, Zhang S and Priya S 2009 Comparative study of energy harvesting from high temperature piezoelectric single crystals *Jpn. J. Appl. Phys.* **48** 0914061–5
[168] Morita T, Niino T, Asama H and Tashiro H 2001 Fundamental study of a stacked lithium niobate transducer *Jpn. J. Appl. Phys.* **40** 3801–6
[169] Kawamata A, Hosaka H and Morita T 2007 Non-hysteresis and perfect linear piezoelectric performance of a multilayered lithium niobate actuator *Sens. Actuators* A **135** 782–6
[170] Panayanthatta N *et al* 2021 A self-powered and battery-free vibrational energy to time converter for wireless vibration monitoring *Sensors* **21** 7503
[171] Machado L Q, Yurchenko D, Wang J, Clementi G, Margueron S and Bartasyte A 2021 Multi-dimensional constrained energy optimization of a piezoelectric harvester for E-gadgets *Iscience* **24** 102749
[172] Barrientos G, Clementi G, Trigona C, Ouhabaz M, Gauthier-Manuel L, Belharet D, Margueron S, Bartasyte A, Malandrino G and Baglio S 2022 Lead-free $LiNbO_3$ thick film MEMS kinetic cantilever beam sensor/energy harvester *Sensors* **22** 559
[173] Kubel F and Schmid H 1993 Growth, twinning and etch figures of ferroelectric/ferroelastic dendritic $BiFeO_3$ single domain crystals *J. Cryst. Growth* **129** 515–24
[174] Martí X, Ferrer P, Herrero-Albillos J, Narvaez J, Holy V, Barrett N, Alexe M and Catalan G 2011 Skin layer of $BiFeO_3$ single crystals *Phys. Rev. Lett.* **106** 236101
[175] Lu J, Qiao L, Fu P and Wu Y 2011 Phase equilibrium of Bi_2O_3–Fe_2O_3 pseudo-binary system and growth of $BiFeO_3$ single crystal *J. Cryst. Growth* **318** 936–41
[176] Haumont R, Saint-Martin R and Byl C 2021 Centimeter-size $BiFeO_3$ single crystals grown by flux method *Phase Transit.* **81** 881–8
[177] Ito T, Ushiyama T, Yanagisawa Y, Kumai R and Tomioka Y 2011 Growth of highly insulating bulk single crystals of multiferroic $BiFeO_3$ and their inherent internal strains in the domain-switching process *Cryst. Growth Des.* **11** 5139–43
[178] Białek M, Ito T, Rønnow H and Ansermet J 2019 Terahertz-optical properties of a bismuth ferrite single crystal *Phys. Rev.* B **99** 064429
[179] Yang X *et al* 2018 Single-crystal $BiFeO_3$ nanoplates with robust antiferromagnetism *ACS Appl. Mater. Interfaces* **10** 5785–92
[180] Catalano M, Spedalotto G, Condorelli G and Malandrino G 2017 MOCVD growth of perovskite multiferroic $BiFeO_3$ films: the effect of doping at the A and/or B sites on the structural, morphological and ferroelectric properties *Adv. Mater. Interfaces* **4** 1601025
[181] Micard Q, Pellegrino A L, Lo Nigro R, Bartasyte A, Condorelli G G and Malandrino G 2020 Piezoelectric Ba and Ti co-doped $BiFeO_3$ textured films: selective growth of solid solutions or nanocomposites *J. Mater. Chem.* C **8** 16168–79
[182] Kan D, Pálová L, Anbusathaiah V, Cheng C, Fujino S, Nagarajan V, Rabe K and Takeuchi I 2010 Universal behavior and electric-field-induced structural transition in rare-earth-substituted $BiFeO_3$ *Adv. Funct. Mater.* **20** 1108–15
[183] Radojković A, Golić D, Ćirković J, Stanojević Z, Pajić D, Torić F, Dapčević A, Vulić P, Branković Z and Branković G 2018 Tuning of $BiFeO_3$ multiferroic

properties by light doping with Nb *Ceram. Int.* **44** 16739–44
[184] Tu C, Chen P, Chen C, Lin C and Schmidt V 2018 Tailoring microstructure and photovoltaic effect in multiferroic Nd-substituted $BiFeO_3$ ceramics by processing atmosphere modification *J. Eur. Ceram. Soc.* **38** 1389–98
[185] Yuan X, Shi L, Zhao J, Zhou S, Guo J, Pan S, Miao X and Wu L 2018 Tuning ferroelectric, dielectric, and magnetic properties of $BiFeO_3$ ceramics by Ca and Pb Co-doping *Phys. Status Solidi* b **256** 1800499
[186] Zhang Y, Zheng H, Wang X, Li H, Wu Y, Zhang Y, Su H and Yuan G 2020 Enhanced photovoltaic properties of gradient calcium-doped $BiFeO_3$ films *Ceram. Int.* **46** 10083–8
[187] Zheng T and Wu J 2020 Perovskite $BiFeO_3$–$BaTiO_3$ ferroelectrics: engineering properties by domain evolution and thermal depolarization modification *Adv. Electron. Mater.* **6** 2000079
[188] Tie Y, Ma S, Pei S, Zhang Q, Zhu K, Zhang R, Xu X, Han T and Liu W 2020 Pr doped $BiFeO_3$ hollow nanofibers via electrospinning method as a formaldehyde sensor *Sens. Actuators* B **308** 127689
[189] Zhu H, Sun X, Kang L, Hong M, Liu M, Yu Z and Ouyang J 2016 Charge transport behaviors in epitaxial $BiFeO_3$ thick films sputtered with different Ar/O_2 flow ratios *Scr. Mater.* **115** 62–65
[190] Hohenberger S, Jochum J, Van Bael M, Temst K, Patzig C, Höche T, Grundmann M and Lorenz M 2020 Enhanced magnetoelectric coupling in $BaTiO_3$-$BiFeO_3$ multilayers—an interface effect *Materials* **13** 197
[191] Lorenz M, Hirsch D, Patzig C, Höche T, Hohenberger S, Hochmuth H, Lazenka V, Temst K and Grundmann M 2017 Correlation of interface impurities and chemical gradients with high magnetoelectric coupling strength in multiferroic $BiFeO_3$–$BaTiO_3$ superlattices *ACS Appl. Mater. Interfaces* **9** 18956–65
[192] Lorenz M, Wagner G, Lazenka V, Schwinkendorf P, Modarresi H, Van Bael M, Vantomme A, Temst K, Oeckler O and Grundmann M 2015 Correlation of magnetoelectric coupling in multiferroic $BaTiO_3$-$BiFeO_3$ superlattices with oxygen vacancies and antiphase octahedral rotations *Appl. Phys. Lett.* **106** 012905
[193] Jin C *et al* 2020 Tuning ferroelectricity and ferromagnetism in $BiFeO_3$/$BiMnO_3$ superlattices *Nanoscale* **12** 9810–6
[194] Yang H, Jin C, Mi W, Bai H and Chen G 2012 Electronic and magnetic structure of Fe_3O_4/$BiFeO_3$ multiferroic superlattices: first principles calculations *J. Appl. Phys.* **112** 063925
[195] Feng N, Mi W, Wang X, Cheng Y and Schwingenschlögl U 2015 Superior properties of energetically stable $La_{2/3}Sr_{1/3}MnO_3$/Tetragonal $BiFeO_3$ multiferroic superlattices *ACS Appl. Mater. Interfaces* **7** 10612–6
[196] Das S, Sahoo R and Nath T 2020 Investigation of room temperature multiferroic properties in sol-gel derived gadolinium, cobalt doped $BiFeO_3$ nanoceramics *J. Appl. Phys.* **127** 054101
[197] Yang H, Zhou C, Liu X, Zhou Q, Chen G, Li W and Wang H 2013 Piezoelectric properties and temperature stabilities of Mn- and Cu-modified $BiFeO_3$–$BaTiO_3$ high temperature ceramics *J. Eur. Ceram. Soc.* **33** 1177–83
[198] Leontsev S and Eitel R 2009 Dielectric and piezoelectric properties in Mn-modified (1-x)$BiFeO_3$-x$BaTiO_3$ ceramics *J. Am. Cer. Soc.* **92** 2957–61
[199] Zuo R, Ye C and Fang X 2008 $Na_{0.5}K_{0.5}NbO_3$–$BiFeO_3$ lead-free piezoelectric ceramics *J. Phys. Chem. Solids* **69** 230–5
[200] Kang F, Zhang L, Huang B, Mao P, Wang Z, Sun Q, Wang J and Hu D 2020 Enhanced electromechanical properties of $SrTiO_3$-$BiFeO_3$-$BaTiO_3$ ceramics via relaxor behavior and phase boundary design *J. Eur. Ceram. Soc.* **40** 1198–204
[201] Auromun K, Hajra S, Choudhary R and Behera B 2020 Structural, dielectric and electrical characteristics of yttrium modified $0.7BiFeO_3$-$0.3PbTiO_3$ *Solid State Sci.* **101** 106139
[202] Wang J, Zhou C, Li Q, Yang L, Xu J, Chen G, Yuan C and Rao G 2018 Simultaneously enhanced piezoelectric properties and depolarization temperature in calcium doped $BiFeO_3$-$BaTiO_3$ ceramics *J. Alloys Compd.* **748** 758–65
[203] Akram F, Kim J, Khan S, Zeb A, Yeo H, Sung Y, Song T, Kim M and Lee S 2020 Less temperature-dependent high dielectric and energy-storage properties of eco-friendly $BiFeO_3$–$BaTiO_3$-based ceramics *J. Alloys Compd.* **818** 152878
[204] Malik R, Zaman A, Hussain A, Maqbool A, Song T, Kim W, Sung Y and Kim M 2018 Temperature invariant high dielectric properties over the range 200 °C–500 °C in $BiFeO_3$ based ceramics *J. Eur. Ceram. Soc.* **38** 2259–63
[205] Zhou C, Feteira A, Shan X, Yang H, Zhou Q, Cheng J, Li W and Wang H 2012 Remarkably high-temperature stable piezoelectric properties of $Bi(Mg_{0.5}Ti_{0.5})O_3$ modified $BiFeO_3$–$BaTiO_3$ ceramics *Appl. Phys. Lett.* **101** 032901
[206] Shao F *et al* 2020 Activation energy mediated band structure in strained multiferroic $BiFeO_3$ thin films *Ceram. Int.* **46** 6838–46
[207] Palkar V, John J and Pinto R 2002 Observation of saturated polarization and dielectric anomaly in magnetoelectric $BiFeO_3$ thin films *Appl. Phys. Lett.* **80** 1628–30
[208] Wang H, Khatkhatay F, Jian J, Huang J, Fan M and Wang H 2019 Strain tuning of ferroelectric and optical properties of rhombohedral-like $BiFeO_3$ thin films on $SrRuO_3$-buffered substrates *Mater. Res. Bull.* **110** 120–5
[209] Daumont C, Farokhipoor S, Ferri A, Wojdeł J, Íñiguez J, Kooi B and Noheda B 2010 Tuning the atomic and domain structure of epitaxial films of multiferroic $BiFeO_3$ *Phys. Rev.* B **81** 144115
[210] Saj Mohan M, Bandyopadhyay S, Jogi T, Bhattacharya S and Ramadurai R 2019 Realization of rhombohedral, mixed, and tetragonal like phases of $BiFeO_3$ and ferroelectric domain engineering using a strain tuning layer on $LaAlO_3$(001) substrate *J. Appl. Phys.* **125** 012501
[211] Amrillah T *et al* 2016 Tuning the magnetic properties of self-assembled $BiFeO_3$–$CoFe_2O_4$ heteroepitaxy by magneto-structural coupling *Nanoscale* **8** 8847–54
[212] Yao Y, Zhang B, Chen L, Yang Y, Wang Z, Alshareef H and Zhang X 2012 Polarization-tuned diode behaviour in multiferroic $BiFeO_3$ thin films *J. Phys. D: Appl. Phys.* **46** 055304
[213] Katiyar R, Misra P, Morell G and Katiyar R 2014 Effect of poling on photovoltaic properties in highly oriented $BiFeO_3$ thin films *Integr. Ferroelectr.* **157** 168–73
[214] Biswas P, Thirmal C, Pal S, Miryala M, Murakami M and Murugavel P 2019 The composition and poling-dependent photovoltaic studies in ferroelectric $(Bi_{1-x}Sr_x)(Fe_{1-x}Ti_x)O_3$ thin films *J. Mater. Sci., Mater. Electron.* **31** 1515–23
[215] Biswas P, Pal S, Subramanian V and Murugavel P 2020 Polarization driven self-biased and enhanced UV–visible photodetector characteristics of ferroelectric thin film *J. Phys. D: Appl. Phys.* **53** 275302
[216] Micard Q, Margueron S, Bartasyte A, Condorelli G G and Malandrino G 2022 Dy-doped $BiFeO_3$ thin films: piezoelectric and bandgap tuning *Mater. Adv.* **3** 3446–56
[217] Micard Q, Clementi G, Bartasyte A, Muralt P, Condorelli G G and Malandrino G 2022 Self-poled

heteroepitaxial $Bi_{(1-x)}Dy_xFeO_3$ films with promising pyroelectric properties *Adv. Mater. Interfaces* **9** 2101539
[218] Yang T, Wang C, Zhang X, Feng Y, Guo H, Jin K, Gao X, Li Z and Li X 2014 Surface double-layer structure in (110) oriented $BiFeO_3$ thin film *Appl. Phys. Lett.* **105** 202901
[219] Nechache R, Harnagea C, Gunawan L, Carignan L, Maunders C, Menard D, Botton G and Pignolet A 2007 Growth, structure, and properties of $BiFeO_3$-$BiCrO_3$ films obtained by dual cross beam PLD *IEEE Trans. Ultrason. Ferroelectr. Freq. Control* **54** 2645–52
[220] Chen C, Her J and Pan T 2020 Structural and electrical properties of the sol-gel derived multiferroic $BiFeO_3$ monolayer and $NiTiO_3$-$BiFeO_3$ bilayer thin films *Ceram. Int.* **46** 13219–24
[221] Campanini M, Gradauskaite E, Trassin M, Yi D, Yu P, Ramesh R, Erni R and Rossell M 2020 Imaging and quantification of charged domain walls in $BiFeO_3$ *Nanoscale* **12** 9186–93
[222] Chen D *et al* 2017 A strain-driven antiferroelectric-to-ferroelectric phase transition in La-doped $BiFeO_3$ thin films on Si *Nano Lett.* **17** 5823–9
[223] Wu J and Wang J 2010 $BiFeO_3$ thin films of (111)-orientation deposited on $SrRuO_3$ buffered $Pt/TiO_2/SiO_2/Si(100)$ substrates *Acta Mater.* **58** 1688–97
[224] Liu Y, Qi Y, Zhou P, Guan C, Chen H, Wang J, Ma Z, Zhang T and Liu Y 2017 Mechanisms of resistive switching in $BiFeO_3$ thin films modulated by bottom electrode *J. Phys. D: Appl. Phys.* **51** 025303
[225] Xu S, Zhang Y, Guo H, Geng W, Bai Z and Jiang A 2017 Improved polarization retention of $BiFeO_3$ thin films using $GdScO_3$ (110) substrates *Chin. Phys. Lett.* **34** 027701
[226] Scillato D, Licciardello N, Catalano M, Condorelli G, Lo Nigro R and Malandrino G 2011 $BiFeO_3$ films doped in the A or B sites: effects on the structural and morphological properties *J. Nanosci. Nanotechnol.* **11** 8221–5
[227] Annapu Reddy V, Pathak N and Nath R 2013 Enhanced magnetoelectric coupling in transition-metal-doped $BiFeO_3$ thin films *Solid State Commun.* **171** 40–45
[228] Yao X *et al* 2019 Growth and physical properties of $BiFeO_3$ thin films directly on Si substrate *J. Cryst. Growth* **522** 110–6
[229] Zhang W, Wu H, Zhang X, Zhu H and Hu F 2019 Growth of (001) preferentially oriented $BiFeO_3$ films on Si substrate by sol-gel method *Mater. Res. Express* **6** 106420
[230] Wang X, Liu H and Yan B 2009 Enhanced ferroelectric properties of Ce-substituted $BiFeO_3$ thin films on $LaNiO_3$/Si substrates prepared by sol–gel process *J. Eur. Ceram. Soc.* **29** 1183–7
[231] Chen X, Wu G, Zhang H, Qin N, Wang T, Wang F, Shi W and Bao D 2010 Nonvolatile bipolar resistance switching effects in multiferroic $BiFeO_3$ thin films on $LaNiO_3$-electrodized Si substrates *Appl. Phys.* A **100** 987–90
[232] Kumari C, Varun I, Prakash Tiwari S and Dixit A 2018 Robust non-volatile bipolar resistive switching in sol-gel derived $BiFeO_3$ thin films *Superlattices Microstruct.* **120** 67–74
[233] Lu Z, Yang X, Jin C, Li P, Wan J and Liu J 2018 Nonvolatile electric-optical memory controlled by conductive filaments in Ti-doped $BiFeO_3$ *Adv. Electron. Mater.* **4** 1700551
[234] Liu J, Deng H, Cao H, Zhai X, Tao J, Sun L, Yang P and Chu J 2014 Influence of rare-earth elements doping on structure and optical properties of $BiFeO_3$ thin films fabricated by pulsed laser deposition *Appl. Surf. Sci.* **307** 543–7
[235] Micard Q, Condorelli G and Malandrino G 2020 Piezoelectric $BiFeO_3$ thin films: optimization of MOCVD process on Si *Nanomaterials* **10** 630
[236] Anlin Golda R, Marikani A and John Alex E 2020 Enhancement of dielectric, ferromagnetic and electrochemical properties of $BiFeO_3$ nanostructured films through rare earth metal doping *Ceram. Int.* **46** 1962–73
[237] Yun K, Ricinschi D, Kanashima T, Noda M and Okuyama M 2004 Giant ferroelectric polarization beyond 150 μC/cm2in $BiFeO_3$ thin film *Jpn. J. Appl. Phys.* **43** L647–8
[238] Xiao S, Sun H, Liu X and Sui H 2020 Investigations on photovoltaic performance of sol–gel derived $BiFeO_3$-based heterostructures via compositional modification *Mater. Lett.* **260** 126964
[239] Yakovlev S, Zekonyte J, Solterbeck C and Es-Souni M 2005 Interfacial effects on the electrical properties of multiferroic $BiFeO_3$/Pt/Si thin film heterostructures *Thin Solid Films* **493** 24–29
[240] Bouquet V, Baudouin F, Demange V, Députier S, Ollivier S, Joanny L, Rault L, Fouchet A and Guilloux-Viry M 2020 Influence of two-dimensional oxide nanosheets seed layers on the growth of (100)$BiFeO_3$ thin films synthesized by chemical solution deposition *Thin Solid Films* **693** 137687
[241] Yan L, Zhuo M, Wang Z, Yao J, Haberkorn N, Zhang S, Civale L, Li J, Viehland D and Jia Q 2012 Magnetoelectric properties of flexible $BiFeO_3$/Ni tapes *Appl. Phys. Lett.* **101** 012908
[242] Khomyakova E, Pavlic J, Makarovic M, Ursic H, Walker J, Shur V, Rojac T, Malic B and Bencan A 2016 Screen-printed $BiFeO_3$ thick films on noble metal foils *Ferroelectrics* **496** 196–203
[243] Yoshimura T, Murakami S, Wakazono K, Kariya K and Fujimura N 2013 Piezoelectric vibrational energy harvester using lead-free ferroelectric $BiFeO_3$ films *Appl. Phys. Express* 6 051501
[244] Wang N, Luo X, Han L, Zhang Z, Zhang R, Olin H and Yang Y 2020 Structure, performance, and application of $BiFeO_3$ nanomaterials *Nano-Micro Lett.* **12** 81
[245] Aramaki M, Izumi K, Yoshimura T, Murakami S, Satoh K, Kanda K and Fujimura N 2018 Investigation of mechanical nonlinear effect in piezoelectric MEMS vibration energy harvesters *Jpn. J. Appl. Phys.* **57** 1–4
[246] Murakami S, Yoshimura T, Satoh K, Wakazono K, Kariya K and Fujimura N 2013 Development of piezoelectric MEMS vibration energy harvester using (100) oriented $BiFeO_3$ ferroelectric film *J. Phys.: Conf. Ser.* **476** 012007
[247] Dmitriev V, Tolédano P, Torgashev V and Salje E 1998 Theory of reconstructive phase transitions between SiO_2 polymorphs *Phys. Rev.* B **58** 11911–21
[248] Aasly K, Malvik T and Myrhaug E 2007 Advanced methods to characterize thermal properties of quartz *INFACON XI*
[249] Demazeau G, Lafon F, Curtet J and Largeteau A 1994 The hydrothermal crystal growth of quartz: new developments *High Press. Res.* **12** 329–35
[250] Pastero L, Turci F, Leinardi R, Pavan C and Monopoli M 2016 Synthesis of α-quartz with controlled properties for the investigation of the molecular determinants in silica toxicology *Cryst. Growth Des.* **16** 2394–403
[251] Jiang X, Jiang Y B and Brinker C J 2011 Hydrothermal synthesis of monodisperse single-crystalline alpha-quartz nanospheres *Chem. Commun.* **47** 7524–6
[252] *Guides Lumineux Fibre Optique en Quartz | Edmund Optics* (available at: www.edmundoptics.fr/f/quartz-fiber-optic-light-guides/12159/)
[253] *Oscillateurs à quartz | RS Components* (available at: https://fr.rs-online.com/web/c/passifs/quartz-oscillateurs-et-resonateurs/oscillateurs-a-quartz/?applied-dimensions=4294651362)

[254] Bridle H and Desmulliez M 2014 Biosensors for the detection of waterborne pathogens *Waterborne Pathogens* ed H Bridle (Amsterdam: Academic) ch 7, pp 189–229

[255] Castner D G and Ratner B D 2019 Proteins controlled with precision at organic, polymeric, and biopolymer interfaces for tissue engineering and regenerative medicine *Principles of Regenerative Medicine* 3rd edn, ed A A, R Lanza, M A G and R Nerem (Boston: Academic) ch 31, pp 523–34

[256] Krim J, Solina D H and Chiarello R 1991 Nanotribology of a Kr monolayer: a quartz-crystal microbalance study of atomic-scale friction *Phys. Rev. Lett.* **66** 181–4

[257] Voinova M V, Jonson M and Kasemo B 2002 Missing mass effect in biosensor's QCM applications *Biosens. Bioelectron.* **17** 835–41

[258] Fredriksson C, Kihlman S, Rodahl M and Kasemo B 1998 The piezoelectric quartz crystal mass and dissipation sensor: a means of studying cell adhesion *Langmuir* **14** 248–51

[259] Keller C A and Kasemo B 1998 Surface specific kinetics of lipid vesicle adsorption measured with a quartz crystal microbalance *Biophys. J.* **75** 1397–402

[260] Iwasaki F and Iwasaki H 2002 Historical review of quartz crystal growth *J. Cryst. Growth* **237–239** 820–7

[261] Kushibiki J I, Ohtagawa M and Takanaga I 2003 Comparison of acoustic properties between natural and synthetic α-quartz crystals *J. Appl. Phys.* **94** 295–300

[262] Drisko G L, Carretero-Genevrier A, Gich M, Gàzquez J, Ferrah D, Grosso D, Boissière C, Rodriguez-Carvajal J and Sanchez C 2014 Water-induced phase separation forming macrostructured epitaxial quartz films on silicon *Adv. Funct. Mater.* **24** 5494–502

[263] Richet P, Bottinga Y, Denielou L, Petitet J P and Tequi C 1982 Thermodynamic properties of quartz, cristobalite and amorphous SiO_2: drop calorimetry measurements between 1000 and 1800 K and a review from 0 to 2000 K *Geochim. Cosmochim. Acta* **46** 2639–58

[264] Takahashi N, Hoshogi M, Nakumura T, Momose Y, Nonaka S, Yagi H, Sinrikic Y and Tamanukic K 2002 Catalyst-enhanced vapor-phase epitaxy of quartz thin films under atmospheric pressure *J. Mater. Chem.* **12** 719–22

[265] Takahashi N, Majima J, Nakumura T, Nonaka S, Yagi H, Sinrikic Y and Tamanukic K 2003 Growth of a high quality quartz film on sapphire by catalyst-enhanced atmospheric-pressure vapor-phase epitaxy using buffer layers *Chem. Mater.* **15** 2889–91

[266] Takahashi N, Nakumura T, Nonaka S, Kubo Y, Sinriki Y and Tamanuki K 2005 Growth of crystalline quartz films with AT-cut plane by means of catalyst-enhanced vapor-phase epitaxy under atmospheric pressure *J. Phys. Chem. Solids* **66** 1145–9

[267] Carretero-Genevrier A, Gich M, Picas L, Gazquez J, Drisko G L, Boissiere C, Grosso D, Rodriguez-Carvajaland J and Sanchez C 2013 Soft-chemistry-based routes to epitaxial α-quartz thin films with tunable textures *Science* **340** 827–31

[268] Zhang Q, Sánchez-Fuentes D, Gómez A, Desgarceaux R, Charlot B, Gàzquez J, Carretero-Genevrier A and Gich M 2019 Tailoring the crystal growth of quartz on silicon for patterning epitaxial piezoelectric films *Nanoscale Adv.* **1** 3741–52

[269] Zhang Q *et al* 2020 Micro/nanostructure engineering of epitaxial piezoelectric α-quartz thin films on silicon *ACS Appl. Mater. Interfaces* **12** 4732–40

[270] Ohsato H, Iwataki T and Morikoshi H 2012 Mechanism of piezoelectricity for langasite based on the framework crystal structure *Trans. Electr. Electron. Mater.* **13** 51–59

[271] Uda S, Wang S Q, Kimura H and Huang X 2008 Phase equilibria and growth of langasite-type crystals *Crystal Growth Technology: From Fundamentals and Simulation to Large-scale Production* ed H J Scheel and P Capper (Wiley-VCH Verlag GmbH & Co. KGaA) ch 15, pp 380–414

[272] Wulfmeier H, Feder R, Zhao L and Fritze H 2020 High-temperature stable piezoelectric transducers using epitaxially grown electrodes *J. Sens. Sens. Syst.* **9** 15–26

[273] Wulfmeier H, Feder R, Zhao L and Fritze H 2019 Epitaxial piezoelectric langasite thin films for high-temperature application *MRS Adv.* **4** 1–7

[274] Wang S Q and Uda S 2003 Phase relations around langasite ($La_3Ga_5SiO_{14}$) in the system La_2O_3–Ga_2O_3–SiO_2 in air *J. Cryst. Growth* **250** 463–70

[275] Phila Optics Inc. *Saw Langasite wafers* (available at: www.philaoptics.com/WafersSawLangasite.asp)

[276] Moulzolf S, Frankel D, Bernhardt G, Nugent B and Lad R 2011 Thin film electrodes and passivation coatings for harsh environment microwave acoustic sensors *Proc. SPIE—The Int. Society for Optical Engineering* p 8066

[277] Richter D, Sakharov S, Forsén E, Mayer E, Reindl L and Fritze H 2011 Thin film electrodes for high temperature surface acoustic wave devices *Proc. Eng.* **25** 168–71

[278] Behanan R, Moulzolf S C, Call M, Bernhardt G, Frankel D, Lad R J and da Cunha M P 2013 Thin films and techniques for SAW sensor operation above 1000 °C *IEEE Int. Ultrason. Symp.* pp 1013–6

[279] Frankel D, Moulzolf S, da Cunha M P and Lad R 2015 Influence of composition and multilayer architecture on electrical conductivity of high temperature Pt-alloy films *Surf. Coat. Technol.* **284** 215–21

[280] Sakharov S, Zabelin A, Kondratiev S, Richter D, Fritze H, Roshchupkin D, Shvetsov A and Zhgoon S 2012 Optimization of wafer orientation and electrode materials for LGS high-temperature SAW sensors *IEEE Int. Ultrasonics Symp.* pp 1525–8

[281] Zhang H, Singh N B, Berghmans A, Adam J D, Tidrow S and Fazi C 2002 Liquid phase epitaxy growth of langasite film for resonators and oscillators *J. Cryst. Growth* **234** 660–5

[282] Hu Y, Wang F W and Lin H L 2008 Photoluminescence of langasite thin films prepared from sol–gel process *Mater. Chem. Phys.* **107** 82–84

[283] Won S S, Sheldon M, Mostovych N, Kwak J, Chang B S, Ahn C W, Kingon A I, Kim I W and Kim S H 2015 Piezoelectric poly(vinylidene fluoride trifluoroethylene) thin film-based power generators using paper substrates for wearable device applications *Appl. Phys. Lett.* **107** 202901

[284] Sriramdas R, Chiplunkar S, Cuduvally R M and Pratap R 2015 Performance enhancement of piezoelectric energy harvesters using multilayer and multistep beam configurations *IEEE Sens. J.* **15** 3338–48

[285] Yeo H G, Xue T, Roundy S, Ma X, Rahn C and Trolier-mckinstry S 2018 Strongly (001) oriented bimorph PZT film on metal foils grown by rf-sputtering for wrist-worn piezoelectric energy harvesters *Adv. Funct. Mater.* **28** 1801327

[286] Kuo C L, Lin S C and Wu W J 2016 Fabrication and performance evaluation of a metal-based bimorph piezoelectric MEMS generator for vibration energy harvesting *Smart Mater. Struct.* **25** 1–10

[287] Tang G, Yang B, Hou C, Li G, Liu J, Chen X and Yang C 2016 A piezoelectric micro generator worked at low frequency and high acceleration based on PZT and phosphor bronze bonding *Sci. Rep.* **6** 2–11

[288] Dhakar L, Liu H, Tay F E and Lee C 2013 A new energy harvester design for high power output at low frequencies *Sens. Actuators* A **199** 344–52

[289] Xu C, Ren B, Di W, Liang Z, Jiao J, Li L, Li L, Zhao X, Luo H and Wang D 2012 Cantilever driving low frequency piezoelectric energy harvester using single crystal material $0.71Pb(Mg_{1/3}Nb_{2/3})O_3$-$0.29PbTiO_3$ *Appl. Phys. Lett.* **101** 033502

[290] Yang Z and Zu J 2016 Comparison of PZN-PT, PMN-PT single crystals and PZT ceramic for vibration energy harvesting *Energy Convers. Manage.* **122** 321–9